Storage of Short Light Pulses
in a Fiber–Based Atom–Cavity System

Dissertation
zur
Erlangung des Doktorgrades (Dr. rer. nat.)
der
Mathematisch-Naturwissenschaftlichen Fakultät
der
Rheinischen Friedrich-Wilhelms-Universität Bonn

vorgelegt von

Tobias Nicolay Macha
aus
Oberwesel, Deutschland

Bonn, 2018

Abstract

In this work I theoretically investigate and experimentally realize the storage of short light-pulses in a fiber-based atom-cavity system. Our miniaturized optical resonator – with seven times the natural atomic linewidth and a small mode volume – simultaneously ensures a high bandwidth and operation in the strong-coupling regime. In particular, it enables the storage of light pulses with on average one photon and a temporal extent of less than 10 ns, which is more than a factor of two shorter than the atomic excited state lifetime of rubidium. We obtain a storage efficiency of 8 %, consistent with both cavity losses and the employed level scheme.

In order to improve the coupling and number of measurements for which a single atom can be recycled, we use dipole-trap assisted, degenerate Raman sideband cooling and a further development of our carrier-free Raman sideband cooling scheme, which permits a three-dimensional ground state population of 70 %. The new techniques increase the measurement repetition rate by two orders of magnitude to ~ 2 kHz. Moreover, for the first time we achieve a Zeeman state preparation fidelity above 95 % in our experiment.

On this basis, I present the deterministic generation of single photons in the near-adiabatic limit. By shaping the control laser pulse, we do not only show that we can control the temporal waveform of retrieved photons, but also reach a faster extraction from the cavity-coupled atom than possible in free-space. The quantum nature of the retrieved light is verified by measuring a second-order correlation function, which yields the expected antibunching. Moreover, the generation of photons in the cavity mode with an efficiency exceeding 66 % is used as a fast hyperfine-state detection method, since our traditional, non-destructive state detection via a probe laser is no longer applicable in a Raman configuration due to the absence of a cycling transition. In order to realize Raman coupling between the two hyperfine ground states, we develop a scheme for shifting the cavity resonance frequency between two hyperfine transitions. During the scan, we are furthermore able to determine the atom-cavity coupling strength via the vacuum Rabi splitting in each individual measurement – a useful tool for post-selection of acquired data sets.

By employing a numerical simulation based on a full quantum-mechanical master equation, I find the strategy to store a coherent laser pulse with the maximum possible efficiency for a given system. Although the cavity input field is treated classically, our simulation model is able to calculate efficiencies for a pure single-photon Fock-state input. Moreover, numerical optimal control methods enable us to find control pulses with storage efficiencies slightly above those achieved for temporally-scaled adiabatic control pulses. For our specific system, we finally demonstrate the non-adiabatic storage of a short, coherent light pulse.

The ability to interact with pulses of high bandwidths encourages quantum hybrid experiments with quantum dots as single-photon sources. In this context, the stabilization of their emission frequency to an atomic transition is required. In collaboration with the IFW Dresden, I present a technique to counteract long-term frequency drifts by applying rate-based feedback to a strain-tunable quantum dot, which results in frequency deviations smaller than 1.5 % of its emission linewidth. By simultaneously stabilizing the emission frequency of two quantum dots in separate cryostats, we enhance their two-photon interference visibility in a Hong-Ou-Mandel measurement from 31 % to 41 %, which corresponds to the maximum reachable visibility for the given emitters. Frequency-stable, efficient photon sources together with atom-cavity based quantum memories may facilitate the realization of quantum networks.

Parts of this thesis have been published in the following article:

[1] **M. Zopf and T. Macha**, R. Keil, E. Uruñuela, Y. Chen, W. Alt, L. Ratschbacher, F. Ding, D. Meschede and O. G. Schmidt, *Frequency feedback for two-photon interference from separate quantum dots*, (2018), Physical Review B **98**, 161302(R)

Contents

Introduction

About 400 years ago, a series of German narratives addressed the absurd endeavors of citizens living in a ficticious medieval town called *Schilda* [2, 3]. The idea of confining light has seemingly inspired the imagination of the author(s): In one of the stories, the people, called *Schildbürger*, built a town hall without windows. The darkness inside led to accidents and confusion. Not realizing the construction error, they made efforts to collect light in buckets, cans, pots, potato bags and even mousetraps. But emptying the vessels inside the building did not illuminate the room – only removing the roof did.

Today, humanity has reached a point where the storage of light is no longer a ridiculous venture, but actually pursued in scientific projects. Strictly speaking, the light itself is not conserved, but its properties are copied by absorption and retrieved at a later point in time. This process of re-creating an indistinguishable and therefore identical state is commonly referred to as storage, also in many aspects of our everyday life.

Applications of light storage are found in the field of quantum information and communication [4–8], where the quantity of light is often reduced to the level of single photons. They are the optimum mobile carriers of quantum information [9], which lead to the term *flying* qubits. But unfortunately they are less suitable for processing [10] and storage of information [11]. Better candidates, especially for achieving (seconds-)long storage times, are neutral atoms [12], ions [13] or solid-state systems [14], which are *stationary* qubits. Their interconnection via communication links [15] is referred to as a *quantum network* [16, 17] and is the strongest motivation for the development of light-matter interfaces. The required strong light-matter coupling can be provided by optical cavities (resonators) [18]. They enable the tight confinement and temporary storage of an electric field, which enhances the interaction rate with a medium placed at its heart. In particular, neutral-atom based quantum nodes have proven themselves as versatile systems: Applications ranging from single-photon sources [19, 20], logic gates [21, 22], quantum memories [23, 24] in elementary CQED networks [25] to platform-comprehensive entanglement distribution [26] have been demonstrated.

Despite on-going efforts, a severe bottleneck of long-distance communication in a quantum network are the inevitable losses in optical fibers [27]. Direct signal amplification is excluded due to the *no-cloning theorem* [28], hence *quantum repeater nodes* [29, 30] are needed to create, purify and swap entanglement [31]. A potential realization out of many [32] is based on storing polarization-entangled photon pairs emitted by semiconductor quantum dots (QDs) in ensembles of ultra-cold atoms, which could be facilitated with an optical resonator. Two particular requirements therefore are that first, the QD emission frequency is compatible with an atomic transition and second, their spectral width matches the cavity linewidth. The first point can be addressed by frequency-tunable QD sources [33, 34] which are

referenced to an atomic standard. In order to fulfill the second criterion, the development of so-called *open* resonators with high bandwidths is being pushed forward [35, 36]. However, the high bandwidth means that the achievable light-matter interaction time is shortened. A compensation is possible by increasing the light-matter coupling, for which two approaches exist. First, reducing the cavity-mode cross section A amplifies the interaction rate g according to $g \propto 1/\sqrt{A}$. Second, one can exploit the collective enhancement provided by atomic ensembles of N atoms, since the collective coupling strength increases with $\sqrt{N}$. Following this motivation, we employ *Fiber-based Fabry-Pérot Cavities* (FFPCs) [37] consisting of microscopic, concave mirrors machined onto the end facets of two opposed optical fibers to reduce the mode volume while still maintaining optical access to manipulate atomic ensembles within the cavity region [38, 39]. While high-density clouds of atoms have already been coupled to FFPCs [40, 41], our focus lies on the controlled manipulation of individual atoms at low numbers, which allows local addressing [42] or the implementation of quantum registers [43].

In this work I present the fast storage of light pulses in a single rubidium atom coupled to a fiber-based microcavity. By developing new techniques to control the internal and external states of the atom, light pulses shorter than the rubidium excited state lifetime are mapped into the single-photon memory. A subsequent adiabatic read-out generates single photons with arbitrarily malleable waveforms. In order to understand the underlying dynamics and to determine the optimum storage efficiency, I simulate our system with a Lindblad master equation approach. On this basis, a specially developed, optimal-control based pulse optimization algorithm ensures that we apply the most effective control pulses.

The ability to work with high-bandwidth photons paves the way towards *hybrid experiments* [44] with quantum dots as single-photon sources. The idea is to combine the advantages of individual systems, such as the long coherence time in atomic memories [24] and the high emission rate of QDs [45]. In order to join the diverse platforms, I will show how the tunable QD emission frequency can be stabilized to rubidium transitions. The scheme is furthermore applied to two distant emitters simultaneously, which opens possibilities for quantum networking with maximally-indistinguishable photons.

A Fiber–Cavity System as a Light–Matter Interface

Cᴀᴠɪᴛʏ Quantum Electrodynamics (CQED) platforms have proven to be excellent for light-matter interfacing [46], which makes them a strong candidate for quantum networks. Apart from elementary demonstrations [25], the major challenge of realizing an efficient, scalable network with a high bandwidth remains. The latter is a strict requirement for today's most promising single photon sources [47–49] and is addressed by open cavities. In order to maintain a rate of coherent interaction above their leakage and loss rates, the overlap of light and matter cross sections needs to be maximized. A fiber-based resonator greatly reduces the cavity mode waist, while still offering optical access for the numerous light fields required to trap and manipulate atomic ensembles – a strong candidate for the collectively enhanced storage of quantum information [40, 41, 50].

Following this motivation, our group developed such a system in the past years. As the work presented here would not have been possible without this solid, experimental basis, there is a lot to learn about our setup that is beyond the scope of this thesis. I strongly recommend to read the work of J. Gallego [51] for insight into CQED basics, the production of fiber cavities and atom trapping, state detection, transport and coupling to a resonator.

The major modifications to the original apparatus are described in this introductory chapter. Section 2.1 gives a brief overview of the experimental apparatus, followed by a more detailed list of improvements on the stabilization of the cavity resonance and related light fields (Sec. 2.2 and 2.3). Two entirely new optical setups to address transitions at the D_1 line of rubidium and to create short coherent photon pulses are presented in Sections 2.4 and 2.5, respectively. In the discussion of modifications we omit the optical setups for both Raman lasers (cooling and storage), as they are very similar to previous realizations, e.g. [52].

2.1 An Overview of the Experimental Apparatus

In our experiments, we use a 3D magneto-optical trap [53] to collect a few tens of neutral ^{87}Rb atoms from the background gas (10^{-10} mbar), which simultaneously cools them down to $\sim 50\,\mu$K. Subsequently they are loaded into an optical lattice which acts as an optical conveyor belt [54–56] for transporting atoms into the ~ 1 mm distant cavity region, as depicted in Figure 2.1. A near-resonant *probe laser* at 780 nm non-destructively detects the presence of an atom and stops the transport in real-time, which we refer to as *feedback transport* [51, Sec. 3.2]. By sparsely loading the trap we limit the probability of a detection event to 70 %, such that we are sure to work with a single atom at the cavity, in most cases.
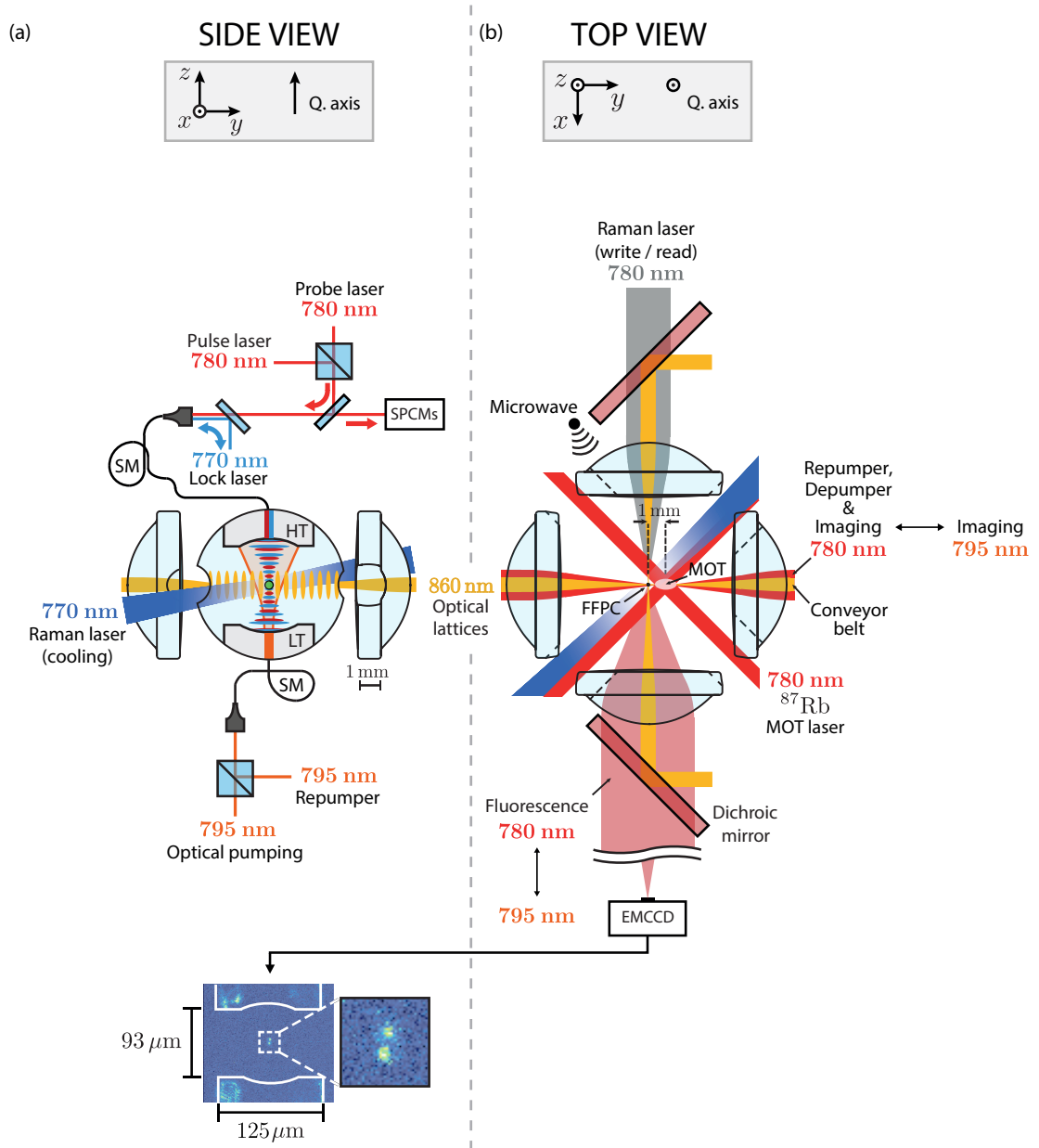
Figure 2.1: Side **(a)** and top view **(b)** of the fiber-based atom-cavity system (not to scale). Atoms are trapped in a magneto-optical trap (MOT) outside the cavity region (FFPC). After loading them into a 1D optical lattice, they are transported into the cavity mode, where a single one is confined in three dimensions. The cavity region is displayed both schematically and in an atom fluorescence image taken by an EMCCD camera. The fiber dimensions are identified by scattered light. Along the cavity axis, cavity-resonant fields address the atoms via the high-transmission mirror (HT), while the low-transmission mirror (LT) is reserved for off-resonant beams – accepting power losses. In both cases, the light is intrinsically guided and coupled to the resonator by single-mode fibers (SM). Single-photon counting modules (SPCMs) detect the weak, reflected probe light used for atom(-state) detection. A detailed description of all involved lasers for optical pumping, cooling and photon generation/storage is found in the main text. The figure is adapted from [39] and illustrates the progress in complexity: A total of 27 beams from 9 lasers are pointed at the atoms.

Table 2.1: Relevant parameters of our cavity system, as obtained from characterization measurements in [51]. The error bars correspond to either direct or propagated experimental uncertainties. The maximum atom-light coupling rate g_{max} is calculated for the ideal case of a single atom at the center of the cavity mode. The finesse values and the cavity linewidth were measured when the cavity was still outside the vacuum [38].

Parameter		Value	Extracted from
Mirrors (HT/LT)			
Transmission	$\mathcal{T}$	$(126 \pm 13)/(13 \pm 3)\,\mathrm{ppm}$	direct measurement
Losses (scat. and abs.)	$\mathcal{L}$	$(26 \pm 5)/(25 \pm 5)\,\mathrm{ppm}$	finesse and transmission
Cavity geometry			
Length	L_{cav}	$(93.36 \pm 0.03)\,\mathrm{\mu m}$	lock-probe beat length
Mode waist	w_0	$(4.40 \pm 0.04)\,\mathrm{\mu m}$	cavity geometry
Input mode matching	ϵ_{HT}	$0.60 + -0.02$	reflection dip asymmetry
Cavity spectroscopy			
Free spectral range	$\Delta\nu_{\mathrm{FSR}}$	$(1\,606.7 \pm 0.5)\,\mathrm{GHz}$	cavity length
Cavity full width	$\Delta\nu_{\mathrm{FWHM}}$	$(50.8 \pm 1.0)\,\mathrm{MHz}$	sideband-modulated dip
Finesse (780 nm)	$\mathcal{F}$	$32\,800 \pm 1\,100$	FSR-FWHM ratio
Finesse (770 nm)	$\mathcal{F}_{\mathrm{lock}}$	$27\,200 \pm 1\,000$	FSR-FWHM ratio
Pol.-mode splitting	$\Delta\nu_{\mathrm{spl}}$	$(9.0 \pm 0.3)\,\mathrm{MHz}$	Hänsch-Couillaud setup [57]
Lock-probe beat length	d_{beat}	$(31.12 \pm 0.01)\,\mathrm{\mu m}$	
CQED parameters			
Atom-light coupling	$g_{\mathrm{max}}/2\pi$	$(121.6 \pm 1.1)\,\mathrm{MHz}$	$^{87}\mathrm{Rb}$ D_2-line cycling transition
Cavity field decay	$\kappa_{\mathrm{total}}/2\pi$	$(24.5 \pm 0.8)\,\mathrm{MHz}$	measured cavity linewidth
Atomic dipole decay	$\gamma/2\pi$	$3.03\,\mathrm{MHz}$	rubidium natural decay [58]
Single-atom cooperativity	C	100 ± 4	

Furthermore, this method constitutes a preselection of the atom-cavity coupling strength g, since only atoms positioned at the center of the cavity mode will trigger a detection event.

The atom is now located at the heart of the apparatus: A fiber Fabry-Pérot cavity (FFPC) [37], described in detail in [38]. One of the mirrors presents a higher transmission (HT), ensuring a highly directional input-output channel. Weakly probing the cavity results in reflection signals from the mirror which are detected by single-photon counting modules (SPCMs). Against expectations, the low-transmission mirror (LT) is also put to use as an access port for optical pumping light at 795 nm[1]. As the quantization axis is defined by a magnetic guiding field along the cavity axis, only in this direction pure σ-polarized pumping is attained. For π-polarized pumping, we use linearly-polarized beams co-propagating with the lattice beams.

The cavity is placed in the center of four aspheric lenses (NA = 0.5), which leads to a high degree of optical control in our system [60–62] compared to previous approaches [63]. They strongly focus two pairs of counter-propagating, red-detuned dipole trap beams at 860 nm which create a 2D optical lattice (DT$_{\mathrm{x,y}}$) [64]. The perpendicular confinement is given by the intra-cavity, blue-detuned *lock laser* field [65–67] at 770 nm (DT$_{\mathrm{z}}$), which is used to stabilize the resonator length (Sec. 2.2). As a result, the

---

[1] Far off-resonant w.r.t. the cavity resonance frequency, as opposed to experiments with three resonant wavelengths [59].

single atom is located with sub-wavelength precision at the antinode of the cavity mode, that is set to overlap with the node of selected hyperfine transitions of the D_2 line of ^{87}Rb at 780 nm (Sec. 2.3).

The lenses are whetted (dashed lines in Fig. 2.1(b)) to give access to both MOT beams and a new Raman laser beam at 770 nm which is not only used for (motional-) state spectroscopy but also cools the atoms down to the 3D motional ground state in our carrier-free Raman cooling scheme [63, 68, 69] (see Sec. 3.2). Spectroscopy of the Zeeman structure can be performed using resonant microwave radiation [52].

Imaging the atoms is done with 780 nm or 795 nm light [70], where the latter can be useful to prevent coherent cavity interaction [39], also in the case of optical pumping (see Sec. 2.4). An alternative to avoid the influence of the cavity is to shift its resonance frequency by several hundred MHz (see Sec. 2.2).

After passing through the pulse shaping setup described in Section 2.5, the pulse laser enters the cavity resonantly as a weak coherent laser pulse, which is mapped into the atomic hyperfine ground states by a dedicated, pulsed Raman laser propagating perpendicularly along DT_x.

Finally, in Table 2.1 the most relevant cavity parameters are listed. They are based on characterization measurements in [51].

2.2 An Improved Scheme for Stabilization of the Cavity Resonance

The cavity length is stabilized to the lock laser using the well-known Pound-Drever-Hall (PDH) method [71]. In the previous setup configuration [51], the lock laser itself was stabilized to a transfer cavity [72], which in turn was referenced to the probe laser, that is locked to a Doppler-free polarization spectroscopy [73]. This complicated *cavity lock chain* has two outstanding disadvantages: First, the cavity resonance can only be shifted, if we shift the lock laser frequency by acousto-optic modulators (AOMs). But the finite AOM bandwidth leads to a drop in diffraction efficiency; and the loss of laser power influences the signal-to-noise ratio of the PDH error signal. This problem was technically circumvented by introducing a second lock laser between the first one and the transfer cavity. A frequency-offset lock [74] between the two lock lasers allowed to scan the cavity length for more than ±250 MHz, enough for a detailed analysis of the *vacuum Rabi splitting* (VRS) and the Purcell effect presented in [39]. Still, the frequency scan range was restricted by the laser power. Second, and more importantly, such a lock chain is too long. While effects such as frequency noise propagation do not affect daily work in an obvious way, the product of five single lock failure probabilities does[2].

We improve the cavity lock chain by stabilizing the lock laser[3] to an optical frequency comb[4] [77], which is specified to have a stability of better than $2 \cdot 10^{-16}$ in 1 s and $3 \cdot 10^{-18}$ in 1000 s, with an integrated phase noise of < 100 mrad in the range 100 Hz to 2 MHz [78]. Subsequently, the resonator and the Raman laser for cooling are locked in parallel to the lock laser, reducing the chain length significantly, as depicted in Figure 2.2. Referencing to a frequency comb has an exciting feature: The cavity length can be shifted considerably by scanning the lock laser across multiple comb lines [79–81] that are spaced by 250 MHz. While the phase lock to a single comb line is realized with our custom optical phase-locked loop (OPLL) technique [52, 82], the continuous tuning requires switching between two comb lines. Hence, we have developed a technique which is presented in detail in [83, 84]. By simultaneously changing the local oscillator frequency of the OPLL (f_{OPLL}) and the driving frequency of the in-loop

---

[2] To give an example, the 1.5 m long transfer cavity is prone to temperature drifts and – presumably – air pressure changes / acoustic noise upon opening and closing the lab door.

[3] All 780 and 770 nm lasers in this experiment are interference-filter stabilized external cavity diode laser (IFL), developed in our group based on [75]. Details see [76].

[4] *MenloSystems FC1500-250-ULN*, but with a downgrade of the SYNCRO-RRE module, which suffers from pending 1 Hz noise.
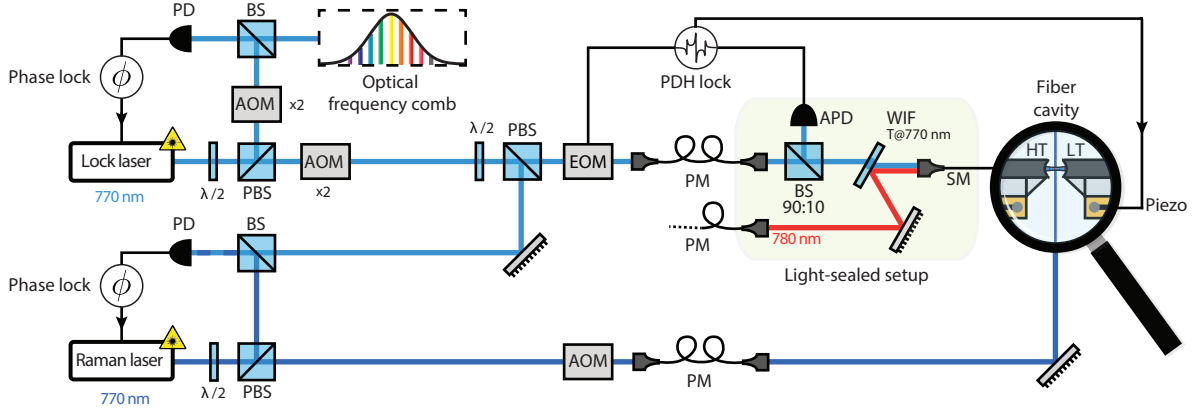
Figure 2.2: An improved *cavity lock chain* for cavity QED experiments. The fiber cavity is stabilized via the Pound-Drever-Hall (PDH) method to the lock laser, which is in turn referenced to an optical frequency comb via an optical phase-locked loop (OPLL, ϕ). The OPLL error signal for frequency feedback is based on an optical beat signal, which is created at a beam splitter (BS) and detected by a photodiode (PD). The Raman laser for spectroscopy and cooling is also phase-locked to the lock light and follows any frequency change caused by the in- and out-of-loop AOM double passes (AOM x2) of the lock laser. An AOM for pulsing the Raman laser before entering a polarization-maintaining (PM) optical fiber is shown at the bottom. The PDH error signal is created with the help of both an electro-optic modulator (EOM) for creating a frequency modulation and an avalanche photodiode (APD) for detection of the lock laser reflection. The correction signal is applied to a piezo-electric actuator (Piezo), to which the cavity is attached. Inside the light-sealed setup for single-photon detection with low background noise (shaded area), probe and lock laser are overlapped with the help of a wide interference filter (WIF) and coupled into the single-mode (SM) fiber spliced to the fiber cavity. In general, adjustments of the laser power are made with a combination of half-wave plate ($\lambda/2$) and polarizing beam splitter (PBS). For details on the lock mechanisms, polarization control, photon detection and frequency filtering see [51, 52, 60]. Compare to the previous lock configuration in [51, Fig. 2.21] and the split-off *probe lock chain* for 780 nm in Figure 2.3.

AOM double pass (f_AOM), we 'jump' over a comb line without causing an abrupt change of the laser frequency at the cavity, as long as we ensure:

$$\left(f_\text{OPLL, after jump} - f_\text{OPLL, before jump}\right) + 2 \cdot \left(f_\text{AOM, after jump} - f_\text{AOM, before jump}\right) = 250 \text{ MHz}$$

The RF frequencies are provided by Direct Digital Synthesizers[5] which feature continuous frequency changes. Consequently, the duration of a jump is merely limited by the AOM rise time on the ns scale, which is too fast for piezo-electric actuators to react. Thus the cavity can follow frequency shifts for up to 1 GHz [84], only limited by the mode-hop free range of the reference laser[6]. An additional out-of-loop AOM is mainly used for intensity stabilization, but can also be included for frequency scanning.

We characterize the properties of the phase lock and find 99 % of the laser power in the carrier frequency, concluded from an optical beat signal between lock laser and comb light [83]. While this is a good value, the limited feedback loop bandwidth gives rise to *servo bumps* at 1.1 MHz (present in Fig. 3.4(b)) [84]. By shortening the electronic path of the loop, values up to 1.6 MHz (absent in Fig. 3.5(b)) are achieved. As the lock laser is part of the Raman spectroscopy setup, frequency

---

[5] *Analog Devices EVAL-AD9915* evaluation boards

[6] External cavity lasers with additional polarization spectroscopy feedback exhibit large tuning ranges, e.g. 105 GHz at a rate of 11 Hz [85].
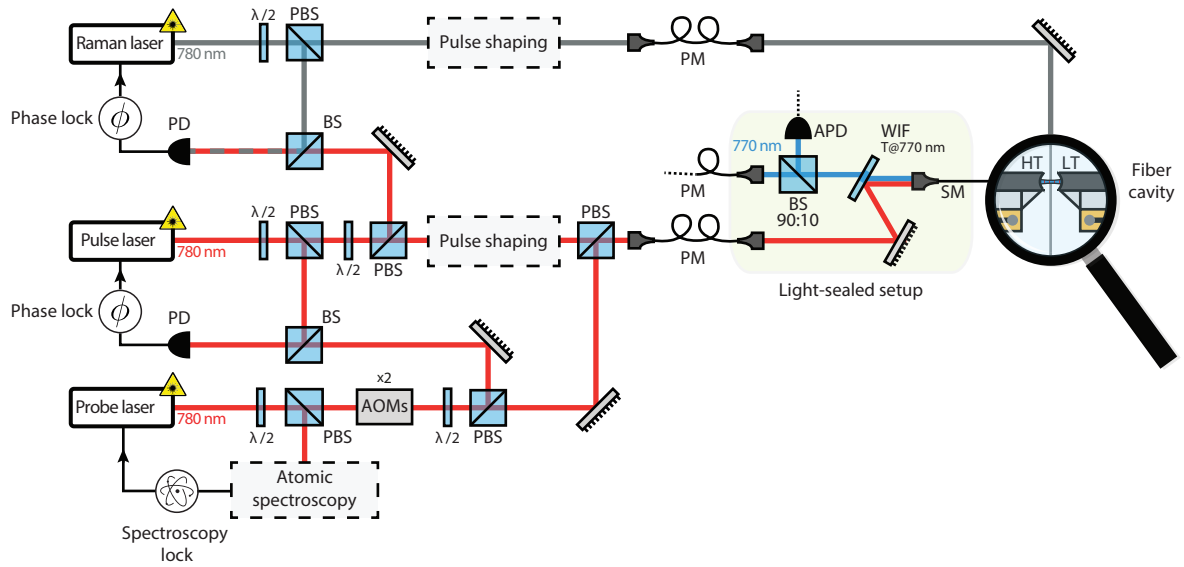
Figure 2.3: The new *probe lock chain* for photon storage experiments. The probe laser for atom detection is referenced to an atomic spectroscopy setup. The pulse laser is phase-locked to the probe laser frequency, which can be shifted by several AOM double passes (AOMs x2). Not only the pulse laser, but also the attributed Raman laser follows the probe laser due to a second phase-lock stage. The photon pulse to be stored and its corresponding Raman pulse are created in pulse-shaping setups as explained in Section 2.5. When pulse and probe laser are combined at the PBS, they have a fixed phase relation. Inside the light-sealed setup (shaded area), probe, pulse and lock laser are overlapped and coupled into the SM fiber spliced to the fiber cavity. For details on the lock mechanisms, polarization control, photon detection and frequency filtering see [51, 52, 60]. Compare to the previous lock configuration in [51, Fig. 2.21] and the split-off *cavity lock chain* for 770 nm in Figure 2.2.

components modulated onto its carrier frequency play an important role (see Sec. 3.2.1). They can propagate to the Raman laser itself, which follows the lock laser at a fixed detuning corresponding to the rubidium hyperfine splitting of ~ 6.8 GHz.

2.3 From Cycling Transition to Lambda Configuration

In the experiments presented in this thesis, we have to work with a cavity resonant to two different hyperfine transitions $|F, m_F\rangle \to |F', m'_F\rangle$ of the D$_2$ line ($5^2S_{1/2} \to 5^2P_{3/2}$). First, we have to detect the atoms during the feedback transport, for which a high atom-cavity coupling g is required. As g is proportional to the hyperfine dipole matrix elements, we find that the *cycling transitions* $|2, \pm2\rangle \to |3', \pm3'\rangle$ give the strongest couplings. In combination with the quantization axis defined by the bias magnetic field, our probe laser is chosen to drive σ^--transitions[7]. Consequently, with the help of a repumping laser, a few scattering events pump the atom to $|2, -2\rangle$, which provides a two-level system suitable for clean state detections based on the VRS, see [51, Ch. 5]. The VRS in dependence of the coupling strength is illustrated in Figure 2.4. Directly detecting the atoms on the $|2\rangle \to |2'\rangle$ transition is not possible: Even if probe lasers with opposite circularity are used simultaneously to avoid dark states, the low coupling strength leads to reduced reflection contrast, as the intermediate regime is approached. Consequently, spatial positioning of the atoms is imprecise, which additionally makes it more difficult to estimate the

---

[7] The low birefringent splitting of the cavity supports circularly polarized light and therefore $\sigma^\pm$-transitions, see [38].
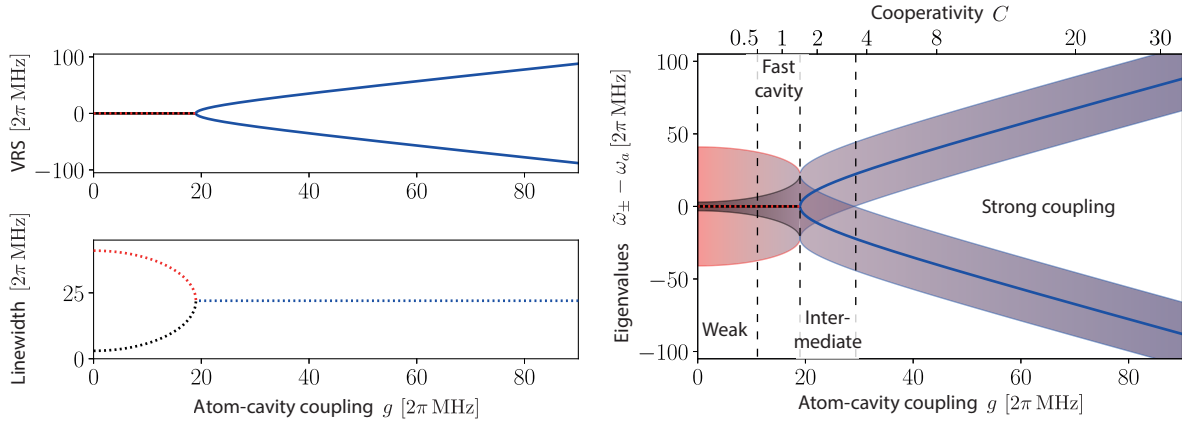
Figure 2.4: Frequency spectrum of the open, non-driven atom-cavity system as discussed in [51, Sec. 4.1.1, cf. Fig. 4.2]. Here, its parameters are $(\kappa, \gamma) = 2\pi \cdot (41, 3)\,\text{MHz}$. Left: The real and imaginary part of the complex eigenvalues $\tilde{\omega}_{\pm}$ of the non-Hermitian Hamiltonian $\hat{H}_{\text{diss}} = \hat{H}_{\text{JC}} - i\hbar\,(\gamma\,\hat{\sigma}^{\dagger}\hat{\sigma} + \kappa\,\hat{a}^{\dagger}\hat{a})$ describe the *vacuum Rabi splitting* (VRS) and the atom- (black) and cavity linewidth (red) at full-width half-maximum, respectively (see also Ch. 4 for the nomenclature). Right: $\tilde{\omega}_{\pm} - \omega_{\text{a}}$ as a function of the atom-cavity coupling strength g. Thus by changing the probe laser frequency, we are able to measure the VRS, from which the parameter g is extracted. At the *cycling transition* with $g \approx 2\pi \cdot 80\,\text{MHz}$, we are located deep within the strong-coupling regime. In a Λ-*configuration* we approach the intermediate regime with $g < 2\pi \cdot 35\,\text{MHz}$. The reduced coupling strength, despite our cooling techniques (see Ch. 3), is a consequence of the weaker atomic transition. For all measurements in this work, the fast- and weak-cavity domain are irrelevant.

number of atoms by the loading efficiency η_{load}.

As we will see in Chapter 6, photon storage and generation require a Λ-type three-level atom, from now on referred to as Λ-*configuration*. In order to realize this level scheme, the cavity resonance has to be shifted by 267 MHz [58] – as well as the probe, pulse and two Raman laser frequencies[8]. While the scanning of the cavity resonance has been discussed in the previous section, the setup for simultaneous scanning of the other lasers is shown in Figure 2.3. The probe frequency is still stabilized to an atomic spectroscopy setup, but it also serves as a reference for the pulse laser. This phase lock is then extended by a second-stage phase lock, in which the attributed Raman laser is locked to the photon laser. Frequency-shifting all beams is realized by multiple AOM double passes. Here, the loss in probe power is not a problem, since for atom- and state detection we only need on average $6 \cdot 10^{-5}$ photons in the cavity.

In summary, during measurements the resonance setting has to be shifted between two set points, which we refer to as *sweep*. If we first shift the probe- and then the cavity lock chain, we are able to observe half of the VRS. From the frequency-dependent probe reflection we can draw conclusions on the coupling strength of an atom in each individual loading attempt, which is a useful tool for post-selection of acquired data sets and referred to as *VRS sweep*.

2.4 A Reliable Laser Source for Additional Atomic Transitions

Quantum optics experiments heavily rely on the sub-MHz linewidth and long-term stability of lasers. A significant improvement in this regard was the upgrade from Littrow lasers to interference-filter stabilized

---

[8] For this to work, lock- and probe laser are frequency-tuned with AOMs and 4 locks follow - back and forth every 5 s!

external cavity diode lasers (IFLs) [63]. However, these lasers are still vulnerable to mode hops caused by daily thermal drifts. Distributed feedback (DFB) lasers on the contrary offer a single-frequency operation over several nanometers, at the cost of a limited tuning range around their center wavelength [86] and an increased linewidth. The difference to standard diodes is the periodic structure of the active region itself, which forms an interference grating that gives optical feedback. This renders an external cavity optional.

We use two 795 nm DFB lasers[9] mounted in special housings[10]. They are implemented in the existing setup [70], which is extended such that each laser can be pulsed and frequency-shifted independently with the help of AOM setups. The suppression exceeds 10^{12}, dispensing with the need of mechanical shutters and thus allowing pulse times on the μs timescale. With a linewidth of typically 0.6 MHz the diodes are applicable for frequency-uncritical tasks such as MOT operation or optical pumping[11]. The previously unused D line ($5^2 S_{1/2} \rightarrow 5^2 P_{1/2}$) at 795 nm is now the main transition for the latter. Whenever we apply D_1 light, a single-photon detuning of about $2\pi \cdot 15$ MHz with respect to the excited state is chosen, for which the a.c. Stark shifts of the dipole trap have to be taken into account. We have extended the calculation in [60] based on [87, 88] and find a shift of +21.6 MHz/mK for each m_F-sublevel of $F' = 2$.[12] Considering also the equally shifted ground states, the free space transition frequency has to be adjusted by +42 MHz/mK.

As mentioned in Section 2.3, $|2, -2\rangle$ is our target state and, on the practical side, a *dark state* with respect to simultaneous, σ^--polarized pumping resonant with $|2\rangle \rightarrow |2'\rangle$ and $|1\rangle \rightarrow |2'\rangle$. The strict requirement for pure σ^--transitions is a $\vec{k}$-vector along the quantization axis, that is parallel to the cavity axis. The D_1 laser frequency cannot be resonant with both the cavity and the atoms along with the probe laser: Since the free spectral range of the resonator is 1.6 THz, the closest, cavity-resonant detuning with respect to the atom is 695 GHz. Our only chance to manipulate the atoms is a brute force approach by entering the cavity through the LT mirror opposite to the lock- and probe laser entrance port. This requires a laser power of ~ 1 mW before the fiber, since the LT mirror coefficient of transmission is (13 ± 3) ppm (see Table 2.1). Considering the SM fiber NA of 0.13, we estimate the beam waist to be above 6 μm at the position of the atoms. Nevertheless, for F-pumping a pulse length of a few μs is required. From previous free-space measurements we conclude that losses at splicings and fiber in-coupling must be significant. The deficit is not entirely unexpected, since UV light at 405 nm is coupled into the same fiber; using the same collimation lens. The reason is an ever-present finesse decay reported in [51, Appendix A.2], which is equivalent to a modified cavity loss rate which is introduced in Section 4.1.

2.5 A Setup for Short Light Pulses

A main building block for the experiments in this thesis has been the development of a pulse-shaping setup. In order to create arbitrary, optical waveforms, the intensity of both pulse and attributed Raman laser is modulated with a waveguide-based Mach-Zehnder electro-optical intensity modulator. The operating principle is the following: The incident beam is split into two paths which form the arms of a Mach-Zehnder interferometer. Each of these arms is a waveguide made from an electro-optic material, which induces a phase change when a voltage is applied. Thus, intensity modulation occurs due to time-varying interference of the two phase-shifted beams.

If, however, the RF electrode for changing the voltage is not placed symmetrically between the waveguide channels, an opposite but unequal phase is induced. As a result, the output has a residual

---

[9] *Eagleyard* model *EYP-DFB-0795-00080-1500-BFW01-0005*

[10] *Thorlabs LM14S2* mount with LD/TEC driver connection

[11] Indeed we have stabilized an 894 nm DFB laser to another one in an OPLL, giving two-fold feedback to the LD current and resulting in 92 % of the power in the carrier of the beat spectrum. The single linewidths were estimated to be around 350 kHz.

[12] For $F' = 3$ a quadratic shift is observed, see Figure 5.1(b) and [60].
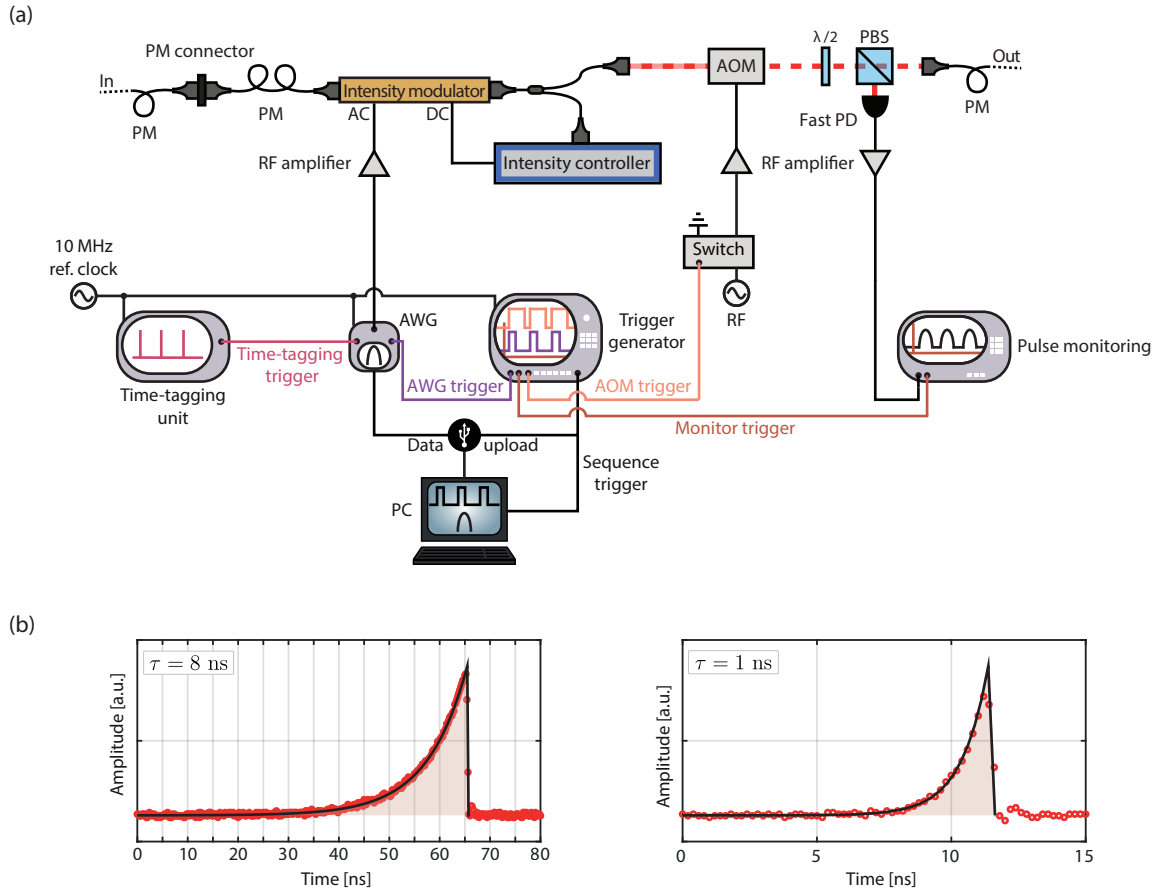
Figure 2.5: **(a)** A simplified setup for shaping short, coherent light pulses. A PC is used to generate RF pulse shapes and trigger sequences, which are then released by a combination of a trigger generator and an arbitrary waveform generator (AWG). These RF electronics drive an intensity modulator, whose output is intensity-stabilized. There is an imperfect suppression of the light-pulse background, which we improve with a single-pass AOM for optical switching. The triggers and pulses are recorded by a time-tagging unit and a pulse monitor. Each device shows a stored or recorded pulse shape or pattern in a white area, to understand the pulse creation in an intuitive way. For a full description, see main text. **(b)** To illustrate the AWG capabilities, we create, record (red points) and fit (black line) exponentially rising pulse shapes of $\tau = 8$ and 1 ns. Such a shape is e.g. useful for loading a photon into an empty cavity [91]. How well the optical shape agrees with the expected value can be seen in Figure 5.3(a).

phase modulation, which is synonymous with a frequency chirp. The size of this potentially detrimental effect is quantified by the intrinsic chirp parameter α_0 [89]. Our device is specified to exhibit $\alpha_0 = 0 \pm 0.1$; and by modulating the EOM we verified $\alpha \approx 0$ based on the methods in [89, 90].

The frequency chirp, if present, can also be used for the better: In atom optics experiments, chirped pulses have e.g. been used for adiabatic (de-)excitation [92]. In our experiments, phase adjustments of the Raman pulse could contribute to the storage efficiency of photon pulses, as discussed in Section 6.1.1.

The pulse-shaping setup is depicted in Figure 2.5(a) in a simplified way[13]. A *Python*-based script running on a PC is used to calculate the individual pulse shapes and a sequence, in which they are

---

[13] In reality, the upper part exists twice; once for the pulse, once for the Raman laser.

triggered. The data is uploaded via USB to an arbitrary waveform generator (AWG)[14] and a trigger generator[15]. The AWG features a rise time of 120 ps, allowing sharp features as demonstrated in Figure 2.5(b). Two different pulse shapes can be stored in a register and triggered alternatingly.

Upon a sequence trigger given by the PC, the trigger generator releases a pulse pattern, which is time-tagged with 81 ps resolution by the unit[16] that also records the SPCM count traces. This way, generated photon pulse shapes can be reconstructed. Each AWG trigger results in an RF pulse, that is sent to the intensity-modulating EOM[17]. This AC component is added to a DC component, which is regulated by an intensity controller[18] such that a low EOM output is maintained outside the pulse windows. The suppression of the transmission is limited to a factor of ~ 150 in power, which is only a factor of ~ 12 in Rabi frequency. Therefore, single-pass AOMs are used to improve the background level, but the window size in our implementation is restricted to > 60 ns [93]. For shorter windows, the AOM pulse does not exhibit a flat plateau onto which the EOM pulse is ideally placed, and also the AOM efficiency is reduced. This is not a problem for the very weak coherent pulse to be stored, but for the storage-assisting Raman pulse that needs up to $200\,\mu$W of optical power it is. The RF shift caused by the AOMs is compensated by the OPLLs in the probe lock chain. RF amplifiers allow to set the power for two successive pulses independently, i.e. the laser power for photon storage can be scanned while the power for photon generation is fixed. All devices and RF sources are locked to an atomic reference clock (10 MHz).

The EOMs require an optical input power of 10 mW, which is why the probe/MOT laser cannot be used as a source. Instead, we have converted the Raman laser setup in [52] to pulse and Raman laser (Fig 2.3). Both laser frequencies thus have a fixed phase relation upon arriving at the atom position.

A fraction of the pulses is monitored by a fast photodiode[19] and a high-bandwidth oscilloscope[20]. As expected, the transmitted intensity after the EOM does not depend linearly on the RF amplitude V, but it approximately follows a $\sin^2(V)$-relation, which is pre-compensated in all measurements. Finally, the pulse is sent through PM fibers to the experiment.

---

[14] *WavePond DAx14000*, up to 16 M data-point entries per segment, read by internal clock of 4 GHz

[15] *Rigol DG4102*, supporting SCPI commands and arbitrary pulse shapes (such as a trigger sequence) up to 80 MHz.

[16] *ID Quantique ID800* 8-channel time-to-digital converter

[17] *iXblue NIR-MX800-LN-10-P-P-FA-FA* with a bandwidth > 12 GHz

[18] *Photline MBC-DG-BT-PD*

[19] *Thorlabs DET025AFC* with a bandwidth of 2 GHz

[20] *TEKTRONIX 4104* with a bandwidth of 1 GHz and a sampling rate of 5 Megasamples/second

Controlling Internal and External States of a Single Atom in an Optical Cavity

Tʜᴇ investigation and application of quantum physics demands an extraordinary level of control. Without the development of cooling techniques to counteract motional state changing mechanisms, demanding experiments such as high precision metrology [94], quantum logical gates [95], the observation of optomechanical effects [96] or the coupling of quantized states of atomic motion to quantum states of light [97] would not have been possible. Not to mention that if an experiment is based on scattering photons or suffers from parametric heating induced by dipole traps [98, 99], atom losses will greatly reduce the duty cycle.

A prominent approach to reduce the temperature of neutral atoms is evaporative cooling [100]. But since the mechanism is associated to atom loss, it is only applicable to large atomic ensembles. In the previous cavity experiment, our group used cavity cooling [101–103] as a standard technique instead. As a proof of principle, we furthermore demonstrated ground-state cooling of a single atom by both electromagnetically induced transparency (EIT) [104–106] and carrier-free Raman sideband cooling [63].

Unfortunately, the robust cavity cooling technique does not work in the regime of open resonators, since the steady-state temperature limit is given by $T_{\text{cav}} = \hbar\kappa/k_{\text{B}}$ [51]. As a consequence, a trapping force that holds atoms at the temperature $T_{\text{cav}} \approx 2$ mK is required, which we cannot provide. But at weak cavity probing, we have recently observed a lifetime-enhancing effect. In Section 3.1, we show phenomenologically that it is based on degenerate Raman sideband cooling [107–110] evoked by the dipole traps. With strong guiding fields as required for addressing selected Raman transitions, the technique is no longer applicable. Additionally, the state-changing effect is ever-present and interferes with optical pumping [111]. We solve this issue by adapting and extending the carrier-free Raman cooling scheme to three dimensions (Sec. 3.2.2). Finally, we characterize the state preparation required for photon generation and storage (Sec. 3.3), demonstrating a high degree of control over the internal and external states of a single atom coupled to the resonator.

3.1 Degenerate Raman Sideband Cooling of a Single Atom

In quantum gas experiments, laser cooling is limited by hyperfine-changing collisions [112]. These density-dependent heating mechanisms were overcome by traps in the Lamb-Dicke regime [113] and the development of degenerate Raman sideband cooling [107]. This technique relies on Raman transitions [114] between the vibrational manifolds associated with a pair of magnetic sublevels of a fixed hyperfine ground state. Remarkably, this coupling is intrinsic to the lattice potential itself and therefore

Figure 3.1: **(a)** Optical fields involved in degenerate Raman sideband transitions (cf. Fig. 2.1). In reality, the 860 nm dipole traps have a small angle with respect to the cavity axis. The magnetic guiding field $\vec{B}$ itself has a controlled tilt α. Optical pumping is applied along the dipole trap (780 nm) or the cavity axis (780 / 795 nm). **(b)** The schematic drawing shows two different ways of reducing the quantized motional state $|m\rangle$ in an approximated harmonic trap potential with trap frequency ν. The blue-detuned lock laser trap (770 nm) drives $\sigma^{\pm}$-polarized two-photon transitions, whereas the red-detuned dipole traps drive a combination of $\sigma^{\pm}$ and π. For the 860 nm beams, the addressed potentials are not exclusively along the propagation direction, since their wave vector projects along the cavity axis as well. Repumpers (not shown) transfer the population back towards $|F, m_F\rangle = |2, -2\rangle$, such that Raman cooling will be constantly present if Equation 3.1 is fulfilled. In $F = 1$, atoms are lost due to Raman heating and the absence of cooling.

supersedes a separate set of phase-locked lasers – a convincing argument if one is interested in simplifying experimental setups.

To observe a cooling effect, the dipole trap beams need to be able to address $\sigma^{\pm}$ and π-transitions simultaneously, while the Zeeman splitting $\Delta\omega_B$ in the presence of a magnetic guiding field strength B has to match a multiple m of the trap frequency ν [115]:

$$\Delta\omega_B = m \cdot 2\pi \cdot \nu. \tag{3.1}$$

In [107–109], the lattice consists of three coplanar laser beams, of which two are linearly polarized in the lattice plane perpendicular to the quantization axis. The third one is elliptically polarized to enable Raman coupling. Our situation is displayed in Figure 3.1(a). We notice the cooling effect, when the quantization axis is not collinear with the cavity axis ($\alpha \neq 0$). At the same time, the alignment of DT$_y$ is in reality not perpendicular to DT$_z$, as introduced in Figure 2.1, but it has a small angle of $\sim 8°$. For DT$_x$, which is orthogonal to the imaging plane, we estimate that the angle is below $20°$. As a result, the DTs (with linear polarization) are no longer purely π-polarized as in [60] and m_F-state changing two-photon transitions can occur.

Two examples of degenerate Raman cooling transitions, which change the approximated harmonic oscillator state with a vibrational excitation m, are indicated in Figure 3.1(b). The red-detuned, 860 nm traps have two equivalent possibilities to change m by $\Delta m = -1$. For circularly polarized traps – as our blue-detuned, 770 nm intra-cavity dipole trap – motional state changes of $\Delta m = \pm 2$ have been
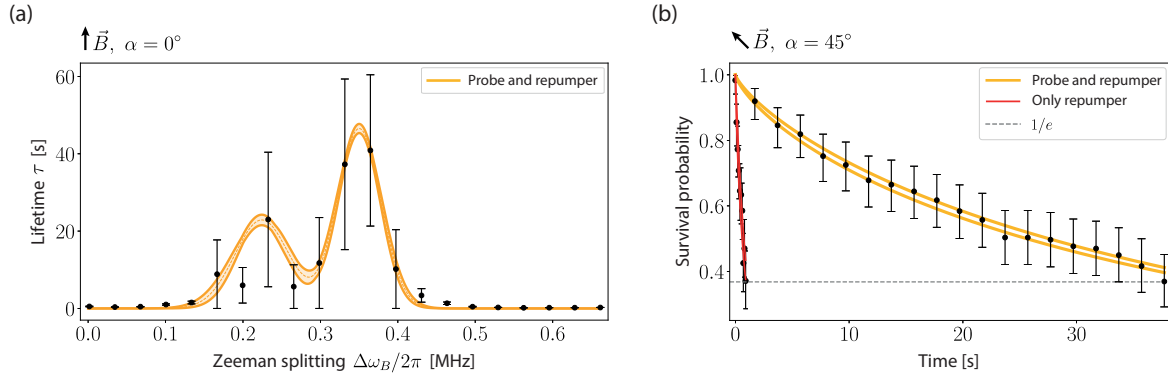
Figure 3.2: **(a)** A measurement of the atom trapping lifetime τ in dependence of the Zeeman splitting $\Delta\omega_B$ reveals degenerate Raman cooling whenever the absolute value of the magnetic field leads to a Zeeman level shift on the order of the average trap frequencies $\nu_x = \nu_y = (350 \pm 1)$ kHz and $\nu_z = (224 \pm 5)$ kHz. **(b)** Measurements of the survival probability at a fixed, but tilted magnetic field lead to drastically different lifetimes depending on whether optical pumping by probe light is present (yellow line) or not (red line). From a stretched-exponential fit (see Eq. 3.3), $1/e$ lifetimes (dashed, black line) of (42.9 ± 1.0) s and (1.0 ± 0.1) s are obtained, respectively.

reported [107]. In the first case it is straightforward to see that an atom prepared in $|F, m_F\rangle = |2, -2\rangle$ can undergo only four cooling cycles before it ends up in a dark state. Hence, long atom observation times probing the cycling transition are only possible in the presence of a repumper $|1\rangle \rightarrow |2\rangle$ and a dominantly σ^--polarized optical pumper (e.g. the probe field $|2\rangle \rightarrow |3'\rangle$), which pumps the atoms back towards the initial state, such that many more iterations are possible until the atom is in the ground state $|m = 0\rangle$.[1] It is worthwhile to point out a few subtleties involved in this scheme: Atoms in $F = 1$ are heated out of the trap in $F = 1$ due to the opposite sign of the Landé g-factor ($g_2 = -g_1 = 1/2$). For opposite probe light circularity, cooling is not observed at all for atoms in $F = 2$.

Aiming to establish degenerate Raman transitions as a robust standard cooling scheme to counteract lock laser induced heating, we measure the atom trapping lifetime τ in dependence of the Zeeman splitting, which is regulated by adjusting the current in the B_z coil [60]. The result is shown in Figure 3.2(a). The individual data points are obtained from lifetime measurements, during which all trapping and repumping fields are present and the probe light constantly interrogates the atom's presence. Their confidence intervals (CIs) are extracted via the bootstrapping method [116]. The error of the fit $f(x, \vec{y})$ with n parameters y_i and their one-sigma errors Δy_i is visualized by two enclosing curves

$$f_+(x) = \max\left[f(x, (y_1 + \Delta y_1, ..., y_i, ..., y_n)), ..., f(x, (y_1, ..., y_i, ..., y_n + \Delta y_n))\right],$$
$$f_-(x) = \min\left[f(x, (y_1 - \Delta y_1, ..., y_i, ..., y_n)), ..., f(x, (y_1, ..., y_i, ..., y_n - \Delta y_n))\right]. \tag{3.2}$$

As a model, we use the sum of two Gaussians, since the field configuration $\alpha = 0$ should lead to projections of DT_x (DT_y) on x (y) and z, respectively. It also takes into account that both resonances are affected by inhomogeneous broadening due to the distribution of atom positions in the 3D trap. At a splitting on the order of the average trap frequencies $\nu_x = \nu_y$ and ν_z, we expect an increase in the survival probability. In other words, $DT_{x,y}$ are cooling independently or even in combination with each other, but each in two dimensions. The magnetic-field to frequency calibration has been performed with microwave spectroscopy, which is briefly discussed in Section 3.3. As a first estimate, we obtain the trap frequencies

---

[1] Later on, we replace both optical pumping beams with 795 nm light (Sec. 2.4).

$\nu_x = \nu_y = (350 \pm 1)$ kHz and $\nu_z = (224 \pm 5)$ kHz, although one has to state that the data quality is affected by the long measurement time per point. In Section 3.2.2 we obtain more accurate values via Raman spectroscopy. A surprising outcome in Figure 3.2(a) is the absence of peaks towards higher splittings, which could be expected for an atom spending most of its time in $|F, m_F\rangle = |2, +2\rangle$. However, microwave spectroscopy shows a prevalent population in $|F, m_F\rangle = |2, -2\rangle$. One could argue that only $\sigma^\pm$-transitions are involved, such that $\Delta m_F = \Delta m = 2$ and cooling only takes place along z. The idea has to be discarded as well, since we also observe an effect on the survival probability of atoms in a 1D trap outside the cavity region; so the cooling has to take place along y as well. Summarizing, despite the absence of higher-order peaks in Figure 3.2(a), a trapping lifetime-enhancing process connected to degenerate Raman transitions is identified and leads to cooling in all dimensions.

In Figure 3.2(b), we try to maximize the cooling effect by tilting $\vec{B}$ to $\alpha = 45°$, which increases the σ-polarization component of the DTs. At the same time, we fix $\Delta\omega_B = 2\pi \cdot 0.35$ MHz. The error bars are given by the Clopper-Pearson CI [117] in accordance with our threshold-based state detection method described in [51, Sec. 5.2]. The data points are fitted with a stretched exponential of the type

$$\mathfrak{S}(t) = A\,e^{-(t/\tau)^n} \tag{3.3}$$

and its errors are visualized following Equation 3.2. While the function $\mathfrak{S}(t)$ is a phenomenological approach, it represents the global time evolution for a distribution of decay processes with independent amplitudes A_i and lifetimes τ_i well enough to optimize cooling parameters [118–120]. When the atoms are constantly repumped in the presence of probe light, an increased $1/e$ survival probability of (42.9 ± 1.0) s is observed. In the absence of nonstop probing, the average lifetime drops to (1.0 ± 0.1) s. In this case, the atoms do not necessarily escape all three traps[2], but they are no longer coupling to the resonator.

The drawback of the degenerate cooling scheme with $\alpha \neq 0°$ is, that the wave vector $\vec{k}_y$ of the red dipole trap DT_y is non-orthogonal to the quantization axis given by $\vec{B}$, leading to spurious effects: On the one hand, off-resonant fields without pure π-polarization give rise to higher-order energy shifts in the magnetic sublevels, which are known as vectorial light shifts [121, 122]. On the other hand, and more importantly, with a tilted magnetic field vector, polarization-sensitive addressing of individual atomic transitions is impossible. For $\alpha = 0°$, the robust technique of σ^--pumping by probe light transfers a majority of the atomic population into $|2, -2\rangle$. But to define a strong guiding field as required for addressing selected Raman transitions and to avoid heating processes as described in Figure 3.1(b), the Zeeman splitting has to be bigger than the individual trap frequencies. Therefore, we have to establish another cooling scheme.

3.2 Carrier–Free Raman Manipulation

Previously, resolved-sideband Raman cooling has been demonstrated in our apparatus in a 1D trap without cavity [52, 60]. Although this approach of two running-wave Raman beams is the most common one [123–125], we showed that in a CQED experiment the blue detuned standing-wave dipole trap created by lock laser light can also serve as a Raman beam. Furthermore, it allows for fundamentally lower temperature limits due to the absence of two-photon carrier transitions [63, 68]. In this section, we describe an adaption of this *carrier-free Raman manipulation* scheme in order to cool in three dimensions.

The dedicated Raman laser (Ω_R) at 770 nm is phase-locked to the lock laser (Ω_L) as the last element in the cavity lock chain, see Section 2.2. The frequency offset corresponds to the hyperfine splitting of

---

[2] Lifetime measurements in a 1D trap reveal lifetimes on the order of 10 s, pointing at heating effects specific to the cavity region.
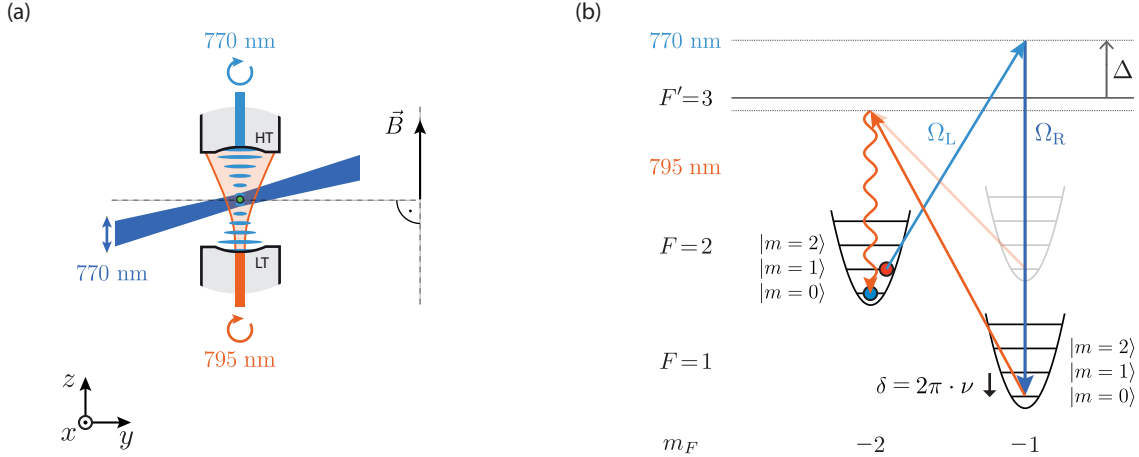
Figure 3.3: **(a)** The circularly polarized, blue detuned dipole trap drives Raman transitions in combination with a running-wave Raman laser propagating in the xy-plane. The quantization axis along the cavity is defined by a magnetic bias field. Circularly polarized light at 795 nm optically pumps the atom. **(b)** Illustration of resolved-sideband Raman cooling. The single-photon detuning of $\Delta = 3\Delta\nu_{\text{FSR}} = 2\pi \cdot 4.8$ THz is set by the lock laser, while the two-photon detuning δ between the Raman beams is given by the trap frequency ν. In order to cool the atom, we drive Raman transitions between the two well-isolated states $|2, -2\rangle$ and $|1, -1\rangle$, which lower the motional state from $|m\rangle$ to $|m - 1\rangle$. An incoherent repumper transfers the population back to $|2, -2\rangle$, where it is in a dark state with respect to the light fields as soon as $m = 0$ is achieved.

$\Delta_{\text{HF}} = 2\pi \cdot 6.835$ GHz plus a variable two-photon detuning δ. The associated optical setup is based on an OPLL [82, 126, 127] in a similar configuration as in [52]. While a fraction of the laser power is used for frequency stabilization, the majority is sent to the experiment as pulses for spectroscopy or cooling. The geometrical beam configuration for Raman cooling is displayed in Figure 3.3(a). The Raman laser is guided under a slight angle[3] diagonally through the xy-plane, which ensures that it has projections to both DT_x and DT_y. As a repumper, we now use only D_1 light at 795 nm, which propagates along the quantization axis defined by a magnetic bias field of ~ 1.8 G (see Sec. 3.3).

Figure 3.3(b) illustrates a cooling cycle. At a Zeeman splitting of $2\pi \cdot 1.25$ MHz and $\delta = 2\pi \cdot \nu$, we drive Raman transitions between the two well-isolated states $|2, -2\rangle$ and $|1, -1\rangle$, which lower the motional state from $|m\rangle$ to $|m - 1\rangle$. The virtual level is $\Delta = 3\Delta\nu_{\text{FSR}} = 2\pi \cdot 4.8$ THz blue detuned with respect to the probe transition. An incoherent repumper transfers the population back to $|2, -2\rangle$, where it is in a dark state with respect to the light fields as soon as $m = 0$ is achieved.

3.2.1 Raman Spectroscopy

With the intention to characterize the trap frequency ν_z in the simplest possible configuration, we perform Raman spectroscopy by sending the Raman laser along DT_y [69]. This trap is adiabatically lowered as soon as an atom is successfully transported to the cavity region and kept in $\text{DT}_{x,z}$, see Figure 3.4(a). Hence, only motional sidebands connected to z are expected. The experimental sequence consists of degenerate Raman cooling followed by an increase of the bias field in order to remove $|2, -1; m\rangle \rightarrow |1, 0; m'\rangle$ transitions from the spectrum. An optional waiting time of 100 ms is used to expose the atoms to heating effects. Subsequently, the state $|2, -2\rangle$ is prepared by optical pumping, followed by a short spectroscopy

---

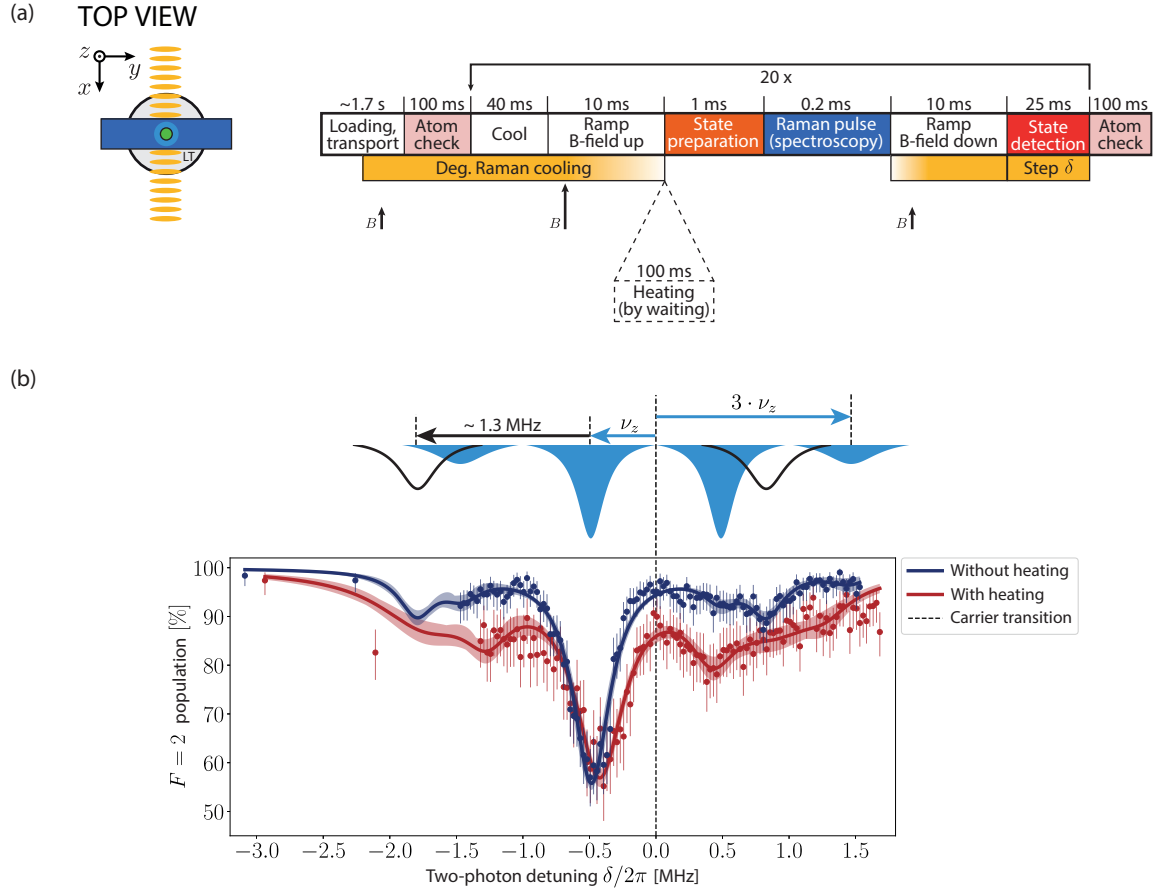[3] The axis is shared with the MOT optics, see Figure 2.1.

(a) **TOP VIEW**

(b)

Figure 3.4: Raman spectroscopy. **(a)** The running-wave Raman beam is sent along DT_y, which is ramped down adiabatically after the feedback transport. The intra-cavity standing wave given by the blue detuned lock laser light acts as the second Raman field for two-photon transitions. A flow diagram of the experimental sequence is shown to the right. For Raman spectroscopy, the magnetic field is increased to isolate the transitions depicted in Figure 3.3(b). For state detection and degenerate Raman cooling, it is reduced to fulfill Equation 3.1. **(b)** Schematic drawing of the expected sidebands ($\pm\nu_z, \pm 3\nu_z, ...$) along with the measured, carrier-free Raman spectra. The limited feedback bandwidth of the lock laser OPLL gives rise to additional sidebands (black line). Without heating the atoms (blue line), the mean motional excitation along z is measured to be $\overline{m}_z = (0.13 \pm 0.03)$, which indicates that the degenerate Raman cooling process is capable of cooling the atoms to the ground state. With heating (red line), the cooling sideband emerges on the right side of the absent carrier transition (black, dashed line).

pulse. The magnetic field is reduced to its original value, allowing for cooling during the cavity-assisted readout of the hyperfine state. The same atom is recycled for 20 iterations, during which the two-photon detuning δ takes different values. They are finally combined in the spectrum in Figure 3.4(b), where the data point uncertainty is given by the Clopper-Pearson CI. A sum of multiple Lorentzian dips is fitted to the data and the error is visualized by bands according to Equation 3.2.

Since the atoms are trapped at a standing wave node of the Raman field along z, the electric field amplitude is proportional to $\sin(k_z\hat{z})$ and the resonant coupling between the spin-motional states is described by

$$\Omega_{\uparrow m_y m_z, \downarrow m'_y m'_z} = \Omega_b |\langle \uparrow m'_y m'_z | \sin(\vec{k}_z \hat{z}) \, e^{i\vec{k}_y \hat{y}} \, \hat{\sigma}^\dagger | \downarrow m_y m_z \rangle|,$$

in analogy to [63]. $\hat{\sigma}^{\dagger} = |\uparrow\rangle\langle\downarrow|$ represents the spin raising operator, while the bare two-photon Rabi frequency is given by Ω_{b}. Since $\vec{k}_y \cdot \vec{k}_z \approx 0$, it follows that $\sin\left(\vec{k}_z\hat{z}\right) e^{i\vec{k}_y\hat{y}}$ is an asymmetric function along $\hat{z}$. Raman transitions therefore change the symmetry of the vibrational wave function, which imposes the selection rule $\Delta m_z = \pm 1, \pm 3, ...$ In the Lamb-Dicke regime, the geometry of the light fields can be expressed in first-order terms of harmonic oscillator raising $\hat{b}_z^{\dagger}, \hat{b}_y^{\dagger}$ and lowering operators $\hat{b}_z, \hat{b}_y$:

$$
\begin{aligned}
\sin\left(\vec{k}_z\hat{z}\right) e^{i\vec{k}_y\hat{y}} &\approx \left(\vec{k}_z\hat{z}\right)\left(\hat{\mathbb{1}}_y + i\,\vec{k}_y\hat{y}\right) \\
&= \eta_z\left(\hat{b}_z^{\dagger} + \hat{b}_z\right) + i\,\eta_y\eta_z\left(\hat{b}_z^{\dagger}\hat{b}_y^{\dagger} + \hat{b}_z\hat{b}_y^{\dagger} + \hat{b}_z^{\dagger}\hat{b}_y + \hat{b}_z\hat{b}_y\right),
\end{aligned}
\tag{3.4}
$$

with the Lamb-Dicke parameter $\eta = \Delta k_{\text{R}}\sqrt{\hbar/(2\,m_{\text{atom}}\,\omega_{\text{trap}})}$ and $\Delta k_{\text{R}} = |\vec{k}_z - \vec{k}_y|$ [113]. Without a trapping potential along $\hat{y}$, we hence expect the first and third order sidebands of z. They reveal a trap frequency of $\nu_z = 485 \pm 27$ kHz. In comparison to Section 3.1, we use a deeper optical lattice in order to simplify the sideband identification. Since we are driving the system strongly, another set of dips shows up, which is attributed to the OPLL servo bumps at ~ 1.3 MHz.[4] They mainly appear for the heating sideband of the z direction. The depth of the dips depends on the experimental details of the Rabi spectroscopy pulse and does not play a role in calculating the mean excitation number $\overline{m}_i$ along the direction i. Assuming a thermal equilibrium, it is given by the relation

$$
\overline{m}_i = \frac{R_i}{1 - R_i},
$$

where R_i is the ratio of cooling to heating sideband [63]. Since in the presented spectra the sidebands overlap, we extract the height ratio from the fitted amplitudes. The mean motional excitation along z is measured to be $\overline{m}_z = (0.13 \pm 0.03)$. Since the trap frequency along z is only slightly bigger than $\nu_{x,y}$, for which the Zeeman splitting was set, we conclude that the degenerate Raman cooling process is capable of cooling the atoms to the three-dimensional ground state. With the value of $\overline{m}_z$, a one-dimensional ground state population $m_{0,z} = 1/(1 + \overline{m}_z)$ of (88.5 ± 2.7) % is found.
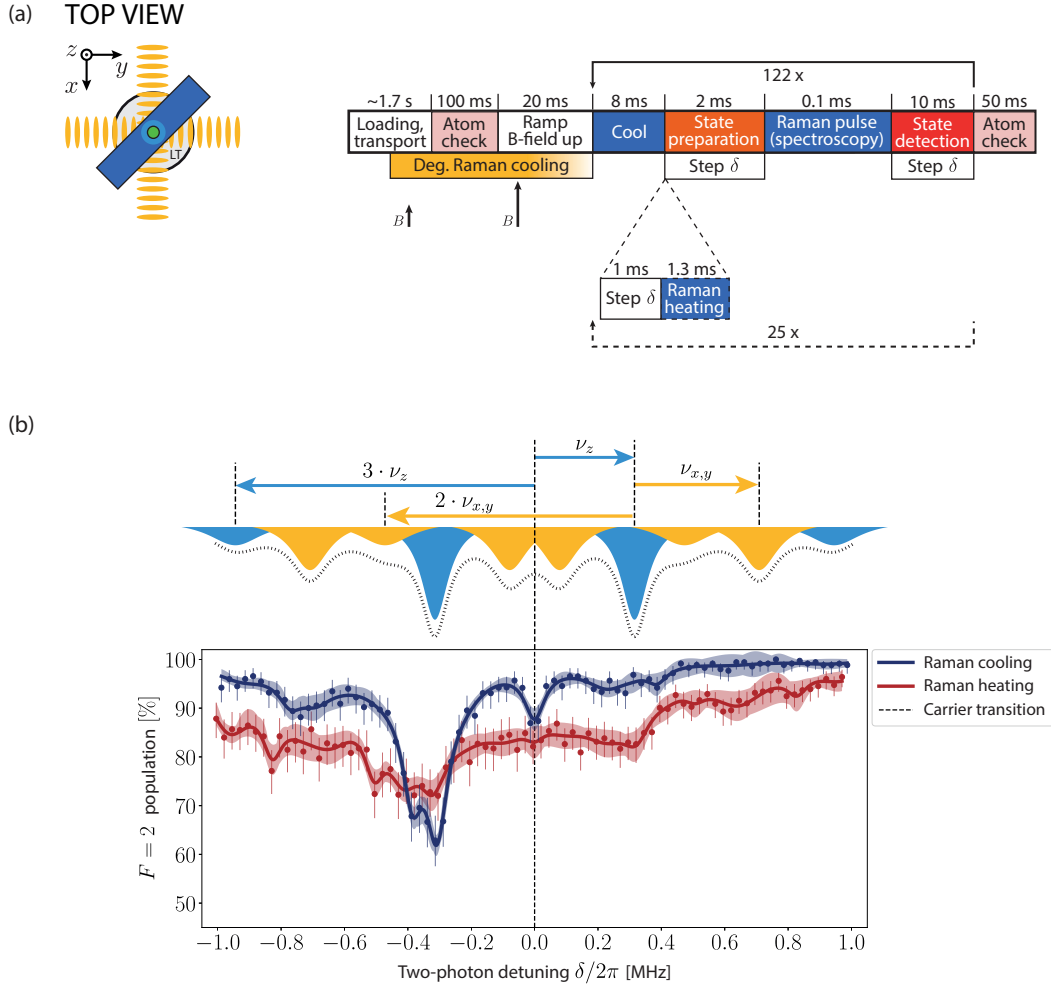
To observe an effect of the atom temperature on the spectrum, we introduce a waiting time before the spectroscopy pulse, which leads to a slightly shifted, overall broader and washed-out spectrum, in which the rise of the cooling sideband is clearly visible. In this case, the atoms leave the motional ground state up to $\overline{m}_z = (0.47 \pm 0.06)$.

3.2.2 Resolved–Sideband Raman Cooling

For the final cooling scenario, the trapping and Raman field configuration is shown in Figure 3.5(a). The running-wave Raman component travels diagonally through the xy-plane, such that sidebands in both red-detuned dipole traps are addressed. The experimental procedure is similar to the previous one, except for an additional resolved-sideband Raman cooling slot before the spectroscopy, for which we switch the value of δ. The optional heating is realized by driving a heating-sideband transition, which we call *Raman heating* and which requires switching δ as well. Overall, with now only a single ramp of the magnetic field, the sequence is much shorter and allows 122 (25) repetitions with the same, cold (hot) atom before it is lost – meaning that a full spectrum for each cold atom can be recorded within ~ 2 s.

Figure 3.5(b) schematically displays the expected, additional sidebands of $DT_{x,y}$, which are degenerate. Here, the trap frequency ν_z has been reduced, but if the intra-cavity trapping potential is too low, the atom loss increases. Experimentally we find, that a reduction to $\nu_z = (309 \pm 9)$ kHz is possible, while

---

[4] We were able to increase them to > 1.6 MHz by reducing the length of the electrical feedback loop (cf. spectrum in Fig. 3.5(b)).

Figure 3.5: Raman cooling. **(a)** The running-wave Raman beam is sent through the xy-plane such that it projects onto $DT_{x,y}$. The experimental sequence is extended by a Raman cooling pulse. To avoid waiting times, we address heating sidebands to record a spectrum for hot atoms. Since the guiding field can now take large absolute values during cooling, the procedure is shorter and allows for 122 iterations per atom loading. **(b)** The motional states of the red detuned dipole traps with equal trapping frequencies $\nu_x = \nu_y$ have to be taken into account. In the presence of Raman cooling pulses at a two-photon detuning $\delta_{\mathrm{cool}} = 2\pi \cdot 0.35$ MHz, the mean motional state numbers are given by $\overline{m}_z = (0.02 \pm 0.07)$ and $\overline{m}_{x,y} = (0.18 \pm 0.11)$. Details are found in the main text.

$\nu_{x,y} = (385 \pm 12)$ kHz is increased compared to the previous setting. In this trapping configuration, it is expected that Equation 3.4 segues into

$$\sin\left(\vec{k}_z\hat{z}\right) e^{i\vec{k}_y\hat{y}} e^{i\vec{k}_x\hat{x}} \approx \left(\vec{k}_z\hat{z}\right)\left(\hat{\mathbb{1}}_y + i\,\vec{k}_y\hat{y}\right)\left(\hat{\mathbb{1}}_x + i\,\vec{k}_x\hat{x}\right). \tag{3.5}$$

In reality, the angles of the red dipole traps give rise to a combined potential with new eigenmodes that are rotated by $45°$ relative to the individual lattices, which leads to first order sidebands along x, y in case of $\nu_z \approx \nu_{x,y}$. This increased dimensionality of Raman transitions in a slightly non-orthogonal optical lattice has also been discovered by Neuzner *et al.* [59]. Therefore, in the fit we do not only take into account the expected sidebands of Equation 3.5 up to the third order along z, but also the first (and second) order sidebands along x, y and the second order along z with its attributed higher order sidebands along x, y. The carrier transition is taken into account as well. It might be visible due to the sum of overlapping $\nu_{x,y}$-sidebands as well as the residual gravitational sag discussed in [68]. Additionally, the running-wave component of the cavity field is limiting the carrier suppression to $\mathcal{S} = 4\mathcal{F}/\pi \approx 10^4$, which is two orders of magnitude lower than in the previous high-finesse cavity, where we have observed an even higher ratio between carrier and heating sideband.

Previously, two-dimensional ground state cooling was achieved by tuning the trap frequencies [63]. We used a weaker, second order sideband of DT_y, which was overlapped with the first order cooling sideband along z, i.e. adjusting $\nu_y = 2\nu_z$ so that both directions were addressed simultaneously. As opposed to that approach, we tune the trap frequencies ν_z and $\nu_{x,y}$ almost into resonance, which enhances the motional coupling and allows three-dimensional ground state cooling. We observe that the detuning for cooling δ_{cool} is relatively insensitive, which allows us to address all cooling directions by setting $\delta_{\text{cool}} \approx 2\pi \cdot 0.35$ MHz. The mean motional state numbers are given by $\overline{m}_z = (0.02 \pm 0.07)$ and $\overline{m}_{x,y} = (0.18 \pm 0.11)$. This corresponds to a one-dimensional ground state population of $m_{0,z} = (97.8 \pm 7.1)\,\%$ and a three-dimensional one of $m_{0,\text{3D}} = m_{0,z} \cdot m_{0,(x,y)}^2 = (69.8 \pm 0.2)\,\%$.[5] In the presence of Raman heating, the motional state numbers change to $\overline{m}_z = (1.39 \pm 0.85)$ and $\overline{m}_{x,y} = (0.15 \pm 0.16)$. The number along x and y is very similar to the one obtained for the cold spectrum, which can be attributed to the clear uprising and broadening of the respective transitions. Hence, the motional state cannot be extracted accurately from the fit to the spread data any longer.

The cooling time slots to obtain these results have been longer than high repetition rate experiments demand (cf. sequence in Sec. 5.2.1). Problems of our scheme are, that on the one hand the far detuned Raman fields lead to a small two-photon Rabi frequency [129]

$$\Omega_b = \Omega_R \Omega_L / (2\Delta). \tag{3.6}$$

On the other hand, the atoms do not see a high intensity of Raman light along z since it simultaneously traps them in a node of the field, which is why we cannot use Equation 3.6 to determine Ω_b. However, an estimate of Ω_b and thus the rate at which we should be able to cool can be obtained from the area A of the sidebands according to

$$\Omega_b = \frac{1}{\eta_z}\sqrt{2\,\frac{A_{z,\text{heating}} - A_{z,\text{cooling}}}{\pi\,t_{\text{pulse}}}}, \tag{3.7}$$

which is derived in [59]. The requirement for this approach is a small pulse area along with the condition that the sideband area has to depend linearly on the duration of the spectroscopy pulse t_{pulse}. Comparing the first spectrum (cf. Fig. 3.4(a)) with a pulse duration of 0.2 ms to the cooling spectrum with

---

[5] In a similar experiment with running-wave Raman beams, $(89 \pm 2)\,\%$ have been achieved [128].

$t_{\text{pulse}} = 0.1$ ms, we see that the area decreases by a visible amount, which strengthens the assumption that we are in the linear regime. For the experimentally determined Lamb-Dicke factor $\eta_z \approx 0.16$ Equation 3.7 yields $\Omega_b \approx 2\pi \cdot 428$ kHz. For the first-order sidebands along z the Rabi frequency reduces to $2\pi \cdot 68$ kHz.[6] This result is in conflict with our observation of atom loss apart from millisecond-long cooling times (also in [68]). A scan of the repumping power versus the lifetime leads to the optimum repumping rate and avoids inefficient cooling to a certain extent. Notwithstanding these efforts, the technique of driving the cooling sideband longer than the decoherence time to shuffle the population between the F-states is not ideal. A better approach would be to apply alternatingly a Raman π-pulse and a follow-up repumping pulse [23].

A future improvement could be to use a standing-wave Raman field inside the cavity, which is closer to resonance and addresses the D_1 line [128]. As opposed to our scheme, the atoms are not localized at the minimum of light intensity. Another possibility is to give up on the resource-efficient carrier-free Raman cooling scheme and to address sidebands with free-space Raman beams. However, Raman cooling presently enables interesting options, such as the minute long, free-space imaging of atoms by probing the cavity only.[7] More importantly, the technique allows us to apply pulsed cooling, which enables long trapping lifetimes and pure m_F-state preparation, as we will see in the next section.

3.3 State Preparation and Microwave Spectroscopy

In order to accurately prepare the internal state of an atom, the transitions addressed by optical pumping [111] have to be selected. The effect of polarized light depends on the orientation of its propagation direction with respect to the quantization axis of the atom. We choose to define this axis by applying a magnetic field along z that breaks the degeneracy of the Zeeman manifold. It is created by *compensation coils*, which compensate the magnetic field of both earth and lab equipment, e.g. the ion pump [60]. By performing microwave (MW) spectroscopy, we identify the allowed microwave transitions shown in Figure 3.6(a). The Zeeman splitting $\Delta\omega_B$ between the m_f-levels is proportional to the absolute value of the weak, magnetic bias field $B = |\vec{B}|$ [51] and ensures that only selected states of the Zeeman manifold interact with each other during Raman processes (as in Sec. 3.2.2).

In the absence of any field, i.e. when all external fields are entirely compensated ($B_{x,y,z} = 0$), all microwave transitions are degenerate and state transfer is only observed for the MW frequency corresponding to the magnetic field insensitive transition number 4. We experimentally search for this spectrum and subsequently calibrate the conversion of coil current I_z to magnetic field strength $B_z(I_z)$ at the atom position. This allows to set a strong guiding field for which the frequency of the MW transitions is already known.

In the following, the state preparation efficiency in $|2, -2\rangle$ is investigated, as this is the initial state for the photon storage attempts in Section 6.2. The experimental sequence to prepare the state and to measure its population is shown in Figure 3.6(b). It consists of loading, transporting and cooling an atom, followed by a short state preparation and microwave spectroscopy pulse before the F-state is detected. The pulse duration of 5 ms is chosen to wash out any coherent Rabi oscillations. In particular, for the microwave manipulation we transport the atom $20\,\mu$m out of the cavity region to avoid fictitious magnetic fields, which arise from the circularly polarized lock laser field [51]. This transport along DT_x, perpendicular to the conveyor belt, is executed back and forth 44 times per atom, while each time the microwave frequency ν_{MW} is stepped.

---

[6] In the previous CQED setup we measured a heating-sideband Rabi oscillation frequency of $2\pi \cdot (38.2 \pm 0.4)$ kHz [63, 68].

[7] It might be interesting to vary the probe / lock laser frequency in order to measure the vacuum Rabi splitting in free-space rather than by cavity reflection.
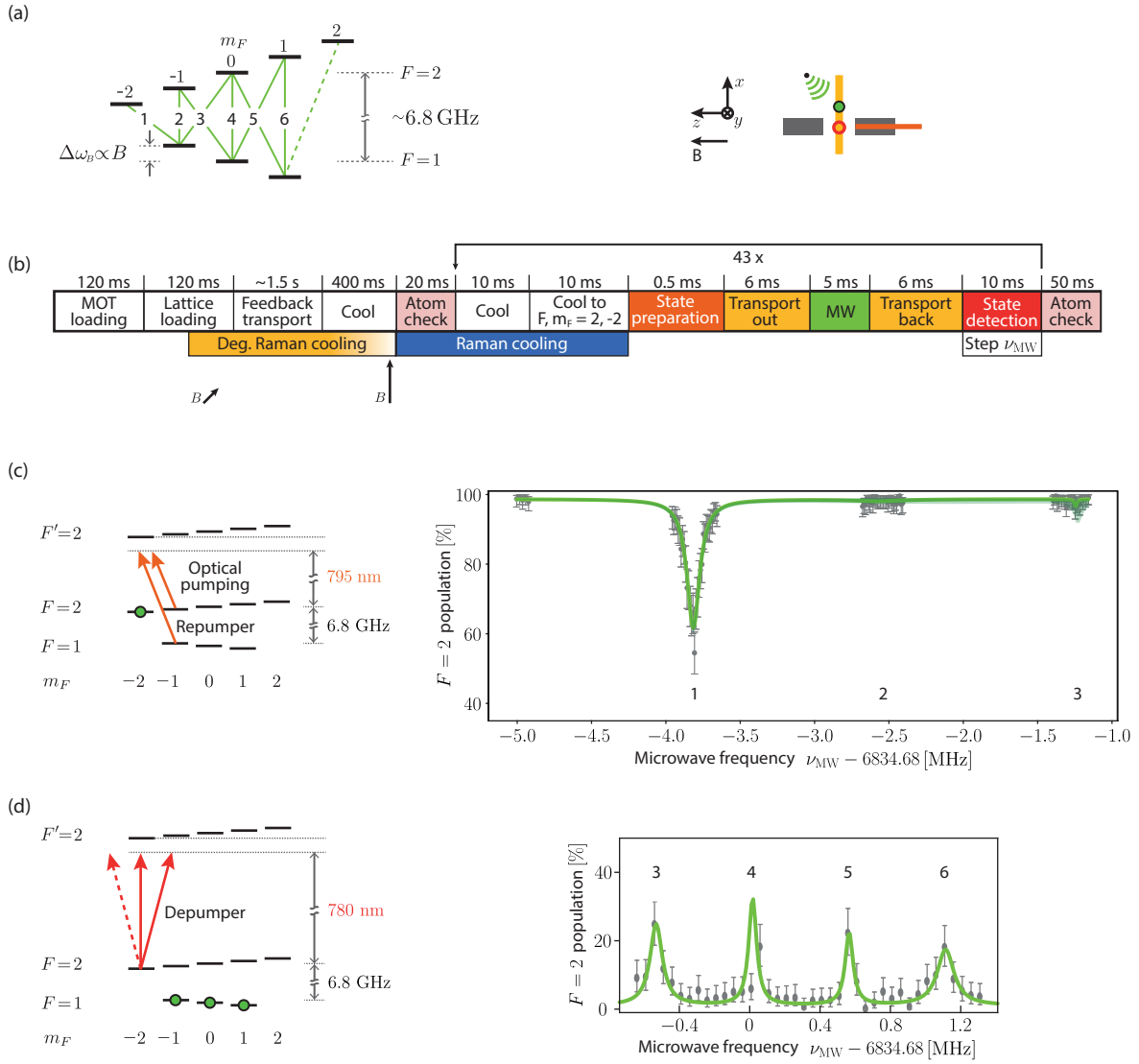
Figure 3.6: **(a)** Allowed microwave transitions between the Zeeman levels of the rubidium hyperfine ground states. In order to prevent inhomogeneous broadening of the individual transitions, the microwave pulses are applied outside the cavity region, while the state is prepared in the 3D dipole trap. **(b)** The sequence for optical pumping to $|2, -2\rangle$, which is needed for photon storage (see Sec. 6.2), uses both cooling mechanisms and an atom transport perpendicular to the conveyor belt. **(c)** The m_F-pumping efficiency using circularly polarized 795 nm light is determined by a fit of three equidistant Lorentzian curves. From the relative area of the dips we obtain an estimate for the state preparation efficiency, which is given by $\eta_{\text{state}} = (95.8 \pm 0.1)\,\%$. Due to its polarization, the microwave only addresses $\sigma^{\pm}$-transitions, which is why dip 1 is a measure for the population in $m_F = -2$ (and 3 for $m_F = -1$ and 0). **(d)** The population is depumped with 780 nm light of all polarizations. Here, the microwave is able to drive transitions 1-6, but its polarization is unknown. The resulting m_F-distribution over the entire $F = 1$ Zeeman manifold indicates that $m_F = 0, \pm 1$ have to be taken into account for our photon generation experiments (see Sec. 5.2). The data has originally been presented in [51] and is reprinted by courtesy of J. Gallego.

Figure 3.6(a) shows that in the presence of $B_z \neq 0$, only a single transition addresses the population in $|2, -2\rangle$. As a consequence of our guiding field of ~ 1.8 G, transition 1 will be driven by $\nu_{MW} \approx 3 \cdot 0.7$ MHz/G $\cdot$ 1.8 G $+ \Delta_{HF} \approx 3.8$ MHz $+ \Delta_{HF}$ [58]. To ensure that the microwave pulse addresses σ^--transitions, we align the MW waveguide to the quantization axis. The spectrum in Figure 3.6(c) reveals that indeed π-transitions (position 2) are suppressed and the population in $m_F = -1$ is only identified by transition 3 (along with population in $m_F = 0$). Reference points indicate that successful F-pumping is achieved in > 98 % of the cases. The m_F-pumping efficiency is determined by a fit of three equidistant Lorentzian curves. From the relative area of the dips we obtain an estimate for the state preparation efficiency, which is given by $\eta_{state} = (95.8 \pm 0.1)$ %.

In order to prepare the atoms for photon generation (see Sec. 5.2), we depump the population in $|2, -2\rangle$ by applying cross-polarized 780 nm light along DT_y such that $\sigma^{\pm}$ and π-transitions are addressed. The resulting m_F-distribution over the entire $F = 1$ Zeeman manifold is displayed in Figure 3.6(d) and has been originally presented in [51]. The difference here is that the microwave has driven the transitions 3 to 6 equally. For depumping, we use the more efficient D_2 transition since the D_1 light only depumps the population due to its finite polarization purity.

In conclusion, we have gained control over the internal and external states of a single atom coupled to the optical cavity. Properly defining the quantization axis along the resonator has enabled the preparation of an initial state for both photon generation and storage by optical pumping techniques. The two presented cooling mechanisms allow to work with well-coupled atoms for several seconds. To our knowledge, it is the first time that degenerate Raman sideband cooling is used to cool a single atom. Only recently, the extended carrier-free Raman cooling scheme has been found independently by Neuzner *et al.* and our team. With cooling – and thus tighter confinement – the average coupling strength between a single atom and the cavity has increased significantly compared to the previous setup [51, Sec. 4.2], as we will see in the measurements presented in Chapter 5. But in order to understand our system, we first focus on its theoretical description.

A Coherently Driven Multi–Level Atom in a Dissipative Cavity

THEORETICAL predictions on the behavior of N-level quantum objects coupled to quantized light-fields with n Fock states are a tough challenge for classical computers. Usually, they are described in the density-matrix formalism, which requires to solve differential equations with $(n \cdot N)^2$ dimensional matrices. It was not without reason that quantum systems themselves were proposed to simulate quantum, many-body phenomena [6, 130].

However, a classical computing approach is still possible if we reduce the complexity of our system. The preparations in Chapter 3 were based on this approach: We cooled the atoms to their motional ground state and initialized them in a well-defined Zeeman state, which is isolated by a strong guiding field. The latter also ensures a high purity for addressing polarization-sensitive transitions. As a consequence, the dynamics of our system can be approximated by a four-level atom coupled to a two polarization modes of an optical resonator.

This chapter is devoted to the development of a simulation which describes our experiments in the chapters to come in a simplified, yet qualitatively accurate way. In Section 4.1, we develop a model, which allows us to predict the evolution of three states and a single cavity mode at any point in time in order to understand underlying processes and to give an estimate of the efficiency of storing or generating a photon in this idealized system. In Chapter 6 we will discuss pulse sequences for photon storage in such a Λ-configuration. In contrast, a realistic description of our system is given by a four-level atom coupled to two resonator modes, which leads to different dynamics (Sec. 4.2).

Both models are implemented in a numerical simulation based on a full quantum-mechanical master equation, which is described in Section 4.3. We discuss our very own pulse optimization algorithm, which is used in the next chapter to explain the shape of generated photons.

4.1 The Evolution of an Open Quantum System

First, we start with the more intuitive scenario of a closed system: The well-known Jaynes-Cummings Hamiltonian [131] describes the interaction between two atomic levels and a quantized mode of an electromagnetic field. We extend this model to a three-level atom with two ground states $|g_{1,2}\rangle$ and one excited state $|e\rangle$, where only the transition from $|g_2\rangle \to |e\rangle$ with frequency ω_{a_2} is resonant with the cavity [105]. The Hamiltonian of this atom-cavity system consists of several parts:

$$\hat{H}_{JC} = \hat{H}_a + \hat{H}_c + \hat{H}_{int} \,,$$

where $\hat{H}_a$ and $\hat{H}_c$ are the separate Hamiltonians of atom and cavity mode, while $\hat{H}_{int}$ describes the interaction.

We treat the atom-photon interaction in both dipole- and rotating-wave approximations, and simplify the individual Hamiltonians by putting the dynamics in the frame of the pulse and Raman laser with frequencies $\omega_{p,R}$. The atom energy in the presence of a single-photon detuning $\Delta_{p\text{-}a} = \omega_p - \omega_{a_2}$ with respect to the excited state and a two-photon detuning $\delta = \Delta_{p\text{-}a} - (\omega_R - \omega_{a_1})$ with respect to the ground state $|g_1\rangle$ is given by:

$$\hat{H}_a = -\hbar \Delta_{p\text{-}a} \cdot \hat{\sigma}_{ee} - \hbar \delta \cdot \hat{\sigma}_{g_1 g_1}. \tag{4.1}$$

We introduce the raising and lowering operators $\sigma_{kl}^{\dagger} = |l\rangle\langle k|$ and $\sigma_{kl} = |k\rangle\langle l|$ which describe the excitation and de-excitation of the atomic spin, respectively.

The energy of the cavity field can be expressed in analogy to the spectrum of a harmonic oscillator by n Fock states $|0\rangle, ..., |n\rangle$. The creation- and annihilation operators $\hat{a}^{\dagger}$ and $\hat{a}$ add or remove a photon from the cavity mode ω_c, so that its energy for zero pulse-cavity detuning $\Delta_{p\text{-}c} = (\omega_c - \omega_{a_2}) - \Delta_{p\text{-}a} = \Delta_{c\text{-}a} - \Delta_{p\text{-}a} = 0$ reads:

$$\hat{H}_c = -\hbar \Delta_{p\text{-}c} \cdot \hat{a}^{\dagger}\hat{a} = 0. $$

The interaction term describes the coupling between the atomic dipole and the electric field of the cavity mode, which occurs with the Rabi frequency $2g$:

$$\hat{H}_{int} = i\hbar g \left(\hat{\sigma}_{g_2 e}^{\dagger} \hat{a} + \hat{\sigma}_{g_2 e} \hat{a}^{\dagger} \right). \tag{4.2}$$

We extend this model by two coherent, time-dependent driving terms, for which the overall Hamiltonian $\hat{H}(t)$ is given by

$$\hat{H}(t) = \hat{H}_{JC} + \hat{H}_d(t), \tag{4.3}$$

with the driving Hamiltonian

$$\hat{H}_d(t) = i\hbar \frac{\Omega(t)}{2} \left(\hat{\sigma}_{g_1 e}^{\dagger} - \hat{\sigma}_{g_1 e} \right) + \hbar \mathcal{E}(t) \left(\hat{a}^{\dagger} + \hat{a} \right). \tag{4.4}$$

The first term with $\Omega(t)$ stands for the control laser in a Λ-configuration and addresses the atomic transition which is off-resonant with respect to the cavity. The second term populates the cavity mode according to the driving strength $\mathcal{E}(t)$.

Without dissipative processes, i.e. the interaction of our system with the environment, we cannot control the ground state population of our system, as is intuitively clear from Equations 4.4 and 4.2: Any excitations brought into the system would lead to infinite oscillations between the states. The environmental states on the other hand are unknown, so we introduce the density matrix formalism to trace them out and to 'open' our system to loss channels. The Schrödinger equation is replaced by the master equation [132], which describes the density matrix $\hat{\rho}$ of our closed system at any point in time:

$$\frac{d\hat{\rho}}{dt} = \hat{\mathcal{L}}\hat{\rho} = -\frac{i}{\hbar}\left[\hat{H}, \hat{\rho}\right] + \hat{C}\hat{\rho}\hat{C}^{\dagger} - \frac{1}{2}\left(\hat{C}\hat{C}^{\dagger}\hat{\rho} + \hat{\rho}\hat{C}\hat{C}^{\dagger}\right). \tag{4.5}$$

The Liouvillian super-operator $\hat{\mathcal{L}}$ contains both the coherent dynamics given by Equation 4.3 and the Lindblad terms attributed to the decay and loss channels, which are specified by the collapse operator $\hat{C}$:

$$\hat{C} = \sqrt{2\gamma_1}\,\hat{\sigma}_{g_1,e} + \sqrt{2\gamma_2}\,\hat{\sigma}_{g_2,e} + \sqrt{2\kappa_{total}}\,\hat{a}. \tag{4.6}$$
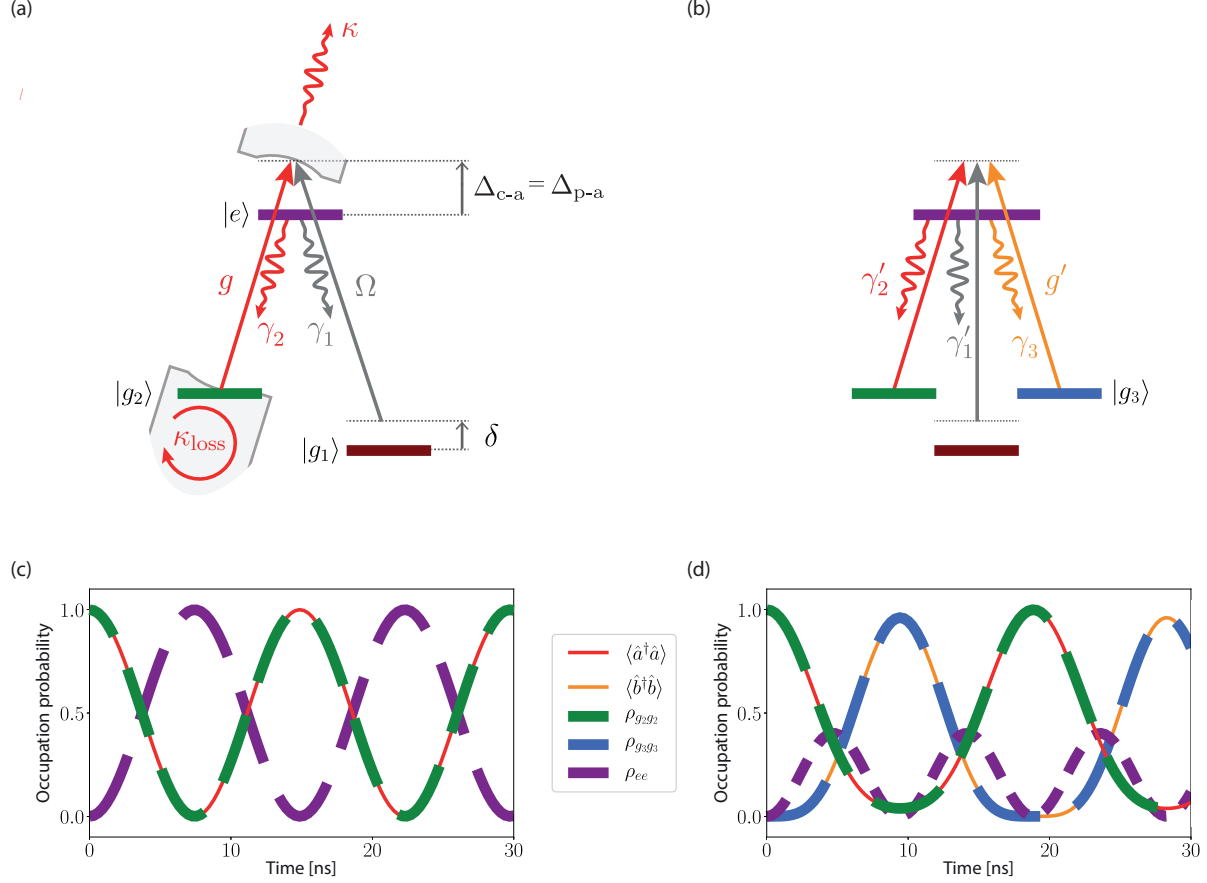
Figure 4.1: Abstract sketch illustrating all parameters our simulations depends on. **(a)** A three-level atom with two ground states $|g_{1,2}\rangle$ and one excited state $|e\rangle$ is placed inside a resonator and coherently driven by the pulse and Raman laser (cf. Fig. 2.3) with the respective Rabi frequencies $2g, \Omega$. Both cavity and pulse laser have a single-photon detuning $\Delta_{\text{c-a}} = \Delta_{\text{p-a}}$ with respect to the excited state. A resonant Raman condition is found for a two-photon detuning δ. The system has decay channels, of which κ is the transmission rate of the HT mirror and κ_{loss} is the absorption and scattering loss rate at the mirrors along with the undesired transmission of the LT mirror. The excited state decay $\Gamma = 2\gamma = 2(\gamma_1 + \gamma_2)$ re-populates both ground states. **(b)** To simulate our measurements, a four-level atom coupled to two $\sigma^{\pm}$-polarized cavity modes is required. We extend the previous model with an additional ground state $|g_3\rangle$ of equal energy as $|g_2\rangle$. It is coupled to the excited state with $2g'$. A new branching ratio $\gamma = \gamma_1' + \gamma_2' + \gamma_3$ has to be taken into account. In **(c)** and **(d)**, both models are compared: We consider an atom in the state $|g_2\rangle$ and $\langle \hat{a}^{\dagger} \hat{a} \rangle = 1$ at $t = 0$ and let the systems evolve coherently in the absence of decay processes (closed system). With $g = \sqrt{2/3}\,g' = 2\pi \cdot 34$ MHz, we observe the expected Rabi oscillations at a rate $2g/2\pi$ for the Λ-configuration, whereas in the *tripod configuration* the population oscillates between $|g_2\rangle$ and $|g_3\rangle$, since $g' \approx g$.

The transmission rate κ through the HT mirror and the unwanted damping of the field due to absorption, scattering at the mirrors and leakage through the LT mirror at rate κ_{loss} form the total cavity loss rate $\kappa_{\text{total}} = \kappa_{\text{loss}} + \kappa$. The excited state decay $\Gamma = 2\gamma$ to both ground states is considered with independent rates $\gamma_{1,2}$ such that $\gamma = \gamma_1 + \gamma_2$. An abstract sketch involving all parameters introduced until now is shown in Figure 4.1(a).

The conversion of modes on the outside of a resonator to modes on the inside is commonly treated by the *input-output formalism* [133, 134]. For mapping a weak coherent pulse with electric field probability amplitude $\phi_{\text{in}}(t)$ into the atom, we have to express the driving term $\mathcal{E}(t)$ in terms of $\phi_{\text{in}}(t)$ which contains on average n_s photons:

$$\mathcal{E}(t) = \sqrt{2\kappa} \cdot \sqrt{n_s} \cdot \phi_{\text{in}}(t). \tag{4.7}$$

Here, we have considered that $\phi_{\text{in}}(t)$ has a temporal shape of length T, to which it is normalized such that $\int |\phi_{\text{in}}(t)|^2 \, dt = 1$, and a mean number of photons n_s.

In summary, we have developed a model, which describes the temporal evolution of an idealized, three-level atom coupled to a resonator, including losses as well as driven excitations from the outside. We can extract information, e.g. about the average intra-cavity photon number $\bar{n} = \langle \hat{a}^\dagger \hat{a} \rangle$ at any point in time. In the case of single-photon generation, the simulation provides predictions for $\mathcal{E}(t) = 0$. In Section 6.1.2 we solve Equation 4.5 to investigate the efficiency of coherent-pulse storage in dependence of its various parameters. For $t > T$, the system reaches a steady state ($\hat{\mathcal{L}}\hat{\rho} = 0$), which allows us to define the storage efficiency η_{storage} by the atomic state population in $|g_1\rangle$:

$$\eta_{\text{storage}} = \frac{\rho_{g_1 g_1}}{n_s} = \frac{\langle \hat{\sigma}^\dagger_{g_1 g_1} \hat{\sigma}_{g_1 g_1} \rangle}{n_s}. \tag{4.8}$$

Leaving the regime of weak coherent pulses with on average one photon ($n_s = 1$), we explore the dynamics of true single-photon Fock-state storage by simulations in the limit $n_s \to 0$. Remarkably, the results for η_{storage} then correspond exactly to the predictions in [135, 136]: In the adiabatic storage regime of $TC\gamma \gg 1$, the storage efficiency is limited to:

$$\eta_{\text{max}} = \frac{C}{C+1}, \tag{4.9}$$

where $C = \frac{g^2}{\kappa \gamma}$ is the cooperativity parameter.

In [137], the - to our knowledge most recent - model to describe single-photon storage is unnecessarily complex, as it involves the coupling of several electromagnetic modes inside and outside the resonator. Besides collecting atomic population due to excited state decays (γ_i) in an auxiliary state outside the three-level atom[1], the main new aspect of that work is an analysis of the drop in efficiency caused by *parasitic losses* (κ_{loss}). In this situation, a new limit is found:

$$\eta'_{\text{max}} = \frac{\kappa}{\kappa + \kappa_{\text{loss}}} \frac{C'}{C' + 1}, \tag{4.10}$$

where $C' = \frac{g^2}{(\kappa + \kappa_{\text{loss}})\gamma}$ is the loss-modified cooperativity. For $\kappa_{\text{loss}} \neq 0$, we obtain efficiencies according to 4.10 as well[2]. But in our model, $\sum_i \rho_{g_i g_i} + \rho_{ee}$ is conserved, which is a more realistic case.

---

[1] Without explanation, but a benefit would be the ability to quantify the free-space loss.
[2] Indirectly visible in Figure 6.2(b), where η_{storage} is compared for κ and κ_{total}.

4.2 A Four–Level Atom Coupled to Two Cavity Modes

In our experiment, we are not dealing with a Λ-, but a *tripod* configuration [138]: The mediating excited state is coupled to both $\sigma^{\pm}$ cavity modes (cf. Fig. 5.1(b)). This means an additional state $|g_3\rangle$ of equal energy as $|g_2\rangle$ has to be taken into account, as shown in Figure 4.1(b). The corresponding operators acting on the photon number in the second cavity mode are $\hat{b}^{\dagger}$ and $\hat{b}$. Thus we have to update the Hamiltonian in Equation 4.2 and the collapse operator in Equation 4.6 to

$$\hat{H}'_{\text{int}} = i\hbar g \left(\hat{\sigma}^{\dagger}_{g2e}\hat{a} + \hat{\sigma}_{g2e}\hat{a}^{\dagger} \right) + i\hbar g' \left(\hat{\sigma}^{\dagger}_{g3e}\hat{b} + \hat{\sigma}_{g3e}\hat{b}^{\dagger} \right)$$

and

$$\hat{C}' = \sqrt{2\gamma'_1}\,\hat{\sigma}_{g1,e} + \sqrt{2\gamma'_2}\,\hat{\sigma}_{g2,e} + \sqrt{2\gamma_3}\,\hat{\sigma}_{g3,e} + \sqrt{2\kappa_{\text{total}}}\,\hat{a} + \sqrt{2\kappa_{\text{total}}}\,\hat{b} ,$$

with the new coupling strength g' and an adjusted branching ratio of the excited state decays γ_3 and $\gamma'_{1,2}$. In reality, there are more levels to decay to, but their respective transitions strengths are weak, such that we may neglect them. Additionally, the excited state population under coherent driving is very small at any time and $\kappa_{\text{total}} \gg \gamma_i$.

To illustrate the difference in the dynamics, we consider an atom in the state $|g_2\rangle$ and $\langle \hat{a}^{\dagger}\hat{a}\rangle = 1$ at $t = 0$ and let the systems evolve coherently in the absence of decay processes. The coupling strengths are chosen to match the special case $|e\rangle = |2', -1'\rangle$. Figure 4.1(c) shows the expected energy exchange between cavity mode a and the excited state $|e\rangle$ at a rate $2g/2\pi$. For the additional level and mode, the population starts to oscillate between the two states $|g_2\rangle$ and $|g_3\rangle$ (Fig. 4.1(d)). Since $g' > g$, there is always population left in $|g_2\rangle$. The excited state still gets populated, but the Rabi frequency is higher at cost of the contrast. As a consequence, the efficiency of coherent manipulations based on the excited state population will suffer, e.g. the π-flip storage of short photon pulses [135]. At the same time, a tripod configuration opens new possibilities, since every photon generation attempt creates entanglement between the emitted photon and the magnetic sublevels of the atom, which is e.g. useful for teleportation experiments [139] or the generation of entanglement between different platforms [26]. In [140], the properties of such a system are investigated and the creation of two-mode Schrödinger-cat states in the cavity is proposed.

The cooperativity parameter C is defined for a single atom-cavity coupling rate only, and in our example above one can see that the energy-exchange rate between atom and cavity modes has increased by a factor of ~ 1.5. We are not aware of any generalized rate depending on g and g', so for any tripod-based calculation of C we give the lower-bound cooperativity value by considering the rate g only.

4.3 Simulating our System: Numerical tools and optimization methods

Exact analytical solutions to the master equation 4.5 are only possible in special cases. In general, a numerical approach is the easier choice. We use *QuTiP* (v4.1), the *Quantum Toolbox in Python* (v3.5) [141, 142] to facilitate the process of setting up state vectors, time-(in)dependent Hamiltonians and (super-)operators and to solve Equation 4.5 with the in-built function *mesolve*. Based on an ordinary differential equation solver, it evolves the density matrix and returns a time-binned array of expectation values for a list of operators. The calculation is based on the absence of correlations between system and environment (separability), a weak interaction with the environment such that it does not change upon interaction with the system (Born approximation), much faster dynamics in the environment i.e. 'no memory' (Markov approximation) and the negligence of fast rotating terms in the interaction

picture (secular approximation).

Searching for the highest storage efficiency, we implement optimal control techniques [143]. *QuTiP* also dedicates a part of its code to *Quantum Optimal Control*, a set of functions implementing *Chopped RAndom Basis* (CRAB) [144] and *GRadient Ascent Pulse Engineering* (GRAPE) [145] algorithms for pulse optimization[3]. These techniques are based on standard optimization methods of which many are already implemented in *Python*, e.g. the *Broyden–Fletcher–Goldfarb–Shanno* algorithm (BFGS). While it is straightforward to set up a problem, the interpretation of results given by QuTiP sometimes is not. For us it turned out to be more practical to develop our own optimal control scheme, which is used to fit obtained pulse shapes (Sec. 5.2.2) and to search for the highest transfer probability (Sec. 6.1.3).

We call it *Basin hOpping Pulse Optimization* (BOPO). Basin-hopping [146] is a stochastic algorithm which is similar to the well-known *Simulated Annealing* (SA) algorithm. It is a meta-heuristic, probabilistic technique, which tries to determine the global minimum of a cost function in a large parameter space by accepting also worse solutions. As opposed to gradient-based search algorithms, it is less liable to ending up in a local minimum.

The algorithm iterates through cycles composed of random perturbation of the parameters, local optimization by a routine to be specified and acceptance or rejection of the parameter set P based on the cost function value. We apply the *Nelder-Mead method* [147], also known as *downhill simplex method*, for the local optimization. Based on the concept of simplices, it approximates local optima by evaluating cost values along the $P + 1$ points of a volume and introducing variations such that the cost value decreases.

We determine the optimal storage parameters with a cost function C_{storage} defined as:

$$C_{\text{storage}} = 1 - \eta_{\text{storage}}\left(\vec{\Omega}, \vec{\delta}\right) + \sum_j \mathfrak{C}_{\Omega_j} + \sum_k \mathfrak{C}_{\delta_k}, \qquad (4.11)$$

where $\vec{\Omega}$ is a time-array of amplitudes, that is interpolated before handing it to *mesolve*, and each entry Ω_j is constrained by $\mathfrak{C}_{\Omega_j}$. Likewise, the corresponding two-photon detunings $\vec{\delta}$ are treated and limited by $\mathfrak{C}_{\delta_k}$. Using a set of interpolated amplitudes is far more reasonable than the common approach of using Fourier components, as it reduces the parameter space significantly. A problem of Equation 4.11 is that single Ω_j entries are likely to take non-zero, divergent values without significantly improving the storage efficiency. They are identified by solving Equation 4.5 with $\vec{\Omega}\,\big|_{\Omega_j=0}$. If η_{storage} does not decrease below a certain threshold, the value Ω_j will be set to zero. The same procedure is repeated for δ_k's. The underlying idea is that single, less relevant amplitude points are not supposed to make use of the entire dynamic range of the pulse modulator. In this case, the important features would be compressed to a low-transmission window, for which distortions of the waveform are observed (cf. Fig. 5.2(a)).

If we are interested in the interpretation of generated single-photon pulse shapes, we use a fit model based on the cost function $C_{\text{retrieval}}$:

$$C_{\text{retrieval}} = \bar{n}_{\text{exp}}(t) - n_0 \cdot \bar{n}\left(t, \tau_\Omega, \Omega(t), \Delta, g_{\text{dist}}\right), \qquad (4.12)$$

where the average photon number $\bar{n}(t)$ given by the simulation depends on the mean value of $\Delta = \Delta_{\text{p-a}}$ and the driving Rabi frequency $\Omega(t)$ and its pulse delay τ_Ω. The experimentally determined variation in coupling strengths is implemented as a distribution g_{dist}, over which we average along with the different initial m_F ground states. $\bar{n}$ is scaled with n_0 in order to reduce the difference of $\bar{n}(t)$ and the measured average detector counts $\bar{n}_{\text{exp}}(t)$. Once the simulation finds the parameters to recreate $\bar{n}_{\text{exp}}(t)$, we can estimate the efficiency of photon generation by $\rho_{g_2 g_2}$ in the steady state.

---

[3] In [137], GRAPE was used for pulse optimization.

Deterministic Generation and Shaping of Single Photons

Tʜᴇ generation of single photons has been studied on a variety of platforms [148]. An important figure of merit is the rate, at which photons are delivered. Here, the efficient collection of a considerable fraction of the created photons plays a crucial role and often leads to the approach of enclosing the emitter by a resonator [149–151][1]. Miniature fiber-cavities with their intrinsic coupling between light-guiding glass fiber and resonator mode are an excellent choice and have been combined with well-known solid-state emitters such as nitrogen-vacancy centers [153, 154], carbon nanotubes [155] and quantum dots [156, 157]. As a proof of principle, we have demonstrated that – under continuous illumination – our system delivers single photons as well [39, 51].

Of high interest is the triggered generation of single photons along with a controlled waveform, which can facilitate information processing or enhance the storage probability of the generated photons in another medium [158]. Shaping of single photons was first shown in an ion-trap cavity system [149] and has advanced up to the point where time-bin entanglement [159] in the form of photonic qubits, qutrits and ququads has been realized [160]. In Section 5.1, the basics for single-photon production are presented. Subsequently, we show that we do not only control the shape of triggered, single photons, but also reach a faster extraction of photons from the cavity-coupled atom than possible in free-space (Sec. 5.2.2). The quantum nature of the emitted light is demonstrated in a Hanbury Brown-Twiss (HBT) experiment [161] and presented in Section 5.2.3.

The observed efficiency is discussed in Section 5.2.4. Since we cannot access the cavity-based, non-destructive state detection [51] in a Λ-configuration, we employ the photon generation as a method of fast state detection to determine the photon storage efficiency in Section 6.2.

5.1 The Atom–Cavity System as a Source of Single Photons

A direct and simple $\sigma^{\pm}$-photon emission into the cavity modes is already triggered by a pulsed, π-polarized laser with a $\vec{k}$-vector perpendicular to the cavity and quantization axis, as shown in the schematic Figure 5.1(a). In this case, the wave-packet envelope is fixed and given by the temporal shape of the cavity field decay [162]. For more sophisticated shapes, the atomic population has to undergo a *vacuum-Stimulated Raman Adiabatic Passage* (vSTIRAP) [163, 164], for which a Λ-configuration is required, such that all involved states $|F\rangle$, $|F'\rangle$ fulfill $|F - F'| \leq 1$. The choice of levels resonant with the cavity has an impact on the maximum generation efficiency: For example, the D_2 line can outperform the

---

[1] An alternative, less efficient way is to use high aperture lens objectives (HALOs), with e.g. a 12 % collection efficiency [152].
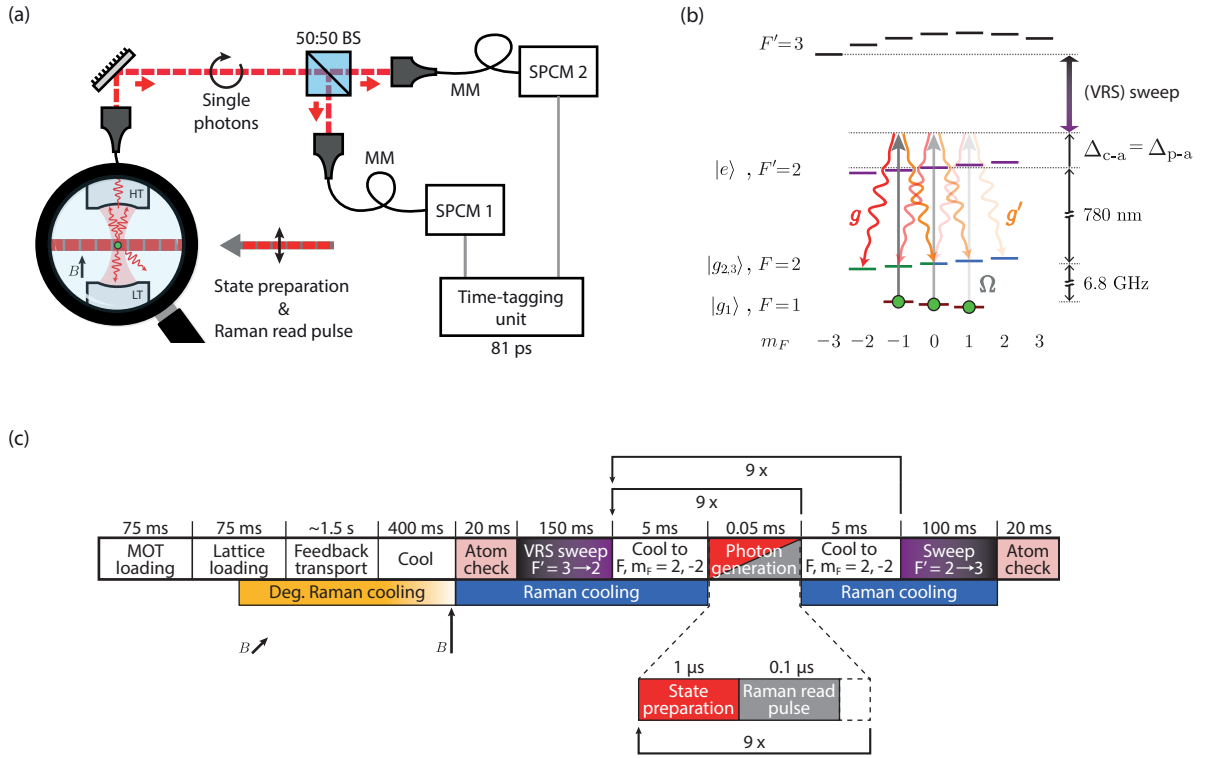
Figure 5.1: **(a)** The atomic state is prepared by short optical pumping pulses (red) along the conveyor belt (cf. Fig. 2.1). Subsequently, a *Raman read pulse* (gray) generates a photon in the cavity mode in a vSTIRAP process. With a certain probability (Sec. 5.2.4), the photon leaks through the HT mirror and is detected by one out of two SPCMs in a Hanbury Brown-Twiss configuration. The time-tagging unit allows to reconstruct pulse shapes and to verify the single-photon emission of the triggered photon generation. **(b)** Level scheme of ^{87}Rb for photon generation on the D_2 line, including Zeeman and AC Stark shifts, whereby the latter are caused by $DT_{x,y}$. As indicated by faint arrows, the atom in $|F = 1\rangle$ has several possibilities of emitting into the two cavity modes $g \approx g'$ (red and orange) when driven by a Raman laser Ω in a tripod configuration. The nomenclature from Chapter 4 is shown as well. **(c)** Flow diagram of the experimental sequence for photon generation. The loops sum up to 500 generation attempts per 3 s sequence time. The effective duty cycle is limited by the atom loading procedure and the cooling efficiency, but within the actual pulsing window the photon-production rate is ~ 2 kHz.

D_1 line [19], where the strongest Λ-compatible coupling transition is $|1\rangle \rightarrow |1'\rangle$. We use $|2\rangle \rightarrow |2'\rangle$ instead, which is in the m_F-average weaker by $\sqrt{2}$, but allows to address the strongest cycling transition, which we need to measure the atom-cavity coupling strength. In addition, we choose to couple the hyperfine ground states via a virtual level that is $\Delta_{p\text{-}a} = \Delta_{c\text{-}a} = 2\pi \cdot 90$ MHz blue-detuned with respect to the excited state $|F' = 2\rangle$. This is not necessarily required for the generation process, but for photon storage experiments this setting helps to suppress the incoherent storage component.

In a Λ-configuration, the shape of the control laser pulse defines the temporal envelope of the generated photon. As discussed in Section 4.2, the presence of two cavity modes – both accessible due to $\kappa \gg \Delta\omega_B$ – prevents a clean Λ-configuration. Instead, the coupled levels form a tripod. While this has no effect on the photon generation efficiency, the obtained shape is no longer fully congruent with the expected one, for which the control laser pulse is designed. Since the deviations turn out to be marginal and compensable by adjustments of the control Rabi frequency, we discuss and derive pulses from this approach despite the mismatch. Another encouraging argument is, that in the adiabatic generation regime, the pulse length

T is much longer than the cavity damping time ($T \gg 1/\kappa_{\text{total}}$), which ensures that $F = 1$ is depopulated. The final m_F-state is of minor relevance, since we aim to generate photons of indefinite polarization.

Furthermore, we have to take into account a total of 3x2 possibilities of emitting a photon into one of the two cavity modes, which is shown in the level scheme in Figure 5.1(b). This leads to variations of the dipole matrix elements, which has to be considered in a simulation of the system.

5.2 Shaping Single Photons

The STIRAP technique is well-established. While numerous reviews discuss applications, recommended references are the recent, comprehensive tutorial given by Bruce Shore [165] and the review of Vitanov *et. al.* [138]. For our system, the most crucial benefits of this technique are first, the ability to shape the cavity photon(s) n by designing the temporal amplitude of the Raman read pulse $\Omega(t)$ and second, the high efficiency with which the mechanism converts a single photon of the laser beam to a single photon in the cavity by following a *dark atom-field state* $|D\rangle$, which prevents occupation of $|e\rangle$:

$$|D\rangle(t) = \cos\vartheta(t)\,|g_1, n\rangle - \sin\vartheta(t)\,|g_2, n+1\rangle \,,$$

where $\vartheta(t)$ is the mixing angle defined by

$$\tan\vartheta(t) = \frac{\Omega(t)}{2g\sqrt{n+1}} \,.$$

The adiabatic condition is fulfilled if cavity and driving laser provide $2g\,T(n+1) \gg 1$ and $|\Omega\,T| \gg 1$, respectively. A more practical condition, as $\Omega(t)$ is usually not the limiting parameter, is adapted from [135]:

$$TC'\gamma \gg 1 \,, \tag{5.1}$$

where C' is the loss-modified cooperativity as discussed in Section 4.1. This inequality is easily fulfilled for either appropriate (long) pulse lengths or a system in the strong coupling regime (or even more intuitively: $T \gg \kappa_{\text{total}}^{-1}, g^{-1}$). In these cases, generation efficiencies close to unity are expected. We face the strong coupling regime at its border, as indicated in Figure 2.4. Thus a minor excited state population can occur and lead to scattering of photons into free-space. Part of the generated photons leave through the HT mirror and become a traveling-wave photon ϕ_{out} (see Sec. 5.2.4). A reasonable choice for the pulse length T are 100 ns, leading to the lower bound value $TC'\gamma = 18$. This leaves the question: How do we find $\Omega(t)$ such that a desired electric field shape $\phi_{\text{out, des}}(t)$ is obtained?

One possibility is to find a simple, analytic solution based on the Schrödinger equation for an atom-cavity system under assumption of population conservation [166]. For an estimated efficiency close to unity, $\Omega(t)$ is analytically calculated from a set of coupled equations:

$$c_{g_2} = -\frac{\phi_{\text{out, des}}(t)}{\sqrt{2\kappa}}$$

$$c_e = -\frac{i}{g}\left(c_{g_2}(t) + \kappa\,\dot{c}_{g_2}(t)\right)$$

$$\rho_{g_1g_1}(t) = 1 - \rho_{ee}(t) - \rho_{g_2g_2}(t) - \int_0^t \left(2\,\gamma\,\rho_{ee}(t') + 2\,\kappa\,\rho_{g_2g_2}(t')\right) dt'$$

$$\Omega(t) = -i\frac{\dot{\rho}_{g_1g_1}(t)}{c_e(t)\,\sqrt{\rho_{g_1g_1}(t)}} \,,$$

where $c_i(t)$ and $\rho_{ii}(t) = c_i(t)c_i^*(t)$ are the probability amplitude and population of the state i, respectively (nomenclature see Ch. 4).

The second option is to exploit *time reversal symmetry* which holds true in the regime of adiabatic state transfer. This can be understood in terms of a passive beam-splitter-like transformation, in which the mapping from a certain input to an output mode – including the atomic states – is considered [135, 167]. A more intuitive example is given by the loading of a photon into an empty, single-sided cavity [91, 168]: Only if the resonator is 'filled' with an exponentially rising pulse, i.e. the time reversal of the cavity decay, the field directly reflected at the entrance mirror and the field leaking out of the cavity will interfere destructively at any point in time. As a consequence, the cavity mode will be populated most efficiently.

Following the time-reversal approach, in order to *generate* a photon of shape $\phi_{\text{out, des}}(t)$, we reverse the temporal envelope of $\Omega_D(t)$ which is required to *store* a photon of the shape $\phi_{\text{out, des}}(t)$. The discussion of the origin of $\Omega_D(t)$ is postponed to Section 6.1.1, where we introduce several ways of calculating the driving Rabi frequency for photon storage.

To calculate the $\Omega_D(t)$, we used $\gamma = 2\pi \cdot 3$ MHz, the measured value of $\kappa_{\text{total}} = 2\pi \cdot 41$ MHz and a coupling strength of $g_0 = 2\pi \cdot 34$ MHz, which originates from the VRS measurement and is scaled by $\sqrt{1/6}$ to match the $|2, -2\rangle \rightarrow |2', -1\rangle$ transition. The single-photon detuning of $\Delta_0 = 2\pi \cdot 90$ MHz has been heuristically implemented as described in Section 6.1.1 and is set taking the dipole-trap light shifts into account.

5.2.1 Measurement Sequence and Repetition Rate

The experimental procedure starts by loading a single atom into the cavity trapping region ($\eta_{\text{load}} = 70\,\%$), determining its coupling strength to the resonator and cooling it to the motional ground state. Then, the trigger generator (Sec. 2.5) releases a short sequence of five state preparations in $|F = 1\rangle$ (Sec. 3.3), each one followed by a $T = 100$ ns long *Raman read pulse*[2]. The loops visible in Figure 5.1(c) are a result of optimizing the sequence for the highest possible atom survival, which is on the order of 40 % due to the limited Raman cooling efficiency. Along with the atom loading procedure, we end up having 1000 generation attempts per 3 s, which corresponds to a rate of ~ 2 kHz in the actual pulsing window. Rates of 1 MHz have been shown for a much shorter window of $100\,\mu$s [160], hampered by an atomic fountain as a source of atoms. In ion-cavity systems, the superior trapping conditions lead to impressive 100 kHz rates over 90 min [149]. Provided that the cooling scheme is improved as discussed in Section 3.2.2, this rate is a realistic expectation for our system as well, with a production time limited by the background pressure.

The generated photon stream is split by a 50:50 beam splitter and guided to two fiber-coupled SPCMs. Their detection signals are recorded by the time-tagging unit mentioned in Section 2.5, which allows to correlate the sum of detection events with the time-tagging trigger in order to obtain the pulse shape. A correlation of the detection events between the two channels is used to check for a single-photon signature.

5.2.2 A Sine–Squared Shape and a Triple–Peak Pulse

We aim to generate photons with a simple target envelope given by

$$\phi_{\text{out, des}}(t) \propto \sin^2(\pi \cdot t/T) \tag{5.2}$$

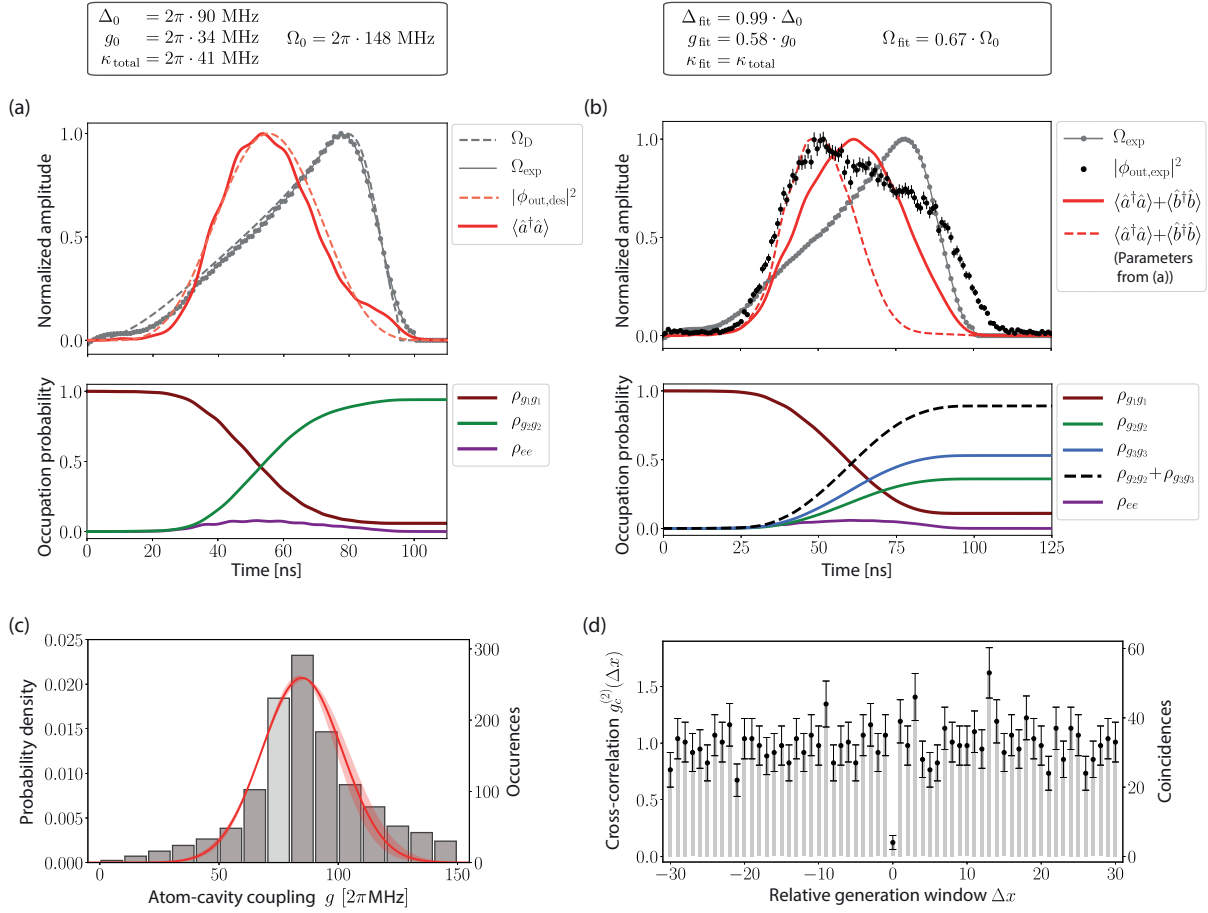[2] In the context of a memory, the Raman laser *writes* and *reads* the information.

Δ_0	$= 2\pi \cdot 90$ MHz	
g_0	$= 2\pi \cdot 34$ MHz	$\Omega_0 = 2\pi \cdot 148$ MHz
κ_{total}	$= 2\pi \cdot 41$ MHz	

$\Delta_{\text{fit}} = 0.99 \cdot \Delta_0$	
$g_{\text{fit}} = 0.58 \cdot g_0$	$\Omega_{\text{fit}} = 0.67 \cdot \Omega_0$
$\kappa_{\text{fit}} = \kappa_{\text{total}}$	

Figure 5.2: Generation of single photons with a temporal envelope given by a sine squared as in Equation 5.2. All pulse shapes are normalized. **(a)** We compare the calculated Rabi frequency $\Omega_{\text{D}}(t)$ (dashed, gray line) with the measured $\Omega_{\text{exp}}(t) \propto \sqrt{I}$ (solid, gray line). For the given parameters and $\Omega_{\text{exp}}(t)$, we simulate the Λ-system and find a good agreement between the resulting intra-cavity photon number $\langle \hat{a}^\dagger \hat{a} \rangle$ (solid, red line) and the desired intensity profile $\left| \phi_{\text{out, des}}(t) \right|^2$ (dashed, red line). A small kink towards the end of the pulse is caused by the heuristically implemented single-photon detuning Δ_0 in Equation 6.1. The occupation probability ρ_{ii} of the involved atomic levels is shown below and gives insight into the dynamics. **(b)** The reconstructed, experimental photon shape $\left| \phi_{\text{out, exp}}(t) \right|^2$ (black) differs from the desired shape. The error bars are given by the square root of the number of detected photons. To this day, the deformation cannot be explained by our tripod-configuration based simulation and a fit (solid, red line) as described in Equation 4.12. The fit parameters are displayed above and a detailed discussion is found in the main text. Below, the system dynamics obtained from the fit are shown. For comparison, a simulation (dashed, red line) based on the parameters from (a) is shown as well (cf. Fig. 6.7). **(c)** In a VRS sweep, we determine the individual atom-coupling strength g for each sequence repetition. The distribution of values is shown with a Gaussian fit and 1σ confidence intervals. Each value still has to be scaled by $\sqrt{1/6}$ to match the $|2, -2\rangle \rightarrow |2', -1\rangle$ transition. As discussed in the main text, a specified range of coupling strengths (highlighted area) is used for post-selection in (d) and for an accurate implementation of g in our simulation in (b), where the displayed data has not been post-selected. **(d)** The cross-correlation $g_{\text{c}}^{(2)}$ of detected photons according to Equation 5.5 reveals $g_{\text{c}}^{(2)}(0) = (12.2 \pm 6.5)$ %, if post-selection with $g \in [70, 80] \cdot 2\pi$ MHz is applied. In this case, only single atoms are present. As our correlation is limited to $g_{\text{c,bg}}^{(2)}(0) \approx (13.6 \pm 0.1)$ % by detector dark- and background counts, the measurement confirms that our system indeed delivers single photons. Another pulse shaping attempt is presented in Figure 5.3.

and a more complex, modulated outline

$$\phi_{\text{out, des}}(t) \propto \sin^2\left(\pi \cdot t/T\right) - \sin^2\left(\pi \cdot 2\,t/T\right) \,. \tag{5.3}$$

Both are normalized such that $\int \left|\phi_{\text{out, des}}(t)\right|^2 dt = 1$ and restricted to $t \in [0, T]$. From the calculated $\Omega_{\text{D}}(t)$, we obtain the peak Rabi frequency Ω_0. Since $\Omega_0 \propto \sqrt{I}$, we simply need to adjust the CW power for the fixed beam waist of $30\,\mu$m.

Using the pulse shaping setup and a separate SPCM, we compare the normalized shapes of both measured and calculated Rabi frequencies $\Omega_{\text{exp}}(t)$ and $\Omega_{\text{D}}(t)$ in Figures 5.2(a), 5.3(a)[3]. The generated pulses follow very closely the desired contour, and only for lower transmission values of the intensity modulator the pre-compensation fails (see Sec. 2.5). In the most important region along the slopes[4], the shapes are in excellent agreement.

We simulate a three-level atom with the aforementioned parameters and time-dependent driving fields to verify that our simulation is capable of producing the expected shapes of the output photon. We compare the evolution of the intra-cavity photon number $\langle \hat{a}^\dagger \hat{a}\rangle(t)$ with the desired intensity profile $\left|\phi_{\text{out, des}}(t)\right|^2$. At any point in time they are proportional, since the field leaks out of the cavity at the rate κ:

$$\left|\phi_{\text{out, des}}(t)\right|^2 = 2\kappa \cdot \langle \hat{a}^\dagger \hat{a}\rangle(t) \,. \tag{5.4}$$

Besides a minor delay, the most prominent feature is an additional kink at the end of the pulses, better visible for the fast modulation. It originates from the single-photon detuning and its heuristic implementation. The formalism, according to which we design the pulses, was originally intended for $\Delta_0 = 0$. In this case, the simulated pulse perfectly follows the desired shape. Another aspect of the simulation is that we are able to understand the dynamics between the three atomic levels: The excited state population is theoretically negligible and a smooth transfer from $|g_1\rangle$ to $|g_2\rangle$ takes place.

The measured generated pulses $\left|\phi_{\text{out, exp}}(t)\right|^2$ are shown in Figures 5.2(b), 5.3(b). We immediately see the deviation from the target outline which manifests in a broadening and, for the adiabatic generation, in a kink towards the end. For the fast retrieval in Figure 5.3(b), we pick the center peak to calculate the $1/e$-time of the rising slope, since it bears the best contrast. We obtain < 12.5 ns, which is faster than the excited state decay time constant $\tau_e = 26.2$ ns [58] by a factor of 2. In other words, the photon extraction is faster than in a free-space scenario and ultimately limited by the cavity intensity-damping time constant of $1/(2\kappa_{\text{total}}) = 1.9$ ns.

In order to understand the discrepancy of the shape, we use Equation 4.12 to fit the data as explained in Section 4.3. The simulated system is a four-level atom coupled to a resonator with two polarization modes $a\,(\sigma^+, g)$ and $b\,(\sigma^-, g')$. As free fit parameters we leave the Rabi frequency amplitude of the Raman pulse Ω_{fit}, its delay and the single-photon detuning Δ_{fit}. The scaled coupling strength g_{fit} includes the measured distribution shown in Figures 5.2(c), 5.3(c) and g' is derived by the ratio of the respective transition strengths. Some of the measured g-values exceed the calculated maximum single-atom coupling strength of $g \approx 120 \cdot 2\pi$ MHz (see Table 2.1), which means that a small two-atom contribution has to be considered in the number of produced photons (Sec. 5.2.3).

Since in the experiment we manipulate a real atom which can initially populate any m_F-state, we average over a set of three branches as shown in Figure 5.1(b) in order to describe it theoretically. The respective transition strengths and excited state decay ratios are taken into account. This approach is

---

[3] For the sake of completeness, I always mention both figures for general statements, but regarding one of them while reading the main text is sufficient.
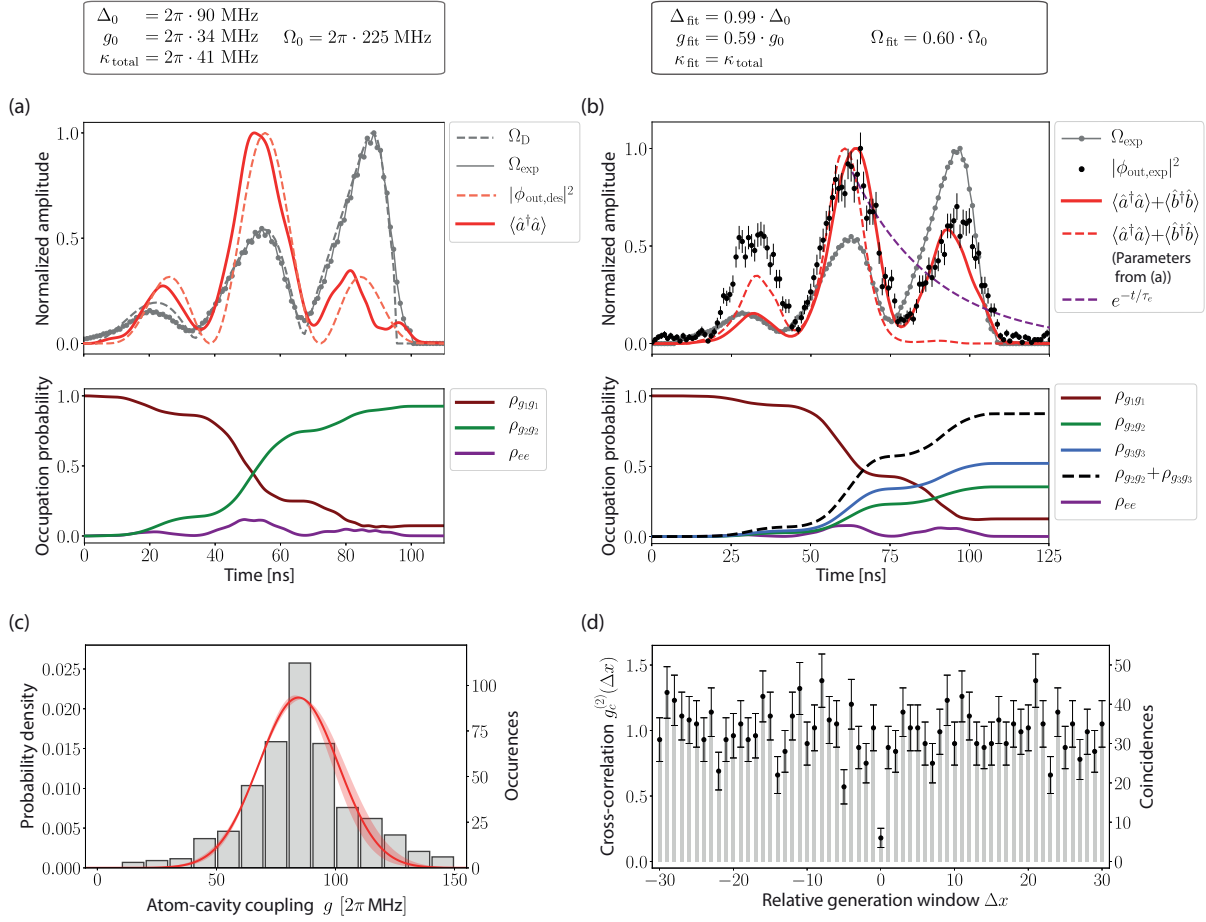
[4] See explanation in Sec. 6.1.1.

$$\Delta_0 = 2\pi \cdot 90 \text{ MHz}$$
$$g_0 = 2\pi \cdot 34 \text{ MHz} \qquad \Omega_0 = 2\pi \cdot 225 \text{ MHz}$$
$$\kappa_{\text{total}} = 2\pi \cdot 41 \text{ MHz}$$

$$\Delta_{\text{fit}} = 0.99 \cdot \Delta_0$$
$$g_{\text{fit}} = 0.59 \cdot g_0 \qquad \Omega_{\text{fit}} = 0.60 \cdot \Omega_0$$
$$\kappa_{\text{fit}} = \kappa_{\text{total}}$$

Figure 5.3: Generation of single photons with a temporal envelope given by a modulation as in Equation 5.3. All pulse shapes are normalized. **(a)** We compare the calculated Rabi frequency $\Omega_{\text{D}}(t)$ (dashed, gray line) with the measured $\Omega_{\text{exp}}(t) \propto \sqrt{I}$ (solid, gray line). For the given parameters and $\Omega_{\text{exp}}(t)$, we simulate the Λ-system and find a good agreement between the resulting intra-cavity photon number $\langle \hat{a}^\dagger \hat{a} \rangle$ (solid, red line) and the desired intensity profile $\left| \phi_{\text{out, des}}(t) \right|^2$ (dashed, red line). A small kink towards the end of the pulse is caused by the heuristically implemented single-photon detuning Δ_0 in Equation 6.1. The occupation probability ρ_{ii} of the involved atomic levels is shown below and gives insight into the dynamics. **(b)** The reconstructed, experimental photon shape $\left| \phi_{\text{out, exp}}(t) \right|^2$ (black) differs from the desired shape. The error bars are given by the square root of the number of detected photons. To this day, the deformation cannot be explained by our tripod-configuration based simulation and a fit (solid, red line) as described in Equation 4.12. The fit parameters are displayed above and a detailed discussion is found in the main text. Below, the system dynamics obtained from the fit are shown. For comparison, a simulation (dashed, red line) based on the parameters from (a) is shown as well. An interesting aspect of this shape is the – not yet limited – $1/e$ time constant, at which we modulate the Rabo frequency and thus the photon. With < 12.5 ns, it is shorter than the excited state decay time constant $\tau_e = 26.2$ ns [58] by a factor of 2 (cf. purple, dashed line). **(c)** In a VRS sweep, we determine the individual atom-coupling strength g for each sequence repetition. The distribution of values is shown with a Gaussian fit and 1σ confidence intervals. Each value still has to be scaled by $\sqrt{1/6}$ to match the $|2, -2\rangle \rightarrow |2', -1\rangle$ transition. As discussed in the main text, the information can be used for post-selection and for an accurate implementation of g in our simulation in (b). Here, the displayed data has not been post-selected. **(d)** A cross-correlation $g_{\text{c}}^{(2)}$ of detected photons according to Equation 5.5. Two-atom contributions are present and the amount of data is insufficient for post-selection. A detailed discussion of the single-photon character is found in Section 5.2.3. Another pulse shaping attempt is presented in Figure 5.2.

valid considering the atom has to start in one of the three subspaces and is at any time also restricted to it – this heavily reduces the computational load for our simulation.

With our model, we have not yet been able to explain the observed curve. To this point, we can exclude an influence of the excited states $F' = 1$ and 3, timing jitters of the pulses, insufficient EOM suppression, a drift of Ω_0 on long timescales by regarding only initial and final measurement traces[5], a drift on short timescales by averaging only the first and last 50 attempts over the traces and a 'washing out' by distributions of Δ_0, g_0 and/or Ω_0. In [20], post-selection on the coupling strength has been suggested. We have tried selecting only the g-value for which $\Omega(t)$ is designed, but there has not been any clear influence on the shape. This also means, that the contribution of two-atom cases has no significant effect on the shape. Moreover, a simulation for the assumed value of g_0 and the designed $\Omega(t)$ actually predicts a much faster read-out, which is nicely visible in Figure 5.2(b). This behavior is expected, since the overall cavity coupling is enhanced with two modes. Instead, we see that the pulse is broadened, suggesting an overall lower atom-cavity coupling and driving Rabi frequency.

Assuming that our intensity modulator has a residual phase shift component which causes a frequency chirp of $\Omega(t)$, we have modified the simulation by introducing the time-dependent single-photon detuning

$$\Delta(t) = \frac{\pi}{2} \, \alpha_0 \, \frac{1}{\Omega_0} \, \frac{d\Omega(t)}{dt} \, ,$$

with a chirp parameter α_0 as discussed in Section 2.5 and [89]. For $\alpha_0 > 1$, the shapes mainly become narrower, since state transfer only occurs close to a two-photon resonance. For $\alpha_0 \leq 0.1$, as specified by the manufacturer, the effect has been barely visible. Furthermore, two-photon detunings in a range of a few tens of MHz have not had any considerable effect, as expected for a high-bandwidth cavity.

The temporal occupation of both cavity modes is identical (except for the amplitude), so even if polarization-dependent detection efficiencies were present, there would be no influence on the shape.

Only an unjustified assumption of two discrete values of Ω_0, over which we average, fits to the data. The reason is obvious considering Figure 5.3(b): First we read out in the beginning, second at the end, such that overall the ratio between side- and center peaks is reduced. We are not aware of any experimental aspect that justifies this assumption and conclude by pointing out that the unexpected behavior of generated photon pulse envelopes is also unclarified in another experiment with a similar theoretical framework [169]. However, in Section 6.2 we generate pulses on resonance, i.e. with $\Delta_{\text{c-a}} = 0$, and are perfectly able to explain the shape.

5.2.3 A Quantum of Light

A prominent process to generate single photons is spontaneous parametric down-conversion of a pump photon with high energy into a pair of photons of lower energy. In this process, the pump power as well as the length of the non-linear medium can lead to multi-photon emission [170]. However, in our tripod configuration the probability of receiving more than one photon per read pulse and emitter is practically zero, since the excitation laser frequency is far-detuned from the emission frequency. But in order to identify the presence of more than one atom, it is interesting to regard the normalized cross-correlation $g_{\text{c}}^{(2)}(\Delta x)$ between photon detections in SPCM 1 and 2. If the individual SPCM sees c_i counts in the 100 ns generation window x, $g_{\text{c}}^{(2)}$ is defined as:

$$g_{\text{c}}^{(2)}(\Delta x) = \frac{1}{m} \frac{\langle c_1(x) \, c_2(x + \Delta x) \rangle}{\langle c_1(x) \rangle \, \langle c_2(x) \rangle} \, , \tag{5.5}$$

---

[5] As a reminder; a single *trace* uses the same atom for 500 *attempts* to generate a photon.

where $\overline{m}$ is the average number of coincidences for $\Delta x \neq 0$.

In Figures 5.2(d), 5.3(d), we show the detection coincidences for a shift of Δx windows along with the Poissonian error given by the number of coincidences. At $\Delta x = 0$, the dip is expected to reach zero for a perfect single-photon source [171, 172], but it is usually limited by the dark count rates of the SPCMs and by Raman-scattered lock laser light. These two effects are combined into the rates $x_{d_1} = (3.00 \pm 0.03)$ kcps and $x_{d_2} = (1.20 \pm 0.01)$ kcps in order to give the estimate

$$g_{c,bg}^{(2)}(0) \approx \frac{\eta_{\text{retrieval}} \left(x_{d_1} + x_{d_2} \right)}{\left(\eta_{\text{retrieval}}/2 + x_{d_1} \right) \left(\eta_{\text{retrieval}}/2 + x_{d_2} \right)} = (13.6 \pm 0.1)\,\% \,,$$

which is derived from Equation 5.5 for equal SPCM detection efficiencies and the probability of detecting a photon per triggered pulse $\eta_{\text{retrieval}} = (2.3 \pm 0.1)$ %. For all g-values in Figure 5.2(c) we find $g_c^{(2)}(0) = (20.9 \pm 3.4)$ %, which means the contrast is not background limited, but most likely constrained by a small two-atom component[6]. In order to filter the spurious events, we post-select the data for $g \in [70, 80] \cdot 2\pi$ MHz (highlighted in Fig. 5.2(c)). As can be seen from Figure 5.2(d), the value $g_c^{(2)}(0) = (12.2 \pm 6.5)$ % is then closer to the background limit, as expected. The bottleneck for giving precise $g_c^{(2)}(0)$ estimates is the number of measurements – in Figure 5.3(d) the measurement time is shorter, therefore the correlation is shown for all g-values. The outcome of these measurements suggests that relying on the pre-selection by the feedback transport might not be sufficient, if we aim to work with a single atom. Also, only in combination with further measurement techniques such as the cross-correlation we can identify the single-atom coupling strengths in their measured distribution.

5.2.4 Photon Generation Efficiency

As already mentioned, the probability of detecting a photon per triggered pulse is $\eta_{\text{retrieval}} = (2.3 \pm 0.1)\%$. This number contains the underlying efficiency of generating a photon inside the cavity mode $\eta_{\text{generation}}$, which can be traced back by calibrating the state preparation efficiency η_{state}, the relative transmission through the HT mirror η_{HT}, the spatial mode-matching between cavity and fiber η_{mm}, the losses in the optical path η_{path} and the SPCM detection efficiency η_{det}:

$$\eta_{\text{generation}} = \frac{\eta_{\text{retrieval}}}{\eta_{\text{state}} \cdot \left(\eta_{\text{HT}} \cdot \eta_{\text{mm}} \cdot \eta_{\text{path}} \cdot \eta_{\text{det}} \right)} \,. \tag{5.6}$$

Optical pumping via the D_2 line has a probability of $\eta_{\text{state}} = (80 \pm 10)$ % to prepare the atoms in the initial state. This is a consequence of the fast repetition rate for which the experiment was built, without knowledge about the final limitation due to insufficient cooling. As discussed in Section 4.1, the input-output coupling depends on the cavity linewidth κ. From a transmission measurement of the HT mirror and [37], we derive:

$$\kappa = \frac{\Delta \nu_{\text{FSR}}}{2} \cdot \mathcal{T}_{\text{HT}} = 16 \cdot 2\pi \text{ MHz} \,,$$

with $\mathcal{T}_{\text{HT}}, \Delta \nu_{\text{FSR}}$ listed in Table 2.1. Along with the measured bandwidth of $\kappa_{\text{total}} = 41 \cdot 2\pi$ MHz, this means significant losses of $\kappa_{\text{loss}} = 25 \cdot 2\pi$ MHz are present and lead to $\eta_{\text{HT}} = \kappa/\kappa_{\text{total}} = (39 \pm 1)$ %.

The mode matching efficiency has been measured in [38] to be $\eta_{\text{mm}} = (60 \pm 2)$ %. This leaves only the optical path, which we calibrated for the measurements in [39] to be $\eta_{\text{path}} = (38 \pm 13)$ %, and the SPCM

---

[6] In this discussion, we omit the additional influence of the ~ 50 ns detector dead time, since the probability of detecting both photons and background counts in the 100 ns windows is very small. As a side remark, after-pulsing of the detectors also plays a role. In accordance with measured probabilities of 1.8 and 0.3 %, we detect a dead-time limited number of 19 two-fold photon events in a single SPCM for the measurement in Figure 5.2.

quantum efficiency of $\eta_{\text{det}} = (50 \pm 5)$ %.

Combining all of these numbers, we obtain $\eta_{\text{generation}} = (66.4 \pm 25.2)$ %, which covers the expected value given by $C'/(C' + 1) = 90$ % with its error margin mostly due to the uncertain path efficiency. To retrieve the probability of generating a photon at all, $\eta_{\text{generation}}$ in turn has to be divided by $C'/(C' + 1)$. Whereby one must keep in mind that the expected efficiency is defined for a three-level atom, as discussed in Section 4.2.

The efficiency of generating a photon in the cavity mode also corresponds to $\int_0^T \left|\phi_{\text{out, des}}(t)\right|^2 dt$ (see Eq. 5.4), and could be obtained from the simulation by a fit to the experimental data. The atomic state transfer between the ground states gives the probability of generating a photon at all, including scattering into free-space. The ratio of both numbers could give an estimate for the Purcell factor in the tripod configuration.

In conclusion, we achieved a deterministic generation of single photons and estimated the generation efficiency, which is particularly useful for the photon storage process, in which success is indicated by a retrieved photon. This can also be used as a method of fast state detection [173], in which a probe photon is energetically converted into a detection photon. By controlling the temporal envelope of the read pulse, we control the shape of the emitted photon and achieve an extraction speed beyond the free-space scenario. Since we are not yet able to fully predict the outcome by our simulation, a next step would be to repeat the measurements and to record more data, such that a combination of different post-selection methods is possible, e.g. a restriction of g-values and regarding only the first 50 attempts simultaneously. If the origin of the distortion cannot be identified, desired shapes will still be obtained by iterative, measurement-based adjustments to the control pulse. For resonant photon generation, as performed in Section 6.2, the output shape can be perfectly explained.

In order to boost the overall detection probability $\eta_{\text{retrieval}}$, we are currently working on new fiber cavities with *GRaded-INdex* (GRIN) lenses that promise a mode-matching efficiency near unity [174]. Simultaneously, we will investigate the finesse degradation discussed in [51, Appendix A.2] to reduce the cavity losses κ_{loss}. Along with small improvements in the optical path an efficiency of $\eta_{\text{retrieval}} > 10$ % should ultimately be feasible.

Light–Pulse Storage in Atom–Cavity Systems

O VER the past decade, the storage of light pulses in atomic systems has been shown for ultra-cold [175–179] and ambient temperature gases [180]. The demonstration of single-atom quantum memories for polarization qubits encoded in weak, coherent pulses has been pursued as well [23, 24, 181]; even down to the level of single photons [25, 182]. While these experiments constitute impressive results, the prestigious goal of storing photons emitted by quantum dots in order to exploit cross-platform benefits (see Ch. 1) has not been achieved yet [183].

A first step towards such a *hybrid experiment* has been the direct photonic coupling of an ion-cavity system with a quantum dot [184]. In order to overcome the bandwidth mismatch between the two systems, the properties of the laser were imprinted on the photonic emission by working in the Heitler regime [185]. However, this means that the single photons are no longer deterministically triggered. A better approach for the efficient storage of high-bandwidth photons is the usage of an open cavity with a sufficiently large coupling strength beyond the intermediate regime ($2g > \kappa_{\text{total}} - \gamma$ [51]) – like the one employed for the presented experiments.

In order to fully absorb an input light pulse, the temporal envelope of the storage-assisting control laser has to be matched to its shape [186]. For designing the control pulse, we first consider the more intuitive adiabatic regime and introduce two analytic approaches to find the correct time-varying Rabi frequency $\Omega(t)$ in a Λ-configuration (Sec. 6.1.1). In Section 6.1.2, we use our previously introduced simulation framework to show the dependence of the storage efficiency on various pulse parameters. At the same time, we find and develop two numerical approaches to optimize $\Omega(t)$ in the fast storage regime, where the pulse length approaches the cavity field decay time. One of them relies on the recurring trend of *optimal control* (Sec. 6.1.3). As a last theoretical remark, the question whether the storage has a significant coherent component is answered in Section 6.1.4.

At the end of this chapter, we experimentally demonstrate the control laser-assisted storage of a short coherent pulse at the single-photon level (Sec. 6.2). Furthermore, we compare the measured storage efficiencies for different control-pulse parameters with the theoretical expectation.

6.1 Adiabatic and Fast Storage in a Lambda Configuration

In this section, we start with reviewing and extending two prominent storage protocols based on adiabatic transfer in a Λ-configuration, for which $TC'\gamma \gg 1$ has to be fulfilled (cf. Eq. 5.1). For short input pulses, we find that a temporal compression of the write pulse and subsequent parameter scans using our simulation (see Ch. 4) lead to a storage efficiency comparable to that obtained by optimal control techniques. All simulations use the measured parameters of our system, i.e. $(g_0, \gamma) = 2\pi \cdot (34, 3)$ MHz,

where g_0 is the weakest coupling strength of the allowed $|2, m_F\rangle \rightarrow |2', m_f \pm 1\rangle$ transitions. For now, $\kappa = 2\pi \cdot 25$ MHz is assumed[1]. In the discussion of the expected efficiencies, the cavity losses are included with $\kappa_{\text{loss}} = 2\pi \cdot 16$ MHz, such that κ_{total} is once more $2\pi \cdot 41$ MHz.

6.1.1 Adiabatic Storage Schemes

Dilley *et al.* proposed an analytical method for finding the control pulse Rabi frequency $\Omega_{\text{D}}(t)$ required to capture a single photon of arbitrary temporal shape with an atom coupled to a single-sided optical cavity [136, 187], which is based on the approach of *impedance matching* [188]: At any point in time, the photon reflection on the input mirror (HT) has to be zero. This is expressed in terms of the input-output formalism [133], which Dilley *et al.* implement in the master equation of the coupled atom-cavity system in matrix form:

$$\begin{pmatrix} \dot{c}_{g_1} \\ \dot{c}_e \\ \dot{c}_{g_2} \\ \phi_{\text{out}} \end{pmatrix} = \begin{pmatrix} 0 & -i\,\Omega_{\text{D}}^*/2 & 0 & 0 \\ -i\,\Omega_{\text{D}}/2 & i\,\Delta_0 - \gamma & -i\,g_0 & 0 \\ 0 & -i\,g_0^* & -(\kappa + \kappa_{\text{loss}}) & \sqrt{2\kappa} \\ 0 & 0 & \sqrt{2\kappa} & -r \end{pmatrix} \begin{pmatrix} c_{g_1} \\ c_e \\ c_{g_2} \\ \phi_{\text{in}} \end{pmatrix}, \tag{6.1}$$

where r is the reflectivity of the HT mirror and c_i denotes again the probability amplitude of the state i. $\phi_{\text{in}}(t)$ is the running-wave probability amplitude of the electric field of the photon and normalized according to Equation 4.7. We heuristically added the single-photon detuning[2] Δ_0 and the cavity losses κ_{loss} to the original Equation (5) in [136]. From Equation 6.1 the analytical expression for the Rabi frequency

$$\Omega_{\text{D}}(t) = 2\,\frac{i\,\dot{c}_e(t) + (\Delta_0 + i\,\gamma)\,c_e(t) - g_0\,c_{g_2}(t)}{c_{g_1}(t)} \tag{6.2}$$

with

$$c_{g_2}(t) = \frac{\phi_{\text{in}}(t)}{\sqrt{2\kappa}}$$

$$c_e(t) = i\,\frac{\dot{\phi}_{\text{in}}(t) - (\kappa + \kappa_{\text{loss}})\,\phi_{\text{in}}(t)}{g_0^*\,\sqrt{2\kappa}}$$

$$\rho_{g_1 g_1}(t) = \rho_0 - \rho_{g_2 g_2}(t) - \rho_{ee}(t) + \int_0^t \left[\left| \phi_{\text{in}}(t') \right|^2 - 2\gamma\,\rho_{ee}(t') \right] dt'$$

is obtained. Here, they introduce the population $\rho_{ii}(t) = c_i(t) c_i^*(t)$ of the state $i \in [g_1, g_2, e]$. They find $\rho_{g_1 g_1}(t)$ is given by the continuity balance and by taking population loss into account. On resonance, $c_{g_1}(t)$ is real and Equation 6.2 is solvable with $c_{g_1}(t) = \sqrt{\rho_{g_1 g_1}(t)}$. The main effect of introducing $\Delta_0 \neq 0$ is the expected increase in the required driving strength and the necessity of an average two-photon detuning $\bar{\delta} \neq 0$, which we will discuss later on.

In Equation 6.2, physically realistic, finite photons and thus Raman pulses within an interval $[0, T]$ are considered. The photons may start off smoothly with $\phi_{\text{in}}(0) = \dot{\phi}_{\text{in}}(0) = 0$ [189], but the second derivative might be non-zero. As a consequence, Equation 6.2 yields $\Omega_{\text{D}}(0) \cdot c_{g_1}(0) \neq 0$. From $\rho_{g_1 g_1}(t)$ it follows that this is only possible for an artificial initial population in $|g_1\rangle$ – otherwise the write pulse diverges. Another problem in this derivation of Ω is that any excited state decay reduces the total atomic population $\sum_i \rho_{ii}$, which is prevented in our simulation by including decay channels back to the ground states (cf. Eq. 4.6).

For a $T = 100$ ns long, sine squared-shaped input pulse $\phi_{\text{in}}(t)$ given by Equation 5.2 and $\Delta_0 = \kappa_{\text{loss}} = 0$,

---

[1] In Section 6.2 we will see that the value in our experiment is actually lower.
[2] In a Λ-configuration, the appropriate choice is given by $|\Delta_0| \gg \gamma C'$, adapted from [135].
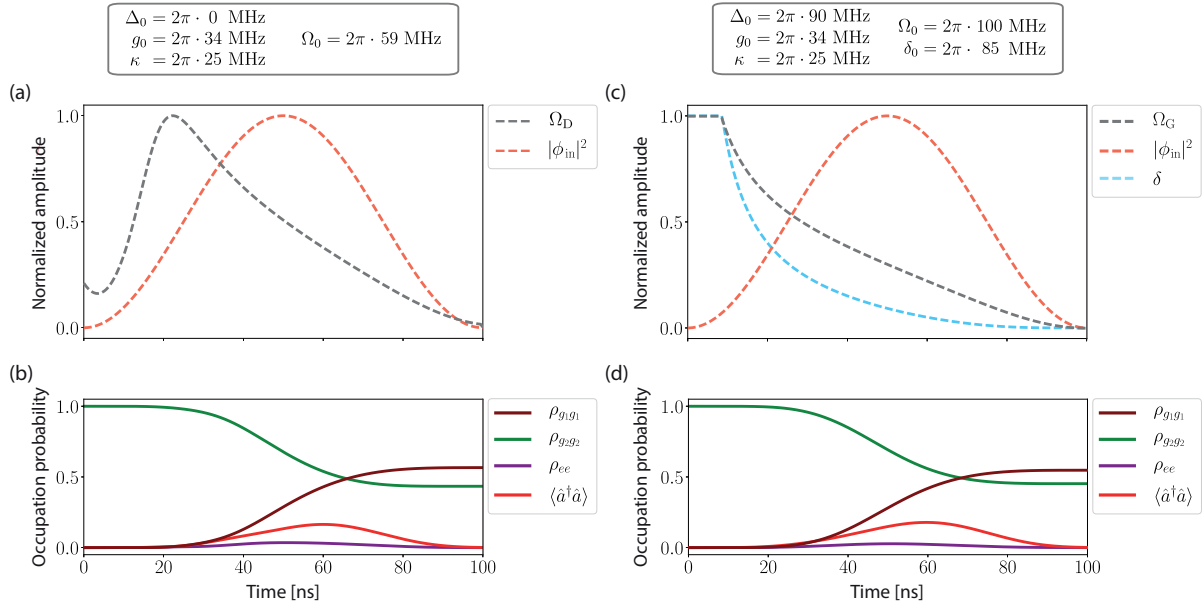
Figure 6.1: Comparison of pulse sequences for adiabatic storage of a $T = 100$ ns long, coherent pulse with a mean photon number $n_s = 1$ and a temporal envelope given by a sine squared as in Equation 5.2. The simulations are performed for a Λ-configuration, see Chapter 4. **(a)** The approach of Dilley *et al.* is based on impedance matching. The typical counter-intuitive order, in which the write pulse Ω_D (gray) arrives before the incoming photon ϕ_{in} (orange), is obtained from Equation 6.2. The pulses are normalized and the system parameters are displayed above. **(b)** The plot showing the occupation probabilities of the internal atomic states ρ_{ii} (brown, green, purple) and the cavity mode $\langle \hat{a}^\dagger \hat{a} \rangle$ (red) reveals a negligible excited state population and a storage efficiency of $\eta_{storage} = 57$ % for a coherent input pulse with a mean photon number of $n_s = 1$. This efficiency also corresponds to $\rho_{g_1 g_1}(t = 100$ ns$)$. Furthermore, 57 % is the maximum possible state transfer for our cooperativity. **(c)** Gorshkov *et al.* derive Ω_G by adiabatic elimination of the excited state. The analytic solution includes a single-photon detuning $\Delta_0 \neq 0$, which requires a time-dependent adjustment of the two-photon detuning δ (blue). The storage efficiency of 55 % is not reduced by truncating both amplitudes. **(d)** Similar dynamics as in (b) are obtained.

we obtain $\Omega_D(t)$ as displayed in Figure 6.1(a). For our system parameters, the initial, false state population of $\rho_0 = 0.5$ % is chosen too small, leading to $\Omega_D(0) \neq 0$. However, as seen in the simulated dynamics of the atomic states below (Fig. 6.1(b)), the storage takes place during the falling slope of the write pulse. The actual value of the Rabi frequency at $t \approx 0$ is less critical, as long as it is rising to Ω_0 while the pulse enters[3]. In STIRAP theory, there is a three-stage description of a process driven by pulses of finite support [191]. Here, the prior and post interval do not play an important role compared to the interaction interval, in which the light and Raman pulse overlap the most.

The simulation reveals another aspect: As desired, the excited state population ρ_{ee} is negligible. The storage efficiency for a coherent pulse with a mean photon number $n_s = 1$ is $\eta_{storage} = 57$ %, which constitutes the optimum for our cavity parameters. The probability $P(n)$ to find n photons in a coherent pulse is

$$P(n) = e^{-n_s} \frac{n_s^n}{n!} . \tag{6.3}$$

Thus the probability of having one or more photons is calculated to be $\sum_{n=1}^{\infty} P(n) = 1 - P(0) = 63$ %.

---

[3] In experiments, the control field is mostly ramped adiabatically down and up for storage and retrieval, respectively [23, 190].

This has to be multiplied by $\eta'_{\max} = 90\,\%$ as given by Equation 4.10, which finally results in 57 %. In fact, in the single-photon limit $n_s \to 0$ (see Sec. 4.1), the simulation fully agrees with the efficiency of 95 % reported in [136].

A drawback of impedance matching is, that major losses due to excited state population are accepted, which negatively affects the transfer fidelity between the two ground states. To avoid this problem, Gorshkov *et al.* find the optimum pulse by adiabatic elimination of the excited state $|e\rangle$. In [135], they obtain the expression

$$\Omega_G(t) = -\frac{\gamma\,(1+C) - i\Delta_0}{\sqrt{2\gamma\,(1+C)}} \cdot \frac{\phi_{\rm in}(t)}{\sqrt{\int_0^t |\phi_{\rm in}(t')|^2\,dt'}} \cdot e^{i\Delta_0 \cdot h(t,T)/[\gamma^2(1+C)^2 + \Delta_0^2]}$$

$$h(t,T) = \int_t^T \left|\Omega_G(t'')\right|^2 dt'' \,.$$

We insert $h(t,T)$ into the expression for $\Omega_G(t)$ and take both the natural logarithm and time derivative to obtain the complex differential equation

$$\dot{\Omega}_G(t) = \left(\frac{\dot{\phi}_{\rm in}(t)}{\phi_{\rm in}(t)} - \frac{\phi_{\rm in}(t)^2}{2\int_0^t |\phi_{\rm in}(t')|^2\,dt'}\right) \cdot \Omega_G(t) - i\frac{\Delta_0}{\gamma^2\,(1+C)^2 + \Delta_0^2} \cdot \Omega_G(t)^2 \tag{6.4}$$

$$= \Phi_{\rm in}(t) \cdot \Omega_G(t) - i\alpha \cdot \Omega_G(t)^2 \,.$$

In order to solve Equation 6.4 we choose to re-write $\Omega_G(t)$ in terms of real ($\Omega_{G,{\rm Re}}(t)$) and imaginary part ($\Omega_{G,{\rm Im}}(t)$), which leads to a set of two coupled differential equations:

$$\dot{\Omega}_{G,{\rm Re}}(t) = \Phi_{\rm in}(t)\,\Omega_{G,{\rm Re}}(t) + 2\,\alpha\,\Omega_{G,{\rm Re}}(t)\,\Omega_{G,{\rm Im}}(t)$$

$$\dot{\Omega}_{G,{\rm Im}}(t) = \Phi_{\rm in}(t)\,\Omega_{G,{\rm Im}}(t) - \alpha\left(\Omega_{G,{\rm Re}}(t)^2 - \Omega_{G,{\rm Im}}(t)^2\right) \,, \tag{6.5}$$

with

$$\alpha = \frac{\Delta_0}{\gamma^2\,(1+C)^2 + \Delta_0^2} \,.$$

We find the solution to Equation 6.5 numerically, while a congruent analytic expression [137] is given by:

$$\Omega_G(t) = \frac{\gamma\,(1+C) + i\Delta_0}{\sqrt{2\gamma\,(1+C)}} \cdot \frac{\phi_{\rm in}(t)}{\sqrt{\int_0^t |\phi_{\rm in}(t')|^2\,dt'}} \cdot e^{-i\Delta_0/[2\gamma(1+C)]\cdot\ln\int_0^t |\phi_{\rm in}(t')|^2 dt'} \,. \tag{6.6}$$

Equation 6.6 does not only tell us the amplitude $|\Omega_G(t)|$ of the write pulse, but also its time-dependent two-photon detuning[4] $\delta(t) = \frac{d}{dt}\arg\left(\Omega_G(t)\right)$: In the presence of a large single-photon detuning and significantly different Rabi frequencies of Raman and light pulse, the optimum condition for population transfer is no longer given by a two-photon detuning of zero [165]. Some state transfer concepts, such as *Stark-Chirped Rapid Adiabatic Passage* (SCRAP)[192] and *Stark-Induced Adiabatic Raman Passage* (SARP) [193] even rely on this effect and try to induce a.c. Stark shifts on purpose.

Figure 6.1(c) shows the pulse shape Ω_G obtained for the previous parameters, but with a single-photon detuning of $\Delta_0 = 2\pi \cdot 90$ MHz, such that $\Delta_0 > \kappa_{\rm total}$. Towards $t = 0$, the pulse diverges, but the infinite part can be truncated without affecting the transfer.[5] We arbitrarily limit Ω_G to a peak Rabi frequency

---

[4] Note that the phase has to be unwrapped before taking the time derivative.

[5] So the exact value of Ω_G *and* Ω_D are uncritical around $t \approx 0$.
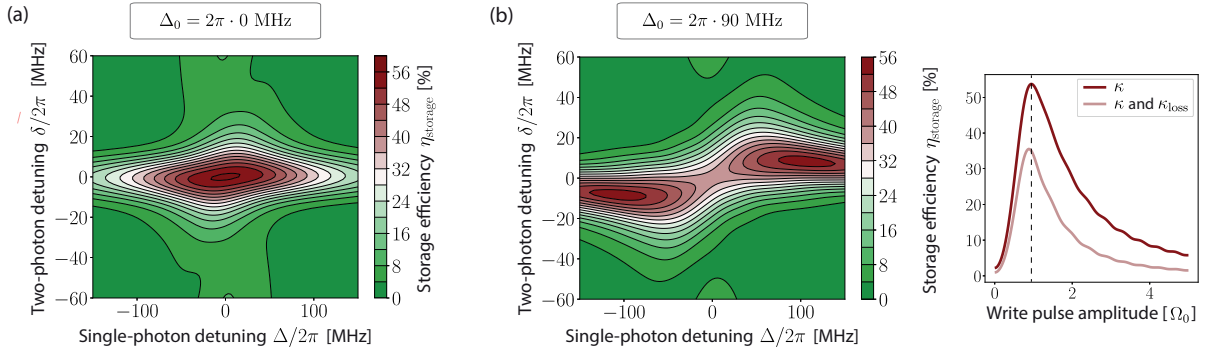
Figure 6.2: We heuristically implemented a single-photon detuning Δ_0 in Equation 6.1. Here, we calculate Ω_D for fixed values $\Delta_0 = 0$ **(a)** and $\Delta_0 = 2\pi \cdot 90$ MHz **(b)**. As a consequence, the peak value increases to $\Omega_0 = 2\pi \cdot 106$ MHz. Using this pulse design, we simulate the storage efficiency in dependence of variable detunings Δ and δ (see Eq. 4.1). We observe that in the second case an average two-photon detuning of $\overline{\delta} = 2\pi \cdot 9$ MHz is required. At the same time, the maximum transfer is 53 %. When taking the cavity losses κ_{loss} into account as well, the transfer is reduced by the factor $\eta'_{\text{max}}/\eta_{\text{max}}$ to 36 %, see Equations 4.9, 4.10 in Section 4.1. This is shown in a separate plot in (b), where η_{storage} is plotted against the write pulse amplitude. A vertical line indicates the maximum storage efficiency.

$\Omega_0 = 2\pi \cdot 100$ MHz with a maximum two-photon detuning $\delta_0 = 2\pi \cdot 85$ MHz. The time-varying $\delta(t)$ is implemented by giving the static Hamiltonian in Equation 4.1 an explicit time-dependence. The resultant dynamics of the three-level atom are very similar to the previous case; a storage efficiency of 55 % is reached (Fig. 6.1(d)).

As a last remark, in Equation 6.6 cavity losses are included by substituting C with C' [137].

In summary, we have reviewed two analytical methods to obtain the optimum storage pulse in the adiabatic regime. The approach based on excited-state elimination treats the case of non-zero single-photon detuning and suggests both time-varying amplitude $\Omega_G(t)$ and two-photon detuning $\delta(t)$. We already mentioned in Section 2.5 that the hereto equivalent phase modulation of the Raman pulse could be realized by exploiting the residual frequency chirp of a pulse modulator. In fact, the similar shape of $\delta(t)$ and the intensity profile $|\Omega|^2$ is likely to make a positive contribution. But in our experiment, we can only control the laser intensity. Therefore we use our simulation and numerically search for an optimum, *static* $\overline{\delta}$, which can be implemented through the OPLL between pulse and Raman laser. As of now, we choose to follow the impedance-matching approach of Dilley *et al.*, since it gives equal results for $\Delta \to 0$ and does not require truncating the amplitude. We design $\Omega_D(t)$ for $\Delta_0 = 2\pi \cdot (0, 90)$ MHz and calculate the storage efficiency in dependence of Δ, δ for both cases. The result for $\Delta_0 = 0$ is shown in Figure 6.2(a). As expected, at $\Delta = \Delta_0$ we obtain the previous efficiency. Figure 6.2(b) for $\Delta_0 = 2\pi \cdot 90$ MHz shows that the transfer success will not fall below 53 %, if the average δ is set to $\overline{\delta} = 2\pi \cdot 9$ MHz – which means that the loss in efficiency here compared to the one using a sophisticated sweep $\delta(t)$ is only 2 %.

An estimate for the expected value of $\overline{\delta}$ can also be obtained by the differential light shift δ_{diff} [126] caused by the pulses. Comparing Equation 6.1 to the classical description of the three-level STIRAP process [194], we find that the *pump* Rabi frequency is given by $2g_0$, which allows us to express δ_{diff} as:

$$\delta_{\text{diff}} = \frac{\Omega^2 - (2\,g_0)^2}{4\,\Delta_0}$$

In our case, the time-varying Rabi frequencies lead to light shifts within $2\pi \cdot [-13, 31]$ MHz, in agreement with the average value we found simulating the system. Another method [195] allows to estimate the center of the two-photon detuning interval directly:

$$\delta_{\mathrm{c}} \approx \frac{\Omega_{\mathrm{rms}}^2 \cos(\pi \alpha')}{8 \, \Delta_0} \left(1 - \frac{\Omega_{\mathrm{rms}}^2}{8 \, \Delta_0^2} \right), \tag{6.7}$$

with

$$\alpha' = \frac{2}{\pi} \cos^{-1} \left(\frac{\overline{\Omega_0}}{\Omega_{\mathrm{rms}}} \right).$$

Here, Ω_{rms} is the rms value of both Rabi frequencies and $\overline{\Omega_0}$ the average Rabi frequency of the write pulse. From Equation. 6.7 we get $\delta_{\mathrm{c}} \approx 2\pi \cdot 7.2$ MHz.

Cavity losses have a detrimental effect: Part of the photon is no longer coherently mapped into the atom, but lost due to scattering and absorption on the mirror coating. Figure 6.2(b) illustrates the storage efficiency with and without losses as a function of the write pulse amplitude. In the presence of κ_{loss}, the transfer is reduced by the factor $\eta'_{\mathrm{max}} / \eta_{\mathrm{max}}$ to 36 %, see Equations 4.9 and 4.10 in Section 4.1.

6.1.2 Storage Efficiency in and beyond the Adiabatic Regime

The cavity losses are accurately determined by recording the empty cavity spectrum, while the single-photon detuning is indirectly measurable by characterizing the a.c. Stark shifts via the trap frequency (see Sec. 3.2.2). The atom-cavity coupling strength g_0 is measured in VRS sweeps. Consequently, we treat these quantities as being well-known and derive a strategy for obtaining the maximum storage efficiency in the multidimensional parameter space given by the residual contributing factors: The write pulse delay τ_Ω, the two-photon detuning $\overline{\delta}$ and the photons per input pulse n_s. To demonstrate that those parameters cannot be regarded independently, opposing to what is sometimes done [196], we simulate the transfer probability as the write pulse amplitude and one of those parameters are varied, while all others are kept at constant values, which grant maximum storage efficiency.

In the adiabatic regime, we use $\Omega_{\mathrm{D}}(t)$ and vary the delay between write and input pulse. Figure 6.3(a) confirms our previous observation that the key aspect of the pulse shape is the falling slope. If the control laser is switched on too early, the loss in transfer can be compensated to a certain extent by increasing the amplitude of the pulse. As a side remark, the special case of simultaneously terminating pulses is pursued in *fractional STIRAP* protocols, e.g. to create coherent superpositions [197].

The parameters $\overline{\delta}$ and $\Omega_{\mathrm{D}}(t)$ are connected similarly: The pulse causes a light shift, which needs to be compensated (Fig. 6.3(b)). The region of high efficiency is sharply defined and given by the spectral properties of the input pulse – the longer T, the sharper the two-photon resonance.

In our single-sided system, experimental techniques to calibrate the photon number per pulse n_s are non-applicable, since the cavity transmission is not accessible [198, 199]. Monitoring the reflection of near-adiabatic pulses, we cannot distinguish between light which was directly reflected on the HT mirror and light that leaks out of the resonator. Therefore, we have to determine n_s by observing the saturation of the *transfer efficiency* η_{transfer} for many input photons. As a reminder, the *storage efficiency* we are really interested in, still has to be normalized by the number of photons retrospectively (see Eq. 4.8), so when dealing with $n_s \neq 1$, the two terms have to be distinguished. During a storage attempt of a pulse containing more than one photon on average, the probability of not having a photon is reduced (see Eq. 6.3) and cavity losses are overcome. Also decay from the excited state can lead back to the initial state, from where the atom can interact with the pulse again, increasing the chance of transfer.
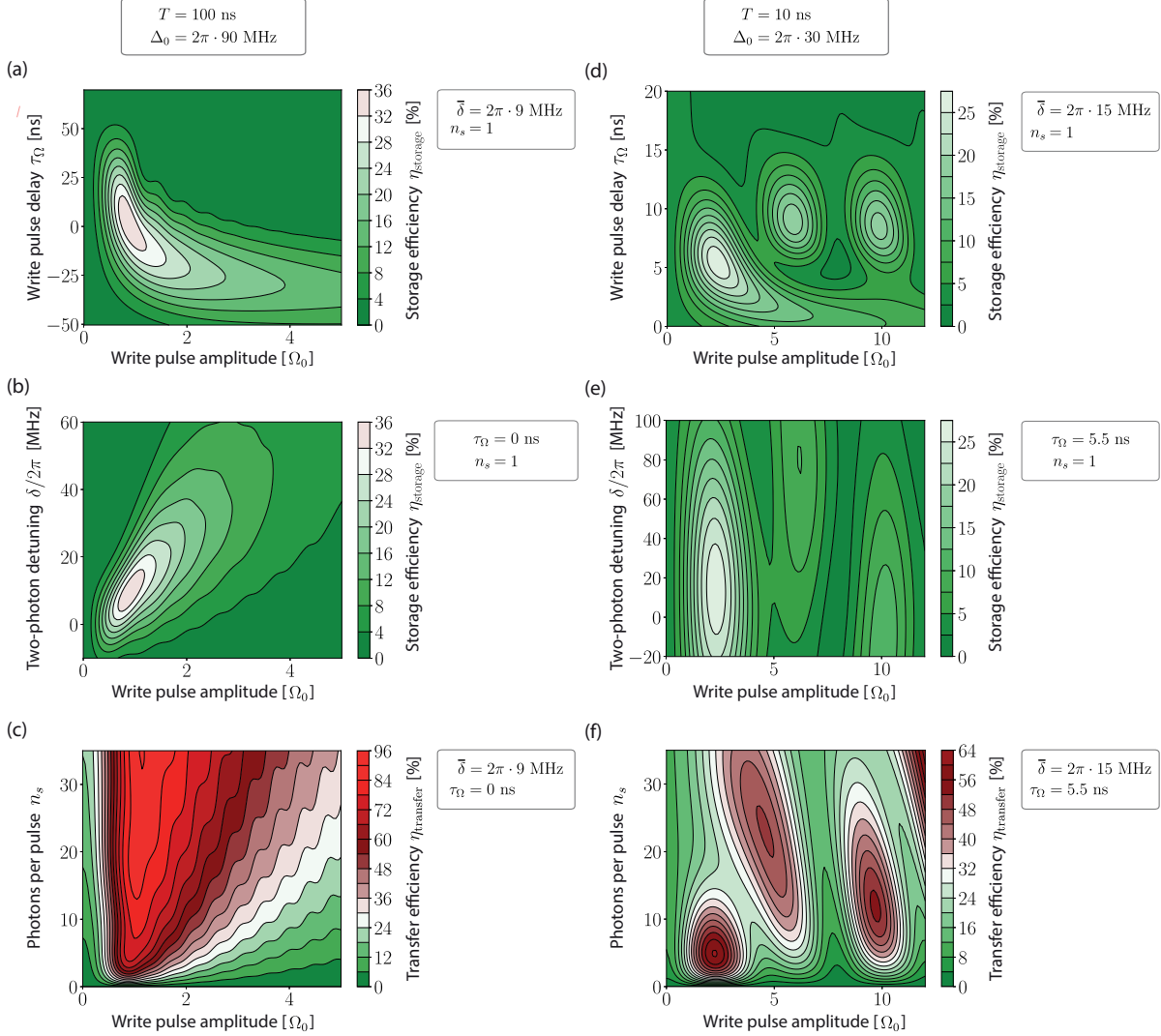
Figure 6.3: The storage and, for $n_s \neq 1$, transfer efficiency as a function of the write pulse amplitude and **(a)** the write pulse delay τ_Ω, **(b)** the two-photon detuning $\bar{\delta}$ and **(c)** the photons per input pulse n_s. The amplitude is given in multiples of the peak value Ω_0 of Ω_D in 6.1(a). All of these simulations are performed in the adiabatic limit with $T = 100$ ns. **(d)**,**(e)** and **(f)** show the dependency for short pulses with $T = 10$ ns. In particular, we temporally compress Ω_D calculated for $\Delta_0 = 0$. The maximum efficiency in each $T = 10$ ns 2-D map can now be *experimentally* found by two independent, one-dimensional scans, e.g. of n_s and write pulse amplitude, which makes it possible to calibrate the average photon number per input pulse. A detailed description is found in the main text.

In any case, if the write pulse is absent (i.e. $\Omega_D(t) = 0$), the incoherent transfer will be much smaller than the coherent one, for any mean photon number we simulate. A more detailed discussion is found in Section 6.1.4. Furthermore, Figure 6.3(c) shows that n_s can only be obtained, if $\Omega_D(t)$ is perfectly known.

So far, we have seen that the knowledge of all control-pulse and system parameters is crucial for achieving high storage efficiencies. Unfortunately, some of them are not easily found experimentally, since a two-dimensional map of the transfer efficiency has to be measured, e.g. to confirm the number of input photons. We will see in the following that the fast storage regime, e.g. with pulses of $T = 10$ ns duration, provides a solution. Although $\Omega(t)$ can no longer be obtained from Equation 6.2, any short pulse of that length can be entered in the simulation to investigate the effect of the pulse parameters. As a first idea, we choose to simply compress $\Omega_D(t)$ as calculated for $\Delta_0 = \kappa_{loss} = 0$, having in mind that $TC'\gamma$ is still greater than one. The resulting pulse with shape $\Omega_{D,c}(t)$ is used to repeat all dependency-investigating simulations.

In Figure 6.3(d) we see that both an adiabatic and a π-pulse component contribute to the storage efficiency. The latter uses the energy exchange between cavity field and atom in order to map the excited state population from $|e\rangle$ to the target state $|g_1\rangle$ [135]. For increasing write pulse amplitudes, we observe revivals which we attribute to Rabi oscillations. Besides, the counter-intuitive pulse order as common for STIRAP processes is no longer the most efficient sequence. Instead, the intuitive order, in which the light pulse is followed by the Raman pulse leads to the highest storage efficiency. This pattern is also realized in the adiabatic regime by the *B-STIRAP* mechanism, in which population transfer relies on adiabatic following of a bright state [200].

The short pulse is not only less sensitive to $\bar\delta$, but it also leads to the possibility of finding the optimum storage efficiency experimentally by first scanning the write pulse amplitude and second the two-photon detuning (Fig. 6.3(e)). Thus, only two one-dimensional scans are required instead of the full 2-D map in case of $T = 100$ ns. We see in Figure 6.3(f) that the same kind of decoupling takes place for the mean photon number per input pulse, which will allow us to find $n_s = 1$.

In summary, the simulation provides a robust strategy to determine the optimum storage efficiency for non-adiabatic pulses experimentally. We have to define as many parameters as possible in advance. In order to set the delay between the two pulses, we calibrate the optical path length: The Raman pulse entering perpendicular to the cavity axis is shone onto the fiber tip directly. Part of the light is scattered into the cavity fiber and the time between pulse trigger and arrival at the SPCMs is measured. Likewise, the coherent pulse to be stored is sent to the off-resonant cavity, which results in total reflection at the input mirror, from where it shares the path of the scattered Raman light. We can determine the delay between both events with a precision of less than half a nanosecond. The two-photon detuning $\delta = 0$ corresponds to the carrier transition in our Raman spectra (see Fig. 3.5). The remaining unclear parameters are thus the write pulse amplitude and n_s, which we can find by two independent one-dimensional scans. Thereby, the initial guess for n_s is given by reflecting the input pulse on the HT mirror and considering the path and detection efficiency discussed in Section 5.2.4. The start point for sweeping the Raman driving strength is based on measuring the CW peak transmission of the EOM. Its power is measured before the optical entrance port of the vacuum chamber, and the beam area is estimated from an EMCCD camera image (cf. Fig. 2.1), which then allows to estimate the Rabi frequency.

6.1.3 Enhancing the Efficiency of Fast Storage by Optimal Control

The simple compression of a write pulse calculated for a different temporal regime might not deliver the highest storage efficiency for short input pulses. Therefore, as a second method, we use an optimal control
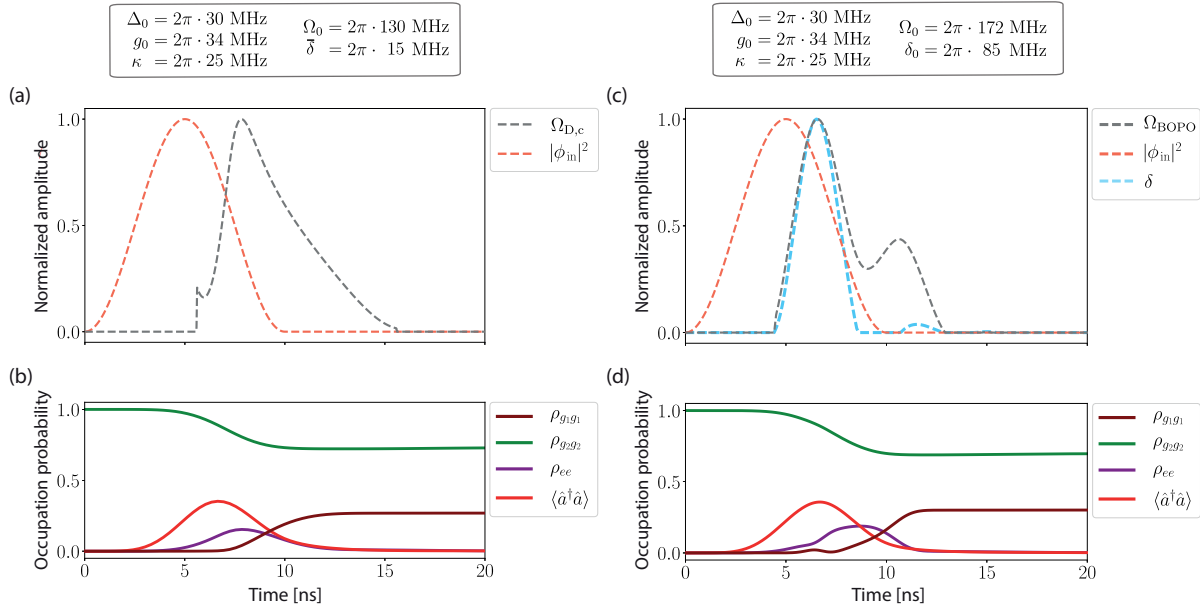
Figure 6.4: Comparison of pulse sequences in the fast storage regime, where a $T = 10$ ns long, coherent pulse with a mean photon number $n_s = 1$ and a temporal envelope given by a sine squared as in Equation 5.2 is mapped into the atomic ground states. **(a)** The first approach is based on temporal compression. As the storage process becomes non-adiabatic, the pulse order changes and $\Omega_{\mathrm{D,c}}$ (gray) follows ϕ_{in} (orange). **(b)** The plot showing the occupation probabilities of the internal atomic states ρ_{ii} (brown, green, purple) and the cavity mode $\langle \hat{a}^\dagger \hat{a} \rangle$ (red) reveals a significant excited state population, which is coherently mapped to $\rho_{g_1 g_1}$. A storage efficiency of $\eta_{\mathrm{storage}} = 27\%$ is achieved (cf. Fig. 6.3(d,e)). **(c)** As a second approach, we employ optimal control techniques and BOPO (see Sec. 4.3) to maximize the state transfer. Only when taking a time-dependent two-photon detuning (blue) into account, we increase the efficiency to 30%. **(d)** The dynamics are similar, but the excited state build-up is slightly favored.

(OC) approach to maximize the state transfer [201]. The idea is also found in a previous experiment, where an optimization relying on successive time-reversal iterations to shape the *input* pulse for storage in an EIT medium [202] was demonstrated [158]. Obviously, this approach does not help providing a memory for arbitrarily shaped input pulses, e.g. with the natural decay envelope of the quantum dot emission. Using our BOPO method (see Sec. 4.3) and Equation 4.11, we thus search for the best temporal shape of the Raman Rabi frequency $\Omega_{\mathrm{BOPO}}(t)$ to store a pulse of the previous shape.

We find that in the adiabatic limit, the control pulse shape alternates between $\Omega_{\mathrm{D}}(t)$ and $\Omega_{\mathrm{G}}(t)$ during the optimization process, which confirms that the STIRAP scheme delivers the optimal pulse sequence [203]. In the fast storage regime, the OC pulse amplitude does not provide a significant improvement with respect to the pulse compression shown in Figure 6.4(a,b). But in combination with an optimized, time-dependent $\delta(t)$, the storage efficiency increases from 27 to 30%, as displayed in Figure 6.4(c,d). We have to keep in mind, that this difference in efficiency becomes more pronounced when regarding the single-photon limit $n_s \to 0$.

To our knowledge, such an investigation of the storage efficiency beyond the adiabatic limit and in the presence of a single-photon detuning has not been pursued yet. For $\Delta_0 = 0$, concurrent efforts to exploit optimal control lead to impractical pulse shapes. As discussed in Section 4.3, initial parts of the pulse found in [137] can most likely be truncated. Although they are probably the best numerical solution, the discussion of the underlying physics is questionable. The divergent pulse is seen as a means
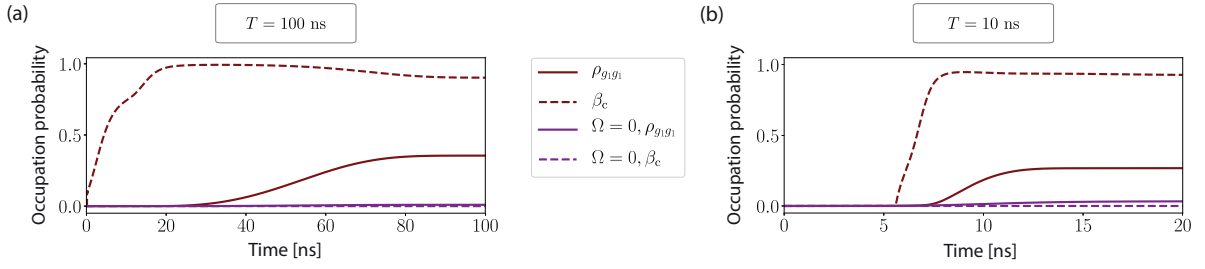
(a)

(b)

Figure 6.5: Whether the storage is a coherent process or not can be quantified by the coherent storage component β_{c} (dashed line) given in Equation 6.8. In the presence (brown) or absence (purple) of the Raman write pulse, the evolution of β_{c} and the ground state population $\rho_{g_1 g_1}$ (solid line) during the storage process is shown. **(a)** In the adiabatic limit, the storage efficiency is 36 % vs. 1%, while $\beta_{\mathrm{c}} = 90$ %. **(b)** For short pulses, the transfer is 27 % vs. 3%, while β_{c} increases to 93 %. In both cases, losses through the excited state are kept small, resulting in coherent storage.

of impedance matching to maximize the transmission at the HT mirror, but it is almost fully switched off when the photon arrives. A similar numerical artifact was present in Figure 6.4(c) at $t = 2$ ns, but its suppression reduced the efficiency by insignificant 0.08 %[6].

Especially for $\Omega_{\mathrm{D,c}}(t)$, the dynamics in Figure 6.4(b) resemble a mixture of an adiabatic transfer between $\rho_{g_2 g_2}$ using the cavity population and a coherent mapping of ρ_{ee} to $\rho_{g_1 g_1}$ similar to a π-pulse. In Figure 6.4(d), the excited state build-up is slightly favored. It would be interesting to investigate, how the storage efficiency for the analytical solutions by Gorshkov *et al.*, which propose a π-pulse only, differs from the one obtained in our work. However, since we cannot control $\delta(t)$ and since we are interested in showing the efficiency as a function of the aforementioned parameters, we stick to the solution given by compressed pulses $\Omega_{\mathrm{D,c}}$.

6.1.4 Estimating the Coherent Storage Component

In the context of (atomic ensemble) quantum memories, a crucial requirement is the coherent state transfer between the incident field state and the atomic ground state superposition. An experimental approach to verify its success relies on exploiting the defined phase of the incoming pulse. By sending a second input pulse of variable phase during the Raman read pulse, interference fringes are observed in the retrieval efficiency [190]. For technical reasons, the method is not yet accessible in this work, so we derive the expected coherent storage component

$$\beta_{\mathrm{c}} = \frac{\rho_{g_2 g_1}}{\sqrt{\rho_{g_1 g_1} \cdot \rho_{g_2 g_2}}} \tag{6.8}$$

from our simulation. For both discussed scenarios, the target state population $\rho_{g_1 g_1}$ and β_{c} are shown in Figure 6.5. In the presence of the control field $\Omega(t) = \Omega_{\mathrm{D}}(t)$, an input pulse of $T = 100$ ns duration is mapped with an optimized efficiency of 36 % and $\beta_{\mathrm{c}} = 90$ %. Without the write pulse, part of the population is still transferred incoherently with $\eta_{\mathrm{storage}} = 1$ %. In the fast storage regime, the transfer is 27 % vs. 3%, while β_{c} increases to 93 %. In the adiabatic limit, a high degree of coherent storage is expected for our system, in which the cavity damping of $\kappa_{\mathrm{total}} \gg \gamma$ and the strong atom-cavity coupling $g \gg \gamma$ keep the excited state population small at any point in time. In the fast storage regime, the excited

---

[6] Not to mention that experiments are not even able to resolve this difference.

state population is built up, but transferred to the ground state in a time window much shorter than the excited state lifetime. Thus in both cases, the losses through the excited state are kept small.

6.2 Fast Storage of Pulses in a Tripod Configuration

In the previous sections, we have developed a strategy to achieve the optimum storage of short light pulses in a Λ-configuration. For our experiment the theoretical description is very similar but a few alterations have to be considered. First, the level structure represents a tripod, in which the chosen initial state $|2, -2\rangle$ is coupled to two cavity modes as discussed in Sections 4.2 and 5.1. As depicted in Figure 6.6(a), part of the population is transferred to $|2, 0\rangle$ by the coherent interaction of the two cavity modes g and g'. As a consequence of this configuration, the optimum transfer to $|1, -1\rangle$ is found for $\Delta_0 = \bar{\delta} = 0$. Second, the value of κ in the previous simulations considers only a single input-output port and is chosen to exceed the cavity losses – in reality, for our resonator the opposite scenario is the case. The value of $\kappa = 2\pi \cdot 16$ MHz for the HT mirror has been determined in Section 5.2.4. As the impedance matching between incoming photon and cavity depends on this κ, we expect an overall loss in storage efficiency for the previously discussed, non-adiabatic pulse length of $T = 10$ ns (since $T C' \gamma \approx 1$). Moreover, with $\kappa_{\text{loss}} = 2\pi \cdot 25$ MHz a significant amount of the photons is lost.

The coherent input light pulse shares its optical path with the probe light, as shown in Figure 6.6(b). Here, a 97:3 beam splitter ensures that generated photons are detected efficiently. The control laser for storage and generation is sent along DT_x as write and read pulses, respectively. The overall sequence in Figure 6.6(c) is very similar to the one for photon generation (cf. Fig. 5.1(c)), though here state preparation is performed by sending D_1 light along the cavity (see Sec. 3.3). Each photon storage attempt consists of cooling, state preparation and synchronized Raman write and input pulses ($\Omega_{\text{D,c}}$ and ϕ_{in}, respectively). After a storage time of 1 μs, which is simply chosen to exceed the pulse duration by two orders of magnitude, a Raman read pulse generates a photon as discussed in Chapter 5. In order to use this process to infer the storage efficiency, we read out the photon in the adiabatic regime, but on resonance as well. All steps considered, the repetition rate during the storage part of the sequence is up to 1.5 kHz. An exemplary, complete data trace for a single atom, recorded by the SPCMs, is shown in Figure 6.6(d) with 1 ms binning.

For an off-resonant cavity $\Delta_{\text{p-c}} \gg 0$, Figure 6.7(a) displays the normalized detection events for an input pulse $\left|\phi_{\text{in, exp}}\right|^2$ with on average $n_{s,\text{exp}} = 2.1$ photons being reflected off the HT mirror. For each data point, the error bars correspond to the Poissonian error. With the cavity on resonance, we perform three different experiments: The first consists of the full storage protocol, the second is without a write pulse and thus indicates the incoherent state transfer caused by optical pumping due to the input pulse and the third uses neither write nor input pulse, which constitutes a measure of false state preparation. From the ratio of the integrated detection counts, we obtain a coherent storage component of (79 ± 3) %, while our simulation predicted > 95 % according to Equation 6.8. Remarkably, the generated photon shape is now explicable by our simulation – for slightly different system parameters than assumed. The fit based on Equation 4.12 is successful for a reduced coupling strength of $g_{\text{fit}} = 0.7 \cdot g_0$. The origin of the now excellent agreement between theory and experiment is not yet entirely clear, but it could be connected to the single-photon detuning of $\Delta_0 = 0$, which forms a cleaner tripod system than in Chapter 5.[7] The level configuration with its two cavity modes is also the reason for the shorter output-pulse length of $T \approx 80$ ns, although we aimed for 100 ns (cf. Fig. 5.2(b)).

---

[7] Technical advancements over the past months could also contribute, e.g. improvements on the pulse suppression by positioning the EOM pulses at the very end of the AOM windows.
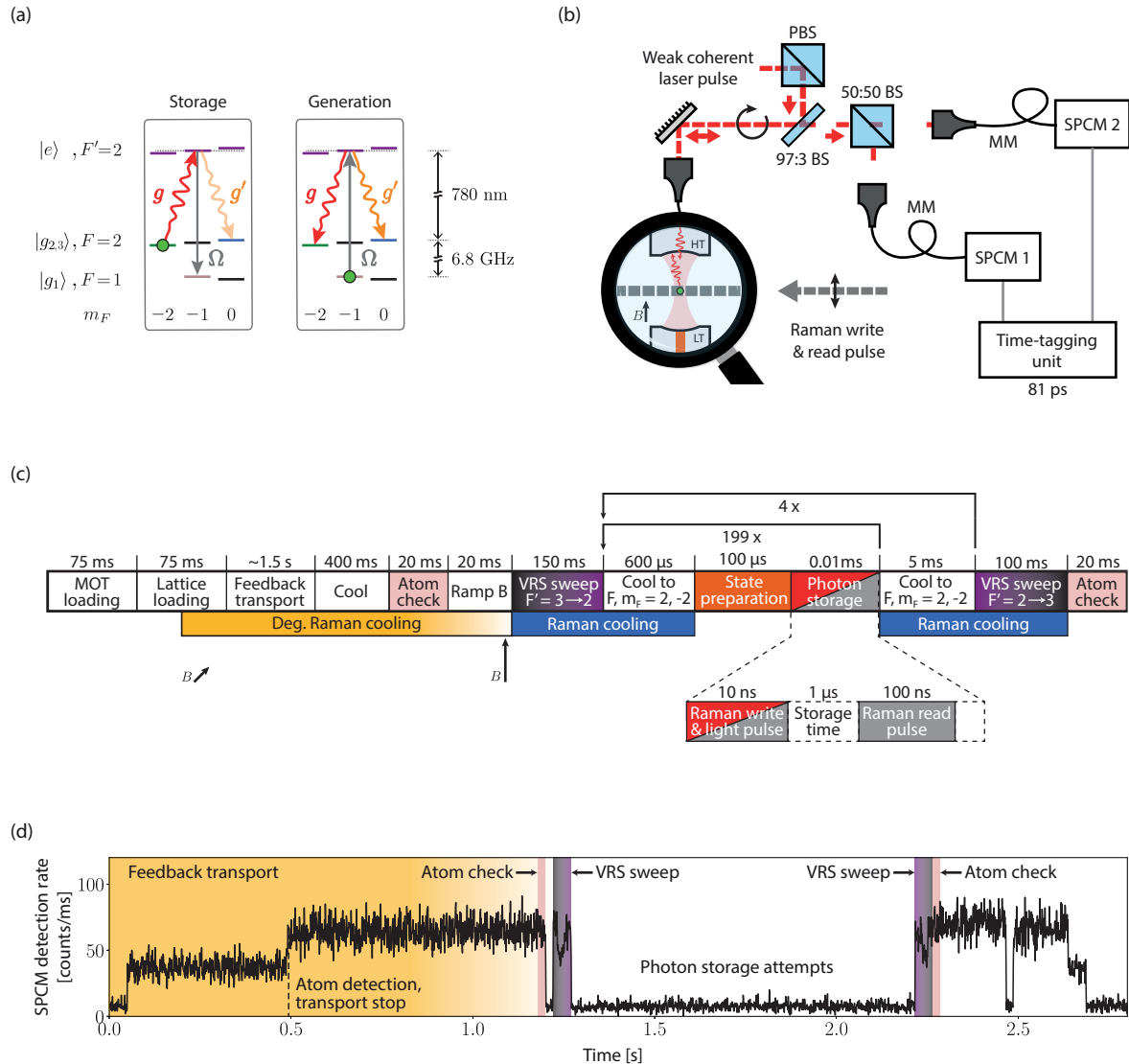
Figure 6.6: **(a)** Photon storage in a tripod configuration. An atom prepared in $|2, -2\rangle$ is not efficiently transferred to $|1, -1\rangle$ by the write pulse Ω (gray), since the coherent interaction with two polarization cavity modes g, g' (red and light orange) maps part of the population to $|2, 0\rangle$. Subsequent photon generation with a read pulse indicates successful storage. Our simulation predicts the highest storage efficiencies for $\Delta_0 = \bar{\delta} = 0$. **(b)** The weak coherent laser pulse shares its path with the probe light. A 97:3 beam splitter (BS) ensures low losses for generated photons. The initial Zeeman state is prepared using D_1 light (orange). **(c)** Flow diagram of the experimental sequence for photon storage. The loops sum up to 1000 storage attempts per 4 s sequence time. Within the actual pulsing window the rate is up to 1.5 kHz. **(d)** A typical measurement trace for the sequence in (c) (and Fig. 5.1(c)). The atom-cavity system is probed with a weak laser and the cavity reflection is recorded by both SPCMs. The summed photon detection events are binned with 1 ms. In the photon storage window, the bins mainly contain background counts (Raman-scattered lock laser light, SPCM dark counts). The presence of an atom (feedback transport, atom check) is indicated by a detected count rate of ~ 60 kcps. Note that during the VRS sweep, the probe light almost becomes resonant with the atom-cavity system (~ 30 kcps).
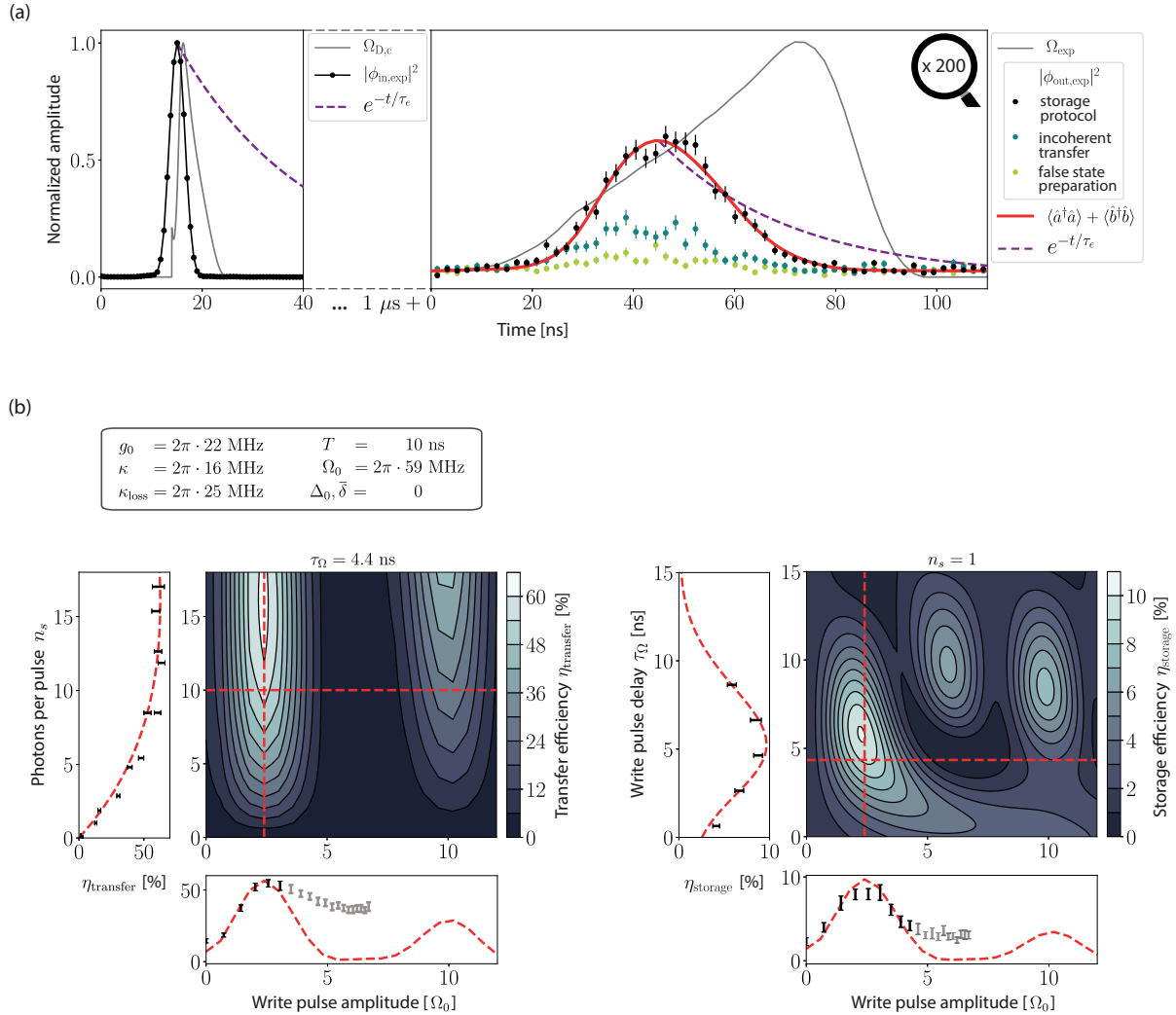
(a)

(b)

Figure 6.7: **(a)** The input pulse $\left|\phi_{\mathrm{in,\,exp}}\right|^2$ is reflected off the HT mirror (off-resonant cavity). Correlating the SPCM counts with the pulse trigger reveals the sine squared shape (Eq. 5.2) of $T = 10$ ns duration (black, solid line). For comparison, the atomic excited state decay with a time constant of $\tau_e = 26.2$ ns [58] is shown (purple, dashed line). In the photon storage experiment, the write pulse $\Omega_{\mathrm{D,c}}$ (gray, solid line) is applied with a delay of 4.4 ns to realize the intuitive pulse order required for optimal, non-adiabatic storage. After a storage time of $1\,\mu$s, a Raman read pulse Ω_{exp} (gray, solid line) generates a photon after the full storage protocol (black dots), from the incoherently transferred population in the absence of a write pulse (blue dots) and due to false initial state preparation (green dots), from which we infer a coherent storage component of (79 ± 3) %, details see main text. A successful fit based on Equation 4.12 (red, solid line) indicates an atom-cavity coupling strength of $g_{\mathrm{fit}} = 2\pi \cdot 22$ MHz. **(b)** Simultaneous fit of one photon-number, two write-pulse amplitude and one pulse-delay scan to the transfer efficiency simulation of our system, with the relevant parameters listed above. The error bars indicate the standard deviation of the mean value. From the fit, we extract the storage efficiency $\eta_{\mathrm{storage}} = (8.2 \pm 0.9)$ % for a coherent input pulse with an average photon number of $n_s = 1$. Points towards higher write pulse amplitudes (gray) have been excluded from the fit. A detailed description is found in the main text.

In order to determine the storage efficiency, we follow the approach found in Section 6.1.2 and simulate our system for its parameters $(g_{\text{fit}}, \kappa, \kappa_{\text{loss}}, \gamma) = 2\pi \cdot (22, 16, 25, 3)$ MHz and an atom in $|2, -2\rangle$. In both the simulation and the experiment, the intuitive pulse order is realized with a delay of 4.4 ns, which is the optimum delay for the originally measured atom-cavity coupling strength of $2\pi \cdot 34$ MHz. For the actual value of $2\pi \cdot 22$ MHz – and future storage attempts – $\tau_\Omega = 6$ ns is the best setting. Since our simulation only considers impedance matching and assumes perfect spatial mode-matching, in the following our calibration of the photons per pulse in the experiment compensates η_{mm} (see Sec. 5.2.4). The photon numbers are set by monitoring the off-resonant cavity reflection and counting the photons per pulse with the SPCMs.

In our experiment, we first scan the peak Rabi frequency $\Omega_{0,\text{exp}}$ of the write pulse, while a pulse containing on average $n_{s,\text{exp}} = 10$ photons is stored. The measurement is repeated for $n_{s,\text{exp}} = 1$. As can be seen from the simulation in Figure 6.7(b)[8], a clear peak in the transfer efficiency is identified. Thus, at the *measured* maximum, we vary the mean number of photons contained in the input pulse while keeping the amplitude of $\Omega_{\text{D,c}}$ fixed. Also, for $n_{s,\text{exp}} = 1$ and the same $\Omega_{\text{D,c}}$ we change the relative delay $\tau_{\Omega,\text{exp}}$ between input and write pulse. In all cases, transfer efficiencies given by

$$\eta_{\text{transfer, exp}} = \frac{\eta_{\text{retrieval}}}{\eta_{\text{state}} \cdot \eta_{\text{generation}} \cdot \left(\eta_{\text{HT}} \cdot \eta_{\text{mm}} \cdot \eta_{\text{path}} \cdot \eta_{\text{det}}\right)}$$

are measured (cf. Eq. 5.6). Here, $\eta_{\text{retrieval}}$ is the probability of detecting a photon after a triggered storage and generation loop, $\eta_{\text{state}} = (95.8 \pm 0.1)$ % is the state preparation efficiency discussed in Section 3.3 and the other factors are listed in Section 5.2.4 except for the on-resonance generation efficiency $\eta_{\text{generation}}$, which is assumed to reach its maximally possible value of

$$\frac{C'}{C' + 1} = \frac{g_{\text{fit}}^2}{g_{\text{fit}}^2 + \kappa_{\text{total}} \cdot \gamma} = (80 \pm 5) \ \% \ .$$

This assumption is legitimate for two reasons: First, the quantities entering the formula are obtained from our previous fit and the robust cavity bandwidth measurement. Second, we have increased the Raman power during the read-out to prevent residual population in $F = 1$. This can be seen in Figure 6.7(a), where the generated light-pulse duration is actually shorter than the read pulse.[9]

The recorded efficiencies of all four scans[10] are simultaneously fitted to our simulated maps using the model

$$\eta_{\text{transfer}} = \tilde{\eta} \cdot \eta_{\text{transfer, exp}} + \eta_0$$

and a method similar to those described in Section 4.3. A wrong estimation of the losses along the optical path and/or an error in the estimation of the photon generation efficiency is corrected by $\tilde{\eta}$, while the offset η_0 is indicating effects such as imperfect state preparation. At the same time, the estimated Rabi frequency of the Raman laser is corrected with $\tilde{\Omega}$[11] and the photon number with $\tilde{n}$, while a timing error is

---

[8] Note that the density matrix for a tripod system with 19 Fock states per cavity mode is extremely large. As a consequence, the resolution in Figure 6.7(b) is reduced in comparison to previous simulations.

[9] The F-state preparation efficiency (Sec. 3.3) could be used to determine $\eta_{\text{generation}}$ via the measurement with absent write and input pulses, but in our case it is afflicted with large errors.

[10] Note that they have been recorded in independent measurements over a time period of one week, which points at a high reproducibility of the presented measurements.

[11] Necessary because of false estimations of path losses and beam size, or due to a spread over m_F-levels.

taken into account with the offset τ_0:

$$\Omega_0 = \tilde{\Omega} \cdot \Omega_{0,\text{exp}}$$

$$n_s = \tilde{n} \cdot n_{s,\text{exp}}$$

$$\tau_\Omega = \tau_{\Omega,\text{exp}} + \tau_0 \,.$$

For the combined fit in Figure 6.7(b), we obtain $\tilde{\eta} = (0.8 \pm 0.1)$, $\eta_0 = (0.5 \pm 0.1)$ %, $\tilde{\Omega} = (0.7 \pm 0.1)$, $\tau_0 = (0.6 \pm 0.2)$ ns and most importantly $\tilde{n} = (1.1 \pm 0.1)$, which confirms that we are accurate in our estimation of the mean photon number per pulse. Peak Rabi frequencies above $3.4 \cdot \Omega_0$ ($n_s = 10$) and $4.5 \cdot \Omega_0$ ($n_s = 1$) are neglected in the fit. The significant deviation in efficiency might be explained by a two-photon Rabi frequency distribution due to different atom positions in the 3D dipole trap. Also, it could be related to an incoherent storage contribution that scales with the number of input photons, since the peak-to-deviation ratio in the two measurements changes. As a next step to resolve this issue, more data should be recorded to make use of our post-selection capability.

Nevertheless, for low photon numbers the deviation from the expected parameters is remarkably small. Hence, the storage efficiency for a spatially mode-matched coherent pulse with an average photon number $n_s = 1$ is found to be $\eta_{\text{storage}} = (8.2 \pm 0.9)$ %, while theoretically we expect 9.7 %. Post-selection on the atom-cavity coupling strength of well-confined atoms should lead to the observation of up to 12 % efficiency. If one is interested in the efficiency of storing a photon impinging on the HT mirror, the value has to be multiplied by $\eta_{\text{mm}} \approx 0.6$. The results can be compared to other atom-cavity systems, although one has to keep in mind that the losses and average coupling strength are not given in detail: In [23], the storage efficiency for a 2 μs long pulse is given as 17.5 % (up to 77 % expected[12]), while in [190], for an input duration $\gg 200$ ns a value of 5.7 % is found (up to 98 % expected[13]). In comparison, we do not only obtain efficiencies that almost reach the predicted value, but also store light pulses which are temporally shorter by more than a factor of 40, which is even shorter than the time constant of the atomic excited-state decay. We fully understand the origin of the measured efficiencies and are finally able to give the overall quantum memory efficiency of our system, which is

$$\eta_{\text{memory}} = \eta_{\text{storage}} \cdot \eta_{\text{mm}}^2 \cdot \eta_{\text{HT}} \cdot \eta_{\text{generation}} = (0.9 \pm 0.1) \ \% \,. \tag{6.9}$$

Here, we have to keep in mind that the input state has not yet been recreated, since both photon statistics and temporal envelope of the light pulse are altered.

In conclusion, we have coherently stored a weak, sine-square shaped pulse with on average one spatially mode-matched photon and less than $T = 10$ ns duration in our atom-cavity system. The efficiency of $\eta_{\text{storage}} = (8.2 \pm 0.9)$ % is close to the expected value for our high-bandwidth cavity and a tripod configuration. The storage process exhibits a coherent component of ~ 80 %, which is crucial for the phase-sensitive storage of photons in atomic ensembles. Our simulation describes the dependency on write pulse parameters accurately, which allows to adjust the pulse settings for optimal storage in the next experiments. In the near term, the main focus should lie on improving the confinement of atoms to increase the atom-cavity coupling strength. Furthermore, for a Λ-configuration, the expected storage efficiency increases by almost a factor of 2, which suggests to change the employed level scheme. In the long run, the implementation of low-loss resonators with higher bandwidths in combination with an increase of the light-matter interaction by placing atomic ensembles within the cavity mode will improve the storage efficiency significantly. This will also allow to demonstrate the storage of even shorter pulses. Consequently, real single photon sources, such as quantum dots, can provide the input field. Therefore,

---

[12] Assuming a loss-free, single-sided cavity and the given atom-cavity coupling strengths.
[13] Both mirrors are used for input-output coupling.

in the next chapter we make a step towards realizing hybrid experiments involving a quantum dot by showing how they can be referenced to atomic transitions.

Frequency–Stabilizing Quantum Dots to Atomic Transitions

S EMICONDUCTOR quantum dots (QDs) are promising building blocks for photonic quantum computing [204], quantum communication [205, 206] and applications in distributed quantum networks [207]. With recent efforts, not only are QDs able to emit high-quality single photons [208–210] and entangled photon pairs [156, 211–215], they also match optical transitions in neutral atoms [216–218]. These constitute important elements in envisioned quantum repeaters [29] and 'quantum hybrid systems' [180, 183].

Interfacing the two platforms requires a stable emission frequency of the QD, which is sensitive to several external perturbations, including temperature [219, 220] as well as electric [221–223], magnetic [212, 224] and strain fields [225–227]. While these phenomena lead to spectral wandering of the QD emission over long timescales, they also provide means to fine-tune and match the emission frequencies using active frequency feedback [33, 34, 228].

In our collaboration with the research group of Prof. Oliver G. Schmidt at the IFW Dresden, we simultaneously stabilize the emission frequency of two separate QDs via strain tuning of the host substrates [225, 229]. For this purpose, a rubidium-based Faraday filter serves as an absolute frequency standard for distant nodes and acts as a tunable frequency discriminator at atomic transitions of rubidium, a prominent quantum memory candidate [24]. The frequency-stabilized emitters thus become suitable single-photon sources for our fiber-based atom-cavity system which provides the high bandwidth needed to interact with short light pulses (as discussed in Ch. 1). Our efficient feedback scheme, for which only a weak photon flux is necessary, along with the introduction of a common and reproducible standard, paves the way towards quantum networks with distributed, indistinguishable solid-state emitters [1].

In this chapter, we briefly introduce quantum dots as single photon sources and characterize the spectral quality of their emission, before we look at their experimental implementation in more detail (Sec. 7.1). Then, the frequency discriminator (Sec. 7.2.1) and the rate-based feedback technique (Sec. 7.2.2) are explained. Subsequently, the feedback quality is analyzed (Sec. 7.2.3). As a benchmark, we show an improved long-term two-photon interference (TPI) visibility of the frequency-stabilized QDs in a Hong-Ou-Mandel experiment [219, 230–232] (Sec. 7.3). The presented results are adapted from [1] and constitute a significant step towards our goal to obtain deterministic and stable coupling of single photons to rubidium-based quantum memories.

7.1 A Brief Introduction to Quantum Dots

A quantum dot is a small solid-state structure which allows the three-dimensional confinement of charge carriers on the order of their de Broglie wavelength (typically several nm). The associated quantization of motion results in discrete energy levels, which is why QDs are sometimes referred to as 'artificial atoms'. These discrete states, along with the Pauli principle, make them ideal, on demand sources of pure single photons without multi-photon components. In order to trigger the emission, an electron is excited to a higher level and leaves a hole behind. This bound state is called an exciton. Depending on the lifetime of the excited state and optical selection rules, the pair recombines under the emission of a photon.

Other competitors, such as atom-cavity systems [20] or spontaneous parametric down-conversion sources [233] offer advantages in terms of coherence, but their emission rate and brightness cannot compete with those of QDs [45]. Another advantage is the integrability and scalability of solid-state technologies.[1]

The GaAs/AlGaAs QD samples in this work are grown by solid-source molecular beam epitaxy and *in situ* Al droplet etching, which leads to the formation of nano-holes with high symmetry. The holes are subsequently filled with GaAs and overgrown by AlGaAs, which results in a variety of isolated QDs (Fig. 7.1(b)), of which many emit close to the rubidium D_1 transitions [216]. Then, several QD-containing nanomembranes are obtained using wet chemical etching and are bonded to a piezoelectric actuator (0.3 mm PMN-PT) via a flip-chip transfer process [235]. Precise emission wavelength control is achieved by applying a voltage to the actuator.

The QD samples (QD1 & 2) are placed in two separate He cryostats[2] at 4 K to avoid thermal excitation of phonons. A Ti:sapphire laser with 3 ps pulse length and 76 MHz repetition rate is fed through a grating-based pulse-shaping setup for spectral narrowing. The light is then used to excite both QDs to the biexciton state (XX) with a resonant two-photon π-pulse [236], which ensures precise temporal control over the emission as it is required for TPI measurements. The fine-structure splitting S of the exciton state (X) leads to two cross-polarized XX decay channels, which are followed by the respective X decay, see Figure 7.1(c) [237]. For symmetric dots or, more general, symmetric electron wave functions in orthogonal directions, the fine-structure splitting vanishes. As a consequence, the which-path information is erased and entangled photon-pair emission is observed [216].

For the best control over the photon emission, we chose the XX photons and use strain tuning to make them compatible with the D_1 line of rubidium at 795 nm. Additionally, we select only one XX channel by polarization filtering. The respective emission spectra of both QDs are shown in Figure 7.1(d).

In order to calculate the expected Faraday filter transmission (Sec. 7.2.1) and photon indistinguishabilities (Sec. 7.3) the emission of both QDs is characterized. Fluorescence decay measurements reveal lifetimes of $T_1^{(QD1)} = (155 \pm 1)$ ps and $T_1^{(QD2)} = (187 \pm 1)$ ps. Using a Michelson interferometer, the coherence time T_2 and thus the Lorentzian linewidth θ of the emitted photons is determined [238, 239]. QD1 exhibits values of $T_2^{(QD1)} = (153 \pm 1)$ ps and $\theta^{(QD1)} = (2.08 \pm 0.01)$ GHz, and QD2 of $T_2^{(QD2)} = (123 \pm 4)$ ps and $\theta^{(QD2)} = (2.59 \pm 0.08)$ GHz.

7.2 Frequency Stabilization of a Single–Photon Source

In this section, we introduce the building blocks for frequency-stabilizing a single-photon source step-by-step. A Faraday filter is used as an atomic reference for frequency discrimination, and the amount of transmitted photons in a given time interval is used to determine deviations from a frequency set

---

[1] E.g. electrical triggering of single photons has already been demonstrated [234].

[2] A flow-cryostat as shown in Figure 7.1(a) (*CryoVac KONTI*) and a closed cycle cryostat (*attocube AttoDRY 1100*).
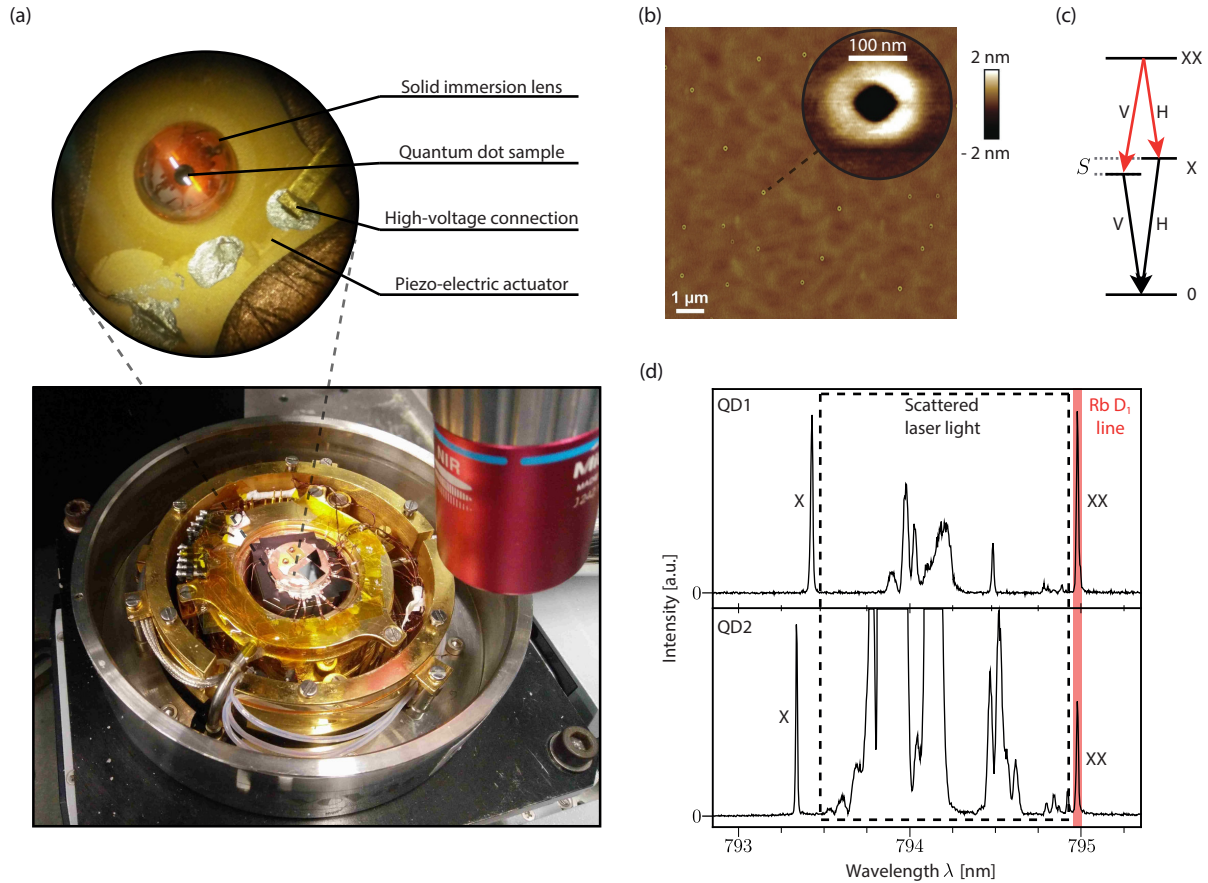
Figure 7.1: **(a)** Photograph of a GaAs/AlGaAs QD containing nano-membrane on a piezo-electric actuator. The copper baseplate beneath the sample is connected to the cold finger of the helium-flow cryostat. A solid immersion lens (top) in combination with a high-NA objective (bottom) allows for single-dot addressing and efficient photon collection. The black fragments are as-grown reference samples (wafer pieces). **(b)** Atomic force microscope (AFM) image of nano-holes in AlGaAs, which are to be filled with GaAs and capped with another layer of AlGaAs [216]. The obtained quantum dots have a lateral extent below 100 nm. The QD density of $\sim 0.1/\mu m^2$ allows to select one out of thousands for a measurement. **(c)** A two-photon excitation scheme resonantly addresses the biexciton state (XX), which decays via the exciton state (X) by emitting two consecutive photons (XX and X). The fine-structure splitting S of the X state leads to two cross-polarized XX-X decay channels (H and V). **(d)** Emission spectra of two separate GaAs/AlGaAs QDs, whose XX emission frequencies are tuned in resonance with the rubidium D_1 transition using piezo-induced strain fields. The scattered excitation laser is partially suppressed using notch filters. The data in (b) was kindly provided by Robert Keil.
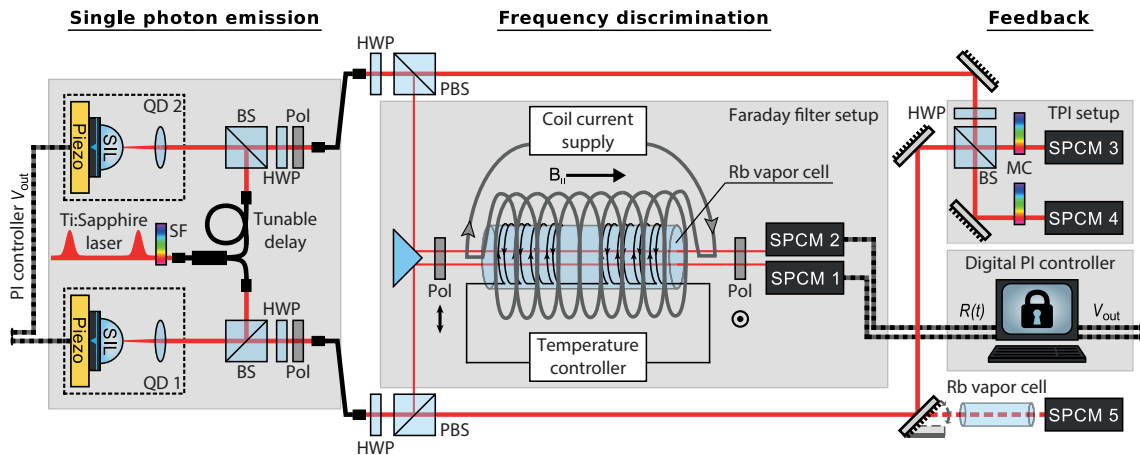
Figure 7.2: Experimental setup for two-photon interference (TPI) between separate, frequency-stabilized quantum dots (QDs). A pulsed Ti:sapphire laser resonantly excites the XX state of QD1 and QD2, positioned in separate cryostats at 4 K. Grating-based spectral filtering (SF) is applied to reduce the laser linewidth. A fiber-integrated, tunable delay adjusts the excitation to match arrival times of XX photons at the subsequent TPI setup. Both QDs are mounted on piezo-electric actuators for strain-induced emission frequency control. In each setup, the XX photons are collected using a confocal microscope, with the addition of a solid immersion lens (SIL) for enhanced extraction and a half-wave plate (HWP) and polarizer (Pol) for polarization filtering. A fraction of the signal is branched off by a HWP and a polarizing beam splitter (PBS) and sent through a Faraday filter setup. It consists of a heated, natural-abundance rubidium vapor cell in a longitudinal magnetic field, enclosed by two crossed polarizers. A coil current supply and a temperature controller enable tuning of the filter transmission features (see Fig. 7.4). The transmitted XX photons are detected by single-photon counting modules (SPCMs) 1 & 2 as signal inputs $R(t)$ for two digital proportional-integral (PI) controllers. Feedback voltages V_{out} are generated and applied to the piezoelectric actuators for QD frequency stabilization. An additional Rb vapor cell in the signal arm of QD1 permits characterization of frequency drifts independent of the Faraday filter. The remaining XX photon streams are sent to the TPI setup, consisting of a beam splitter (BS), monochromators (MCs) and SPCMs 3 & 4. A HWP in one input arm is used to set the photon (in)distinguishability with respect to the polarization state.

point. This allows to apply a correction signal via strain-tuning of the QD host material, resulting in a stabilized emitter frequency. The whole setup is displayed schematically in Figure 7.2. Here, we focus on the components required for feedback, while the TPI measurement and the corresponding setup part is described in Section 7.3.

It is worth to emphasize that not only QDs, but any single-photon source emitting at an atomic transition frequency may be stabilized with our feedback approach based on atomic line filtering and rate estimation.

7.2.1 The Faraday Filter as an Atomic Reference

The signal for frequency discrimination is provided by the Faraday effect: Light traveling through a dispersive atomic vapor will experience a polarization rotation, if a dc magnetic field is applied parallel to the propagation direction and if the frequency of the light is close to an atomic transition. Adding crossed polarizers before and after the vapor cell ensures that only the narrow frequency bands with a 90° polarization rotation are transmitted with a high efficiency. Such a setup is referred to as a *Faraday Anomalous Dispersion Optical Filter* (FADOF) [240, 241].

Using a narrow-band laser at 795 nm, in Figure 7.3 we illustrate the difference between simple
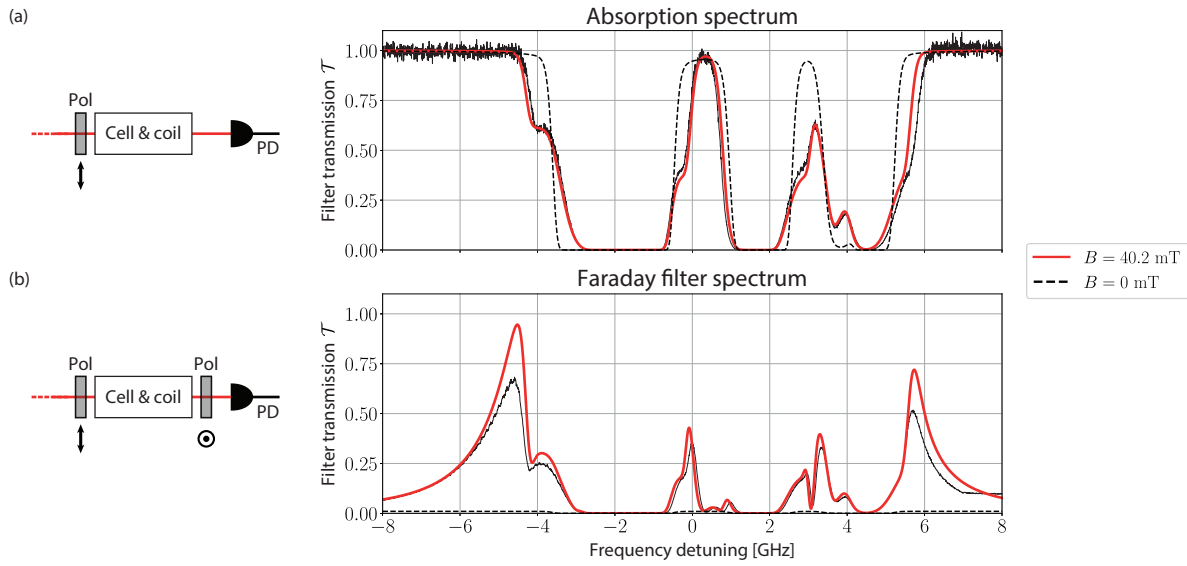
Figure 7.3: A weak, narrow-band laser is used to characterize **(a)** an absorption spectrum and **(b)** a Faraday filter spectrum, for which only an additional, crossed polarizer (Pol) before the photodiode (PD) has been introduced. Both spectra are measured in the presence of a magnetic field of $B_{\parallel} = 40.2$ mT. The fits (red lines) are carried out with the software *ElecSus* [242]. The detuning is given with respect to the weighted line center of the rubidium D_1 transitions. In the absence of a field ($B_{\parallel} = 0$ mT) the expected transmission is also shown (dashed, black lines).

absorption spectroscopy (a) and Faraday filtering (b). The latter depends on both temperature T and axially-applied magnetic field $B_{\parallel}$. These settings influence the transmission level as well as the overall spectrum in terms of peak positions and widths. In combination with spectrally broad emitters, having only two high-transmission features becomes advantageous, as we will see in Figure 7.5.

The magnetic field is generated by a homemade coil, which encloses the Rubidium vapor cell. Temperature adjustments are realized by a heating strip around the cell that avoids building up a magnetic field (see schematic filter in Figure 7.2). Since Joule heating by the coil also contributes to the overall temperature, we counteract this side-effect by regulated water cooling. To a certain extent the dissipated heat is desirable: A higher temperature leads to a higher filter transmission. However, the temperature cannot be set arbitrarily high; we are limited to 85° C. Then rubidium condensation occurs at the vapor cell windows, since the core temperature of the cell becomes higher than the window temperature. Figure 7.4(a) shows the resulting drop in filter transmission for 40.2 mT and 85° C.[3]

To compare measured Faraday filter spectra for given $B_{\parallel}$ and T settings with the expected ones, we use the software *ElecSus* [242] to calibrate the conversion from coil current to magnetic field and, more importantly, the absolute frequency axis. *ElecSus* calculates the electric susceptibility of alkali-metal vapors [245] to predict their absorptive and dispersive properties. The model includes effects such as dipole-dipole induced linewidth broadening [246] and axial magnetic fields [247]. The software is based on *Python* (v2.7) and has a GUI which simplifies data fitting, for which we leave free parameters for T, $B_{\parallel}$, additional broadening and the incident angle of polarization, whereas e.g. cell length and isotope abundance are fixed. From the parameter scan in Figure 7.4, we conclude that the recorded temperatures at the sensors close to the windows are not reflecting the actual temperature at the core of the cell, as for high magnetic fields the transmission is lower and the feature width higher than expected. This points at

---

[3] To point out a more extreme case: Starting at $\sim 120°$ C [243], absorption processes referred to as 'curing' take place [244].
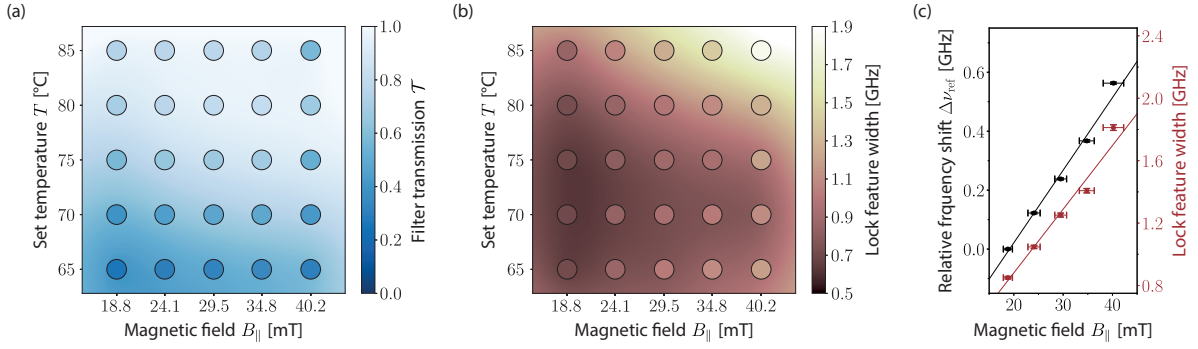
Figure 7.4: **(a)** Filter transmission as a function of set temperature T and applied magnetic field $B_\parallel$. The filled circles are measured transmission values for the leftmost peak in the Faraday filter transmission (see Fig. 7.3(b)). The expected values are interpolated and displayed in the background. **(b)** The width of the peak, which we call the *lock feature*, in dependence of the same parameters as in (a). We observe that despite the recorded temperatures at the sensors close to the cell windows, Joule heating of the magnetic field coil causes an even higher core temperature, which results in lower transmissions (rubidium condensation) and higher feature widths than expected ($B_\parallel = 40.2$ mT). **(c)** Frequency tunability of the central point on the falling lock-feature slope around rubidium transitions (cf. *set point* in Fig. 7.5(b)). Besides the coarse tuning via the temperature, tuning the magnetic field allows to shift the transmission peak of the filter, and thus the frequency set point of the stabilized emitter, accurately to a desired frequency near an atomic hyperfine resonance of the rubidium D_1 line – with 24.6 MHz/mT. As a convenient side effect, the width of the transmission peak changes with 40.8 MHz/mT and can be adjusted to match the linewidth of the QD.

the aforementioned condensation of rubidium.

After understanding the working principle of the filter and its characterization using a laser, we now look at the transmission properties of the photon stream emitted by a QD. As depicted in Figure 7.2, a part of each emission is directed to the filter. The expected transmission $\mathcal{T}_{QD}$ is given by a convolution of a narrow-band, weak laser transmission $\mathcal{T}_L$ with the broader spectral emission profile $f(\nu)$ of the QD, that is obtained from a coherence time measurement using a Michelson interferometer (Fig. 7.5(a)):

$$\mathcal{T}_{QD}(\nu) = (\mathcal{T}_L * f)(\nu).$$

Figure 7.5(b) shows the expected curve of $\mathcal{T}_{QD2}$ along with the measured frequency-tuned transmission of QD2. For a transmission peak close to the desired set frequency ν_{set}, the slope around ν_{set} serves as the error signal for frequency stabilization. Changes in frequency are directly translated to a variation of the FADOF transmission.

The coarse set point is chosen by the appropriate isotope abundance of rubidium. The set point of the stabilized frequency ν_{set} shown in Figure 7.5(b) has been selected for interfacing the XX photons with the $F = 2$ to $F' = 1, 2$ hyperfine transitions of the D_1 line of ^{87}Rb ($5^2S_{1/2} \rightarrow 5^2P_{1/2}$) only. In this case, a natural isotope abundance is required. If one is interested in addressing $F = 1$ to $F' = 1, 2$ instead, a pure ^{85}Rb vapor cell is the right choice, as can be simulated straightforward with *ElecSus*. The settings for transitions at the D_2 line (780 nm) are found likewise.[4]

Further adjustments to the set point are possible using the set temperature of the filter, see Figure 7.5(c).

---

[4] Experiments involving the ^{85}Rb isotope could also address e.g. $F = 3$ to $F' = 2, 3$ at 795 nm using a pure ^{87}Rb vapor cell, while $F = 2$ to $F' = 2, 3$ would be technically challenging due to a fairly low filter transmission at the appropriate set point, which is at the beginning of a slope.
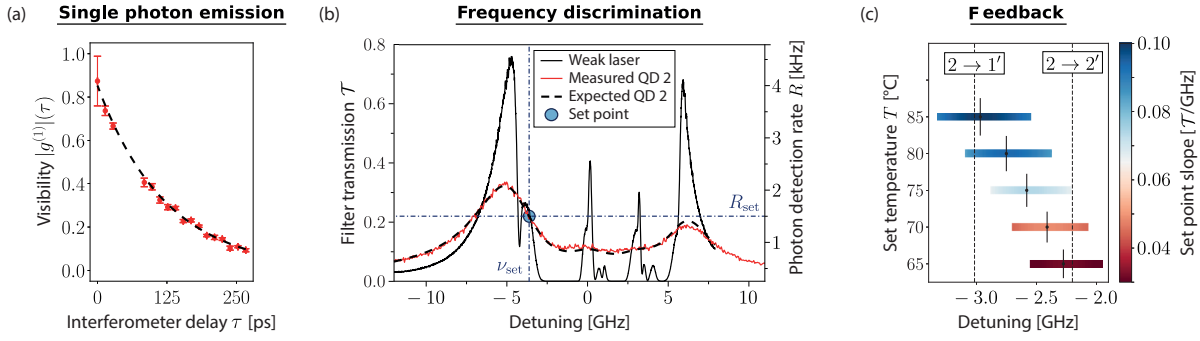
Figure 7.5: **(a)** The coherence $g^{(1)}(\tau)$ of XX photons emitted by QD2 is measured using a Michelson interferometer. From a fit (dashed, black line) to its absolute value we extract the coherence time $T_2^{(QD2)} = (123 \pm 4)$ ps and thus a Lorentzian linewidth of $\theta^{(QD2)} = (2.59 \pm 0.08)$ GHz, which has to be taken into account in the spectral emission profile $f(\nu)$ of QD2. **(b)** Faraday-filter transmission spectra measured with a weak, narrow-band laser (solid, black line) and with the frequency-tuned QD2 (red line). A convolution of the laser transmission with $f(\nu)$ of QD2 (dashed, black line) is used to model the QD transmission. The detuning is given with respect to the weighted line center of the rubidium D_1 transitions. The set point for the TPI measurement (Fig. 7.7) with the reference photon rate $R_{set} = R(\nu_{set})$ is highlighted. Frequency deviations are detected according to Equation 7.2. Only relatively weak photon streams (here: 6000 photons per second) are required to stabilize the frequency. The vapor cell was kept at a temperature of 85 °C and the magnetic field was set to 40 mT. **(c)** Rubidium hyperfine transitions $F \rightarrow F'$ are addressed by coarse adjustments of the set temperature T and fine-tuning of the magnetic field $B_\parallel$. For different temperatures and $B_\parallel = 29.5$ mT, the maximum set point slopes are marked, along with the windows over which the slope decreases by less than 10 %. Stabilizing the frequency to other atomic resonances is discussed in the main text.

For finer tuning, the magnetic field is sufficient, as shown in Figure 7.4(c). Simultaneously, the width of the transmission peak can be adjusted to match the linewidth of the QD.

In conclusion, we find that the Faraday filter delivers a reliable set point for any desired wavelength that addresses ^{87}Rb D-line transitions, including expedient detunings. Furthermore, in any interfacing experiment, the hyperfine transition of use is most likely fixed, such that an intermediate exchange of isotopes is obsolete.

7.2.2 Single–Photon Based Feedback Algorithm

The SPCM photon detection rate $R_{set} = R(\nu_{set})$ serves as the reference for frequency feedback. The rate $R(t)$ of photon events at the SPCM can be written as:

$$R(t) = R(\nu(t)) \equiv \mathcal{T}_{QD}(\nu(t)) \cdot R_{QD} \,, \tag{7.1}$$

which depends on the time-varying center frequency $\nu(t)$ of the QD's spectral emission profile and its emission rate R_{QD}. By inverting Equation 7.1, the instantaneous frequency deviation from the set point $\Delta\nu(t) \equiv \nu(t) - \nu_{set}$ can be determined, using the observed detection rate $R(t)$. In practice, deviations from the set point are kept small by the feedback loop and the linearized relation:

$$\Delta\nu \approx \frac{1}{\frac{dR}{d\nu}\big|_{\nu_{set}}} \Delta R \,, \tag{7.2}$$

63

with $\Delta R = R(t) - R_{\text{set}}$ provides a good approximation.

In order to obtain an error signal for feedback, a simple, empirical algorithm is implemented to estimate the underlying scattering rate at any point in time. Motivated by the fact that photon events lying further in the past convey less information and should thus be given lower weight with time, an exponential smoothing filter is chosen to estimate the count rate $R(t)$. The digital implementation is similar to a first order low pass filter and described by the pseudo-code:

$$R_{\text{estimate},n+1} = R_{\text{estimate},n} \cdot d + \mathcal{B} \cdot i$$

$$\text{where } \mathcal{B} = \begin{cases} 1, & \text{if a photon arrived} \\ 0, & \text{else}, \end{cases}$$

with the decrement $d = e^{-\tau_{\text{cycle}}/\tau_{\text{filter}}}$ and the increment $i = (1 - d)/\tau_{\text{cycle}}$. Here, τ_{cycle} and τ_{filter} denote the cycle time of the digital loop and the chosen integration time of the filter, respectively. Instead of using a discrete averaging window [228], our algorithm represents an infinite impulse response filter and thus features a smooth frequency response.

There are two important aspects for rate-based frequency estimations: The first one is the correct detection of variations in the scattering rate $R(t)$ from the stochastic train of photon detection events observed by the SPCM. We measure the free-running QD frequency-noise power spectral densities [248] on the rate $R(t)$ to determine the frequency at which the QD $1/f$-noise is exceeded by detection shot noise. Then the feedback bandwidth of the control system is set to a frequency well below (see Fig. 7.6(a,b)).

The second aspect is the distinction between rate variations due to frequency drifts and due to intensity changes in the QD emission. The latter could be compensated by adjusting the rate R_{set} with respect to a rate measurement before the Faraday filter. Another possibility is creating a dispersive error signal by taking the difference of the orthogonal circular components of the filter transmission [240]. In our experiment, QD intensity fluctuations due to sample drifts are taken into account by selecting data windows in which the count rate after the TPI setup is stable.

The rate estimation algorithm as well as a subsequent standard digital proportional-integral (PI) controller are implemented on a *field programmable gate array* (FPGA) [5] using *LabVIEW* [249]. The generated correction signal is sent to the strain-tuning piezoelectric actuator beneath the QD via a high-voltage amplifier. Due to *piezo creep*, a certain set voltage on the piezoelectric actuator does not result in a constant strain in the QD membrane. The strain slightly changes over time and therefore results in a frequency drift, which is compensated by the implemented stabilization.

7.2.3 Characterization of the Feedback Quality

For locking the QD emission frequencies, small count rates of only $R_{\text{set,QD1}} = 3600$ cps and $R_{\text{set,QD2}} = 1500$ cps are used. Figure 7.6(a) shows the frequency drift of QD1 for the frequency-locked and free-running case over a duration of $T = 40$ min. It is determined by measuring the photon transmission through a separate, heated rubidium vapor cell (see Fig. 7.2), which constitutes an out-of-loop measurement of the frequency drift. Frequency-stabilization leads to a constant frequency within a deviation of < 30 MHz [6], which is less than 1.5 % of the linewidths of the QD (≥ 2 GHz). In the free-running case, the frequency detuning $\Delta\nu(t)$ increases over time, following a logarithmic law known for the displacement

---

[5] *National Instruments NI PXI-7842R card*

[6] Calculated using $\sqrt{\sigma_N^2 - \overline{N}}$ to exclude the detection shot noise. $\overline{N}$ is the average count number for ≥ 0.5 s binning times and σ_N is the corresponding standard deviation.
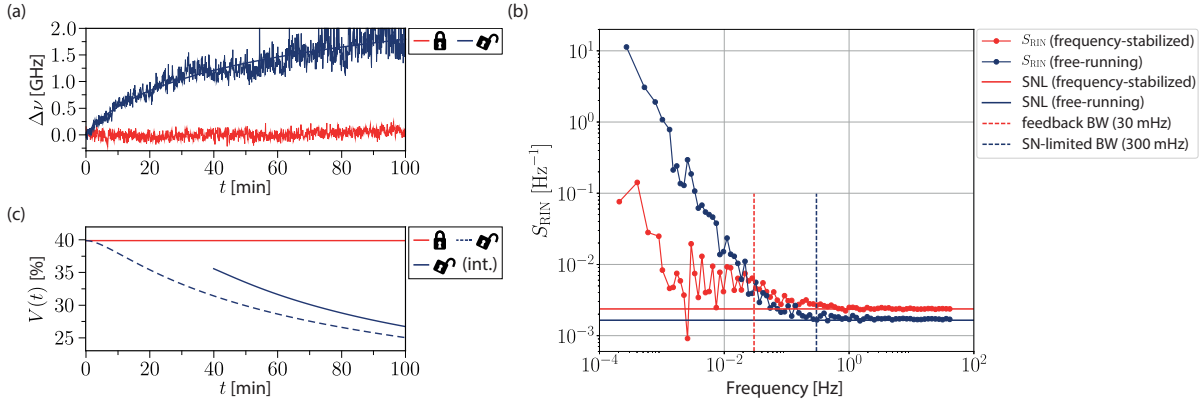
Figure 7.6: **(a)** Relative emission-frequency drift over time for QD1 in frequency-locked and free-running state, obtained by an out-of-loop measurement of the transmission through a separate Rb vapor cell. In the stabilized state the frequency is kept constant within a deviation of less than 30 MHz, which is below 1.5 % of the emission linewidth. The free-running state reveals a frequency drift due to *piezo creep*, which is fitted by a logarithmic function. **(b)** The relative intensity noise S_{RIN} of the free-running quantum dot emission (solid, blue line) after the out-of-loop frequency discriminator is calculated according to Equation 7.4 and allows to determine the maximum possible feedback bandwidth (BW), which is the intersection point of S_{RIN} with the shot noise level (SNL) (dashed, blue line). The point at which the frequency-locked emission S_{RIN} (solid, red line) is no longer lower than the free-running S_{RIN} indicates the chosen feedback bandwidth (dashed, red line). **(c)** Theoretically expected evolution of the TPI visibility $V(t)$ considering the frequency drift shown in (a). We use the experimentally determined lifetimes T_1 and coherence times T_2 of the two separate QDs to model $V(t)$. While the visibility stays constant in the frequency-locked case (red line), for free-running QDs it drops from $V_{\text{free}}(t = 0 \text{ min}) = 40$ % to $V_{\text{free}}(t = 100 \text{ min}) = 25$ % (dashed, blue line). The solid blue line represents the time-averaged visibility with a coincidence integration window of 40 min as used for the experiment in Figure 7.7(c).

change due to piezo creep [250]:

$$\Delta\nu(t) = \Delta\nu_0 \cdot [1 + \alpha \cdot \log_{10}(t - t_0)] .$$

Here, $\Delta\nu_0$ denotes the frequency detuning 1 minute after a certain voltage is applied to the piezo at a time t_0, and α describes the rate of the piezo creep, which depends on the applied voltage and the piezo load. The displayed data in Figure 7.6(a) is in good agreement with the model.

As a next step, we use the trace of N binned photon detection events x_n to determine the frequencies of the underlying fluctuations and drifts. They can only be detected up to the point, at which the photon detection shot noise starts dominating the relative intensity noise (RIN). For a given count rate $R = x_n/\Delta t$, this shot noise level (SNL) is given by:

$$\text{SNL} = \frac{2}{R} \tag{7.3}$$

in analogy to the shot noise for electric currents.

We determine the shot noise-limited bandwidth by first calculating the power spectral density $S_{xx}(\omega)$ from the count rate fluctuations in the time domain:

$$S_{xx}(\omega) = \lim_{T \to \infty} \frac{1}{T} \mathbf{E}\left[|\hat{x}_T(\omega)|^2\right] ,$$

where $\mathbf{E}$ denotes the expectation value and $\hat{x}_T(\omega)$ is the truncated Fourier transform given by:

$$\hat{x}_T(\omega) = \int_0^T x(t)e^{-i\omega t}\,dt\,.$$

Using $\omega = 2\pi f$ and the discretization of the time variable t [7], this expression can be re-written as:

$$\hat{x}_T(\omega) = \sum_{n=0}^{N} \underbrace{x(n\cdot\Delta t)}_{=x_n}\cdot\Delta t\cdot e^{-2\pi i f n\Delta t}$$

and

$$\hat{x}_T\left(\frac{k}{\Delta t\cdot N}\right) = \hat{x}_T\left(\frac{k}{T}\right) = \Delta t\cdot\sum_{n=0}^{N} x_n\cdot e^{-2\pi i\frac{nk}{N}}$$

$$= \mathrm{DFT}_k\,[x_n]\cdot\Delta t\,,$$

with $k = -\frac{N}{2},\ldots\frac{N}{2}-1$ being the Fourier components. Thus the power spectral density is given by:

$$S_{xx}(\omega) = \frac{\left|\hat{x}_T\left(\frac{k}{\Delta t\cdot N}\right)\right|^2}{T} = \frac{|\mathrm{DFT}_k\,[x_n]|^2\cdot(\Delta t)^2}{T}\,.$$

To obtain the relative intensity noise (RIN), one needs to normalize by the average count number $\bar{x}$:

$$S_{\mathrm{RIN}}(\omega) = \frac{S_{xx}(\omega)}{\bar{x}^2} = \frac{\left|\mathrm{DFT}_k\left[\frac{x_n}{\bar{x}}\right]\right|^2\cdot(\Delta t)^2}{T}\,. \tag{7.4}$$

For different temporal lengths T of the photon trace and binning sizes Δt as well as intensities, in the limit of high frequencies, Equation 7.4 has to lead to the SNL given by Equation 7.3.

The S_{RIN} in Figure 7.6(b) shows an $1/f$ behavior which leads to an intersection point with the SNL. This crossing indicates that a feedback bandwidth higher than 300 mHz would add additional noise to the quantum dot emission frequency. At the set point of $R_{\mathrm{set,QD2}}$, depicted in Figure 7.5(b), we choose 30 mHz by adjusting the digital PI parameters – one order of magnitude smaller than the limit. In Figure 7.6(b), this can be seen at the point, where the frequency-locked emission no longer exhibits less noise than the free-running one (for an extrapolated equal SNL).

To conclude, the feedback bandwidth is determined by the amount of photons branched off for frequency discrimination. The brighter a single photon source is, the more frequency noise can be suppressed. While narrowing the spectral emission profile $f(\nu)$ is rather unfeasible, our available rate of photons for frequency stabilization is sufficient to generate an ideal frequency overlap between the two photon streams, as we will see in the next section. It is important to point out that the bandwidth is not limited by our feedback scheme, but mainly by the available rate of photons. Quantum dots in general have shown emission rates of up to several tens of Megahertz [45]. With extremely high rates, the limitation in our approach is given by the piezo-electric actuators which are able to react to modulations up to the kHz regime.

---

[7] This step is necessary, since we numerically calculate the Fourier transformation with the SciPy module in Python.

7.3 Two–Photon Interference from Separate Quantum Dots

In this chapter we show an improved long-term two-photon interference (TPI) visibility of two frequency-stabilized QDs in a Hong-Ou-Mandel experiment[8]. Before we actually compare the visibility for stabilized and free-running emission, we estimate the ideally expected TPI visibility. In Section 7.1 the lifetimes of the XX state T_1 and the coherence times T_2 of the respective photons have been determined for both QDs that are used in this last experiment. We calculate the respective photon indistinguishabilities $I = T_2/(2T_1)$ [253], which are $I^{(\mathrm{QD1})} = (49.4 \pm 0.5)$ % and $I^{(\mathrm{QD2})} = (32.9 \pm 1.1)$ %. The obtained values indicate a presence of internal dephasing processes[9] in the QDs which degrade the photon indistinguishability. The latter also sets an upper limit to the achievable TPI visibility for interfering photons from the two separate dots. The visibility V is calculated by [219]:

$$V = \frac{\gamma_1 \gamma_2}{\gamma_1 + \gamma_2} \cdot \frac{\gamma_1 + \gamma_2 + \gamma_1^* + \gamma_2^*}{(2\pi\delta)^2 + (\gamma_1 + \gamma_2 + \gamma_1^* + \gamma_2^*)^2/4} , \tag{7.5}$$

with $\gamma_i = 1/T_1^{(\mathrm{QD}i)}$ denoting the radiative decay rate and $\gamma_i^* = (2/T_2^{(\mathrm{QD}i)} - \gamma_i)$ the pure dephasing rate for the different QDs (i =1,2). The frequency detuning between the photon streams from QD1 and QD2 is specified by δ. Interfering photons of identical frequency ($\delta = 0$) results in a maximum visibility of $V = 40$ %, while $\delta > 0$ reduces the visibility.

We use Equation 7.5 to calculate the theoretical TPI interference visibility for the locked and free-running QDs, taking the experimental parameters of the QD photons into account. Figure 7.6(c) shows the expected visibility over time, assuming a frequency drift between the two QD emission frequencies as observed in Figure 7.6(a). Perfect frequency stability results in the maximum achievable visibility of $V = 40$ %, while for the measured piezo creep the theoretically expected visibility drops to $V = 25$ % at t =100 min. This expected visibility is comparable to other QD based TPI experiments [219, 232, 255]. However, it has been shown that in principle visibilities as high as 98% can be obtained, e.g. by using charge-tunable QD devices [231]. For quantum repeater applications, photon indistinguishabilities of 99% are ultimately required [256]. As we present in the following, the maximum visibility – together with tunability to an atomic transition – is only accessible using efficient frequency feedback.

In order to experimentally verify an improved long-term visibility under frequency stabilization, we compare the TPI of photons from two separate QDs in the frequency-locked and free-running state. Each QD emission is coupled into a single-mode fiber, delivering a photon rate of $R_{\mathrm{QD}} \approx 30$ kcps. One part of each single-photon stream is sent to the TPI setup. It consists of a 50:50 non-polarizing beam splitter (BS), followed by monochromators for further background suppression and single-photon counting modules (SPCMs) in each output arm, see Figure 7.2. If photons with equal properties (frequency, polarization, spatio-temporal mode structure) impinge on a 50:50 beam splitter (BS) at the same time, the probability amplitudes for simultaneous transmission and reflection interfere destructively, such that only pairwise propagation after the BS is possible (Fig. 7.7(a)). Equal rates at the BS input ports ensure a maximum peak at zero delay in the crossed polarizations case. For the HOM measurement, we have rates of 5 kcps per QD available.

For stabilized QDs, Figure 7.7(b) shows the normalized coincidences of photons in the two beam splitter output ports versus the delay time τ between the recorded events. The polarization state between the interfering photons is controlled by a half-wave plate. The interference visibility V is calculated by

---

[8] HOM interference has also been shown for single photons provided by atomic systems [251] and SPDC sources [252].

[9] It is not clear what causes them, it could be related to charge noise in the vicinity of the QDs or spectral jittering due to charge traps [254].
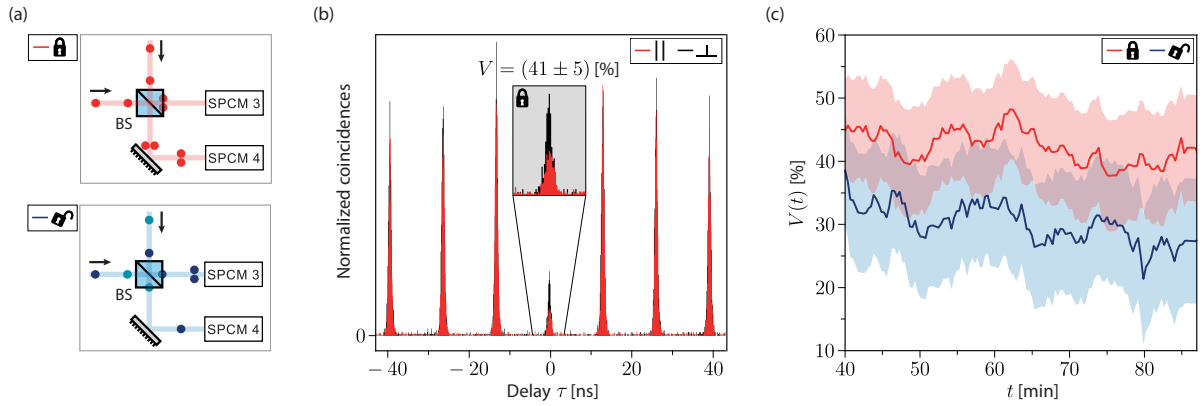
Figure 7.7: **(a)** Schematic illustration of the expected outcome of a Hong-Ou-Mandel experiment in the cases of frequency-stabilized and free-running QD emission. If photons with equal properties (frequency, polarization, spatio-temporal mode structure) impinge on a 50:50 beam splitter (BS) at the same time, the probability amplitudes for simultaneous transmission and reflection interfere destructively, such that only pairwise propagation after the BS is possible. **(b)** Two-photon interference measurement between two frequency-stabilized, separate QDs, showing the normalized coincidences versus the delay time τ. The black curve corresponds to perpendicular polarizations of the photons arriving at the BS. The red curve for parallel polarizations depicts a clear reduction of coincidences at $\tau \approx 0$. An interference visibility of $V_{\text{lock}} = (41 \pm 5)$ % is obtained. A similar measurement of the visibility with free-running QDs (not shown) results in $V_{\text{free}} = (31 \pm 7)$ %. **(c)** Measurement of the interference visibility over time for both free-running and frequency-locked QDs. Each data point corresponds to the coincidences obtained for the previous 40 min. The shaded areas are the respective uncertainties based on Poisson counting statistics. At any measurement time the visibility is higher for frequency-locked QDs than for free-running QDs.

evaluating the peak areas $A_\parallel$ for parallel and $A_\perp$ for perpendicular polarizations of photons impinging on the beam splitter at $\tau = 0$:

$$V = \frac{A_\perp - A_\parallel}{A_\perp} .$$

A clear Hong-Ou-Mandel dip is observed, yielding an interference visibility of $V_{\text{lock}} = (41 \pm 5)$ % after dark count correction of the SPCMs ($R_{\text{dc,SPCM3}} = 104$ cps, $R_{\text{dc,SPCM4}} = 134$ cps). The visibility agrees well with the expected value of $V = 40$ % in Figure 7.6(c). Afterwards, a measurement with free-running QDs is performed. The visibility in that case decreases to $V_{\text{free}} = (31 \pm 7)$ %, due to piezo creep and other emission frequency perturbations. For ideal quantum emitters the ratio of the peak at $\tau = 0$ compared to the neighboring peaks equals 0.5 for perpendicular photon polarizations and low emission rates. For perfectly bright sources with one photon per trigger pulse, this ratio would increase to 2/3. The origin of these numbers can be understood if all detection cases including the possibility of photon absences are scaled with the probability of having a photon at the BS input port at all. In our case, by comparing the detection rate of 5 kcps with the excitation rate of 76 MHz, we are allocated to the dark emitter limit and expect 0.5. Here, a lower ratio is observed, which can be attributed to blinking[10] of the QD emission [209, 257]. Recorded intensity traces of the photon streams indicate that there is no blinking on long timescales (milliseconds to hours). In order to observe blinking at shorter timescales, the second-order autocorrelations $g^{(2)}(\tau)$ are measured for both QDs, using an HBT setup. The result, as shown in [1, 254], shows a significant bunching at small delay times, which is a signature of blinking of the QD emission. Fitting a bi-exponential results in characteristic blinking timescales of

---

[10] Which can be understood as a high-frequency imbalancing of the emission rates, see previous discussion.

$T_{\rm b}^{\rm (QD1)}$ = 332 ns and $T_{\rm b}^{\rm (QD2)}$ = 27 ns, to which the frequency stabilization is insensitive. The blinking effect can be attributed e.g. to the dark excitonic state [258].

To further compare the two cases of TPI with and without frequency feedback, the interference visibility is measured as a function of time, as shown in Figure 7.7(c). Each respective data point corresponds to the coincidences obtained within the previous 40 min. Hence, the integration window is gradually shifted through the total measurement time of 87 min. The shaded areas display the respective uncertainties due to Poissonian counting statistics. In the locked and free-running case, both QDs were frequency-matched at t =0 min. In the free-running case, frequency changes in the QD emission within the first integration window reduce the visibility for the first data points already (cf. Fig. 7.6(c)).

In conclusion, we have verified that active frequency feedback solely based on measurements of the emitted single photons is an attractive solution to maintain long-term indistinguishability of photons from separate solid-state emitters. The rubidium-based Faraday filter offers a common, absolute frequency reference for distant nodes in a quantum network. Furthermore, matching atomic transitions is desirable for atom-based quantum memories as potential elements in quantum repeaters. Low filter losses and an efficient rate-estimation algorithm ensure an effective frequency stabilization. Although we are only using a small fraction of the photon flux, frequency fluctuations are suppressed to a negligible fraction of the emission linewidth. While we have shown that the frequency of emitted photons can be kept at a set point around rubidium transitions, their bandwidth is still a problem that has to be solved in order to combine the two platforms efficiently. Here, the sample growth plays an important role [259]. Also internal dephasing processes have to be kept at a minimum to ensure transform-limited linewidths [260].

Outlook

I͟N this thesis I presented the storage of short light pulses in a CQED system consisting of a rubidium atom coupled to a high-bandwidth fiber Fabry-Pérot resonator. The strong light-matter interaction enables input-pulse durations shorter than the excited state lifetime of the atomic species. The subsequent generation of a single photon with a controllable temporal waveform does not only witness the successful preceding storage, but in principle also creates an entangled state between the internal state of the atom and the polarization of the generated photon. This is a consequence of the tripod configuration, in which the system is prepared. While for memory applications a Λ-system is preferred, this scheme offers interesting possibilities for entanglement distribution, as we will see in this chapter.

The ability to interact with photons of short duration furthermore encourages hybrid experiments involving semiconductor quantum dots, for which we have already demonstrated frequency-stabilization of the QD emission to atomic transitions [1]. The bandwidth mismatch between the two platforms is currently being resolved by the growth of quantum dot samples with lifetime-limited emission and optical resonators with high bandwidths – like the one employed in the presented experiments. Moreover, making use of GRIN lenses and reducing the losses due to scattering and absorption, an overall boost in quantum memory efficiency is to be expected.

Towards Hybrid Quantum Networks

The rapidly expanding field of quantum hybrid systems aims at the development of practical technologies that overcome the limitations imposed by a single platform, e.g. QDs are producing single photons at remarkable rates [261], but their applicability as a quantum memory is still discussed [262, 263]. Atomic systems, on the other hand, are approaching storage times of half a second [24]. From my personal point of view, this shows that our field has to make a transition from separate laboratories to collaboration networks or research centers, in which different systems – or at least our knowledge about them – can be combined. Fascinating examples for hybrid experiments include the entanglement of successive atom-cavity photons in a photonic chip [264], the interaction between a single trapped ion and resonant, heralded single photons from an entangled-photon source based on spontaneous parametric down-conversion (SPDC) [182] and a semiconductor–atomic interface for slowing down single photons emitted by a quantum dot [265].

In that line, I will propose two long-term goals that could be realized in our current fruitful collaboration with the group of O. Schmidt: The storage of a quantum-dot photon in an atomic ensemble and entanglement swapping between a *real* and an *artificial* atom. But also our CQED system on its own offers interesting possibilities, such as the dissipative entanglement of two atoms [266], the possible implementation of which has already been discussed in [51].

Storage of Even Shorter Light Pulses in an Atomic Ensemble

We have reduced the discrepancy between the bandwidths of our chosen atomic species and a short light pulse by interfacing both via an impedance matching element – namely our open cavity. But its linewidth low-pass filters shorter i.e. spectrally broader pulses. So how can we provide a more efficient quantum memory in the presence of a bandwidth mismatch? Before exchanging the resonator itself with a *fast* cavity [184], we can try to improve the storage efficiency, for which we have two major options: First, the light-matter coupling $\sqrt{N} \cdot g$ can be increased by employing ensembles of N atoms. An incoming photon will be mapped into a coherent superposition of any out of the atoms being transferred to the target ground state, creating a so-called *Dicke state* [267, 268]. In other terms, with an increase of g, the transfer to the excited state, from where we can map to the target ground state, happens faster than the cavity field decay. Thus for $g \gg \kappa$, the photon is captured with a higher probability than in the presented measurements with $g \approx \kappa$. A promising technique to place tens of atoms into the optical lattice within the cavity mode is based on spatial atomic ensemble compression [269] and has been realized in the prior experiment [60]. Without compression, we have already observed more than 6 atoms in the cavity region [51]. Second, and more importantly, a clean Λ-system should be realized by making the cavity resonant with the $|1\rangle \rightarrow |1'\rangle$ transition and preparing the atoms in the state $|1, 0\rangle$ [23]. This can be achieved by optical pumping with π-light, which unfortunately bears the risk of heating the atoms and requires improving our cooling method.

Realizing $|1, 0\rangle$ as an initial state also enables the storage of quantum information encoded in the polarization of a light pulse. Depending on whether it drives the σ^+ or the σ^--transition, the atom is transferred to $|2, +1\rangle$ or $|2, -1\rangle$, as depicted in Figure 8.1(a). The storage fidelity is obtained by a full quantum state tomography [270], for which we have already built a setup [271].

Even without encoding quantum information in the incoming pulse, the storage of shorter coherent pulses – or even true single photons – will be a significant step towards the interconnection of different platforms.

Entanglement Swapping with Real and Artificial Atoms

A prerequisite for my following proposal is the emission of entangled-photon pairs, as it is the case for a vanishing spin-related fine-structure splitting (FSS) between the intermediate exciton states [216]. Unfortunately, as soon as the exciton frequency is stabilized to a rubidium transition according to our scheme, the FSS is altered due to the applied strain field. We therefore propose to split the (bi)exciton emission according to its polarization and to use two orthogonal degrees of freedom to stabilize the frequency and the FSS *simultaneously* [272]. This could be done by two independent control loops with significantly different bandwidths or with two orthogonal degrees of freedom for feedback, as available in anisotropic strain-tuning platforms [227].

Alternatively, a QD which is naturally emitting close to rubidium lines and does not have to be tuned over a wide wavelength range has to be chosen. The group of O. Schmidt has recently reported on the emission of entangled photon pairs around the D_2 line [254]. Fine-tuning of the frequency has been possible via the temperature, which does not affect the FSS.

The exciton photon can either be used for storage experiments with polarization-encoded quantum information, or for entangling the atom with the biexciton photon (via entanglement swapping) at a wavelength, that is 'alien' to rubidium – i.e. atom-photon entanglement, that could not be created with our system alone. Furthermore, this can be understood as a proof-of-principle demonstration of quantum frequency conversion [273] from 780 to 781.6 nm [254]. However, for entanglement distribution in quantum networks, the common focus is on state-of-the-art fiber technologies at telecom bands. The
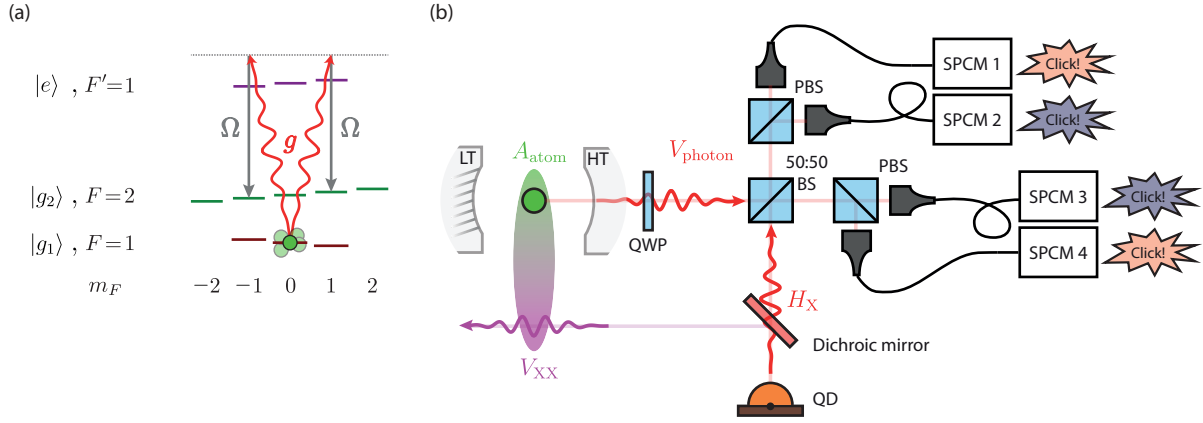
Figure 8.1: **(a)** Polarization-dependent storage of a light pulse in an atomic ensemble. As opposed to the scheme in Figure 6.6(a), the atoms have to be initialized in $|1,0\rangle$ to realize a clean Λ-system, in which polarization-encoded qubits can be stored. **(b)** Entanglement swapping with a real and an artificial atom (QD) in a hybrid experiment. In a tripod configuration (see Fig. 5.1(b)) photon generation creates entanglement between the atom-cavity photon and the atomic m_F-states A_{atom} and B_{atom} (Eq. 8.1). Biexciton (XX) and exciton (X) photons emitted by the quantum dot are entangled as well (Eq. 8.2, see Fig. 7.1(c)). A dichroic mirror is used to separate X and XX, while the quarter-wave plate (QWP) transforms circular to linear polarizations. A Bell measurement is performed with the exciton and cavity photons, using a 50:50 beam splitter (BS) and polarizing beam splitters (PBS) according to the Innsbruck detection scheme [275]. The state in Equation 8.3 is created when a coincidence is detected by the SPCMs (two examples shown). The illustration considers V_{photon} and H_{X} which projects the entangled state onto $|A_{\text{atom}}V_{\text{XX}}\rangle$.

wavelength conversion of an entangled photon can be realized by quantum frequency down-conversion to the C-band at 1560 nm [274] to finally realize an atomic quantum memory entangled with an outgoing telecom photon.

The idea for the experiment is graphically sketched in Figure 8.1(b). A photon is generated by applying a control pulse to the atom prepared in $|1,0\rangle$. This results in a circularly polarized photon, which is transformed to the H,V-basis by a quarter-wave plate, resulting in the entangled atom-photon state

$$\frac{1}{\sqrt{2}}\left(|H_{\text{photon}}A_{\text{atom}}\rangle + |V_{\text{photon}}B_{\text{atom}}\rangle\right), \tag{8.1}$$

where A_{atom} and B_{atom} are Zeeman states the atom is transferred to. At the same time, the biexciton cascade of the QD is triggered, delivering polarization-entangled photons in the H,V-basis:

$$|\Phi^+_{\text{X, XX}}\rangle = \frac{1}{\sqrt{2}}\left(|H_{\text{X}}H_{\text{XX}}\rangle + |V_{\text{X}}V_{\text{XX}}\rangle\right). \tag{8.2}$$

Both cavity and QD photon are sent to a 50:50 beam splitter, where a Bell measurement [275] is performed and unambiguously detects the Bell states $\Psi^\pm$. This event indicates the creation of the entangled state

$$\frac{1}{\sqrt{2}}\left(|A_{\text{atom}}V_{\text{XX}}\rangle + |B_{\text{atom}}V_{\text{XX}}\rangle\right). \tag{8.3}$$

While the biexciton photon can be directly analyzed with respect to its polarization, the atomic state has to be read out by applying an m_F-state selective π-pulse which transfers the population e.g. from A_{atom}

back to $F = 1$. A subsequent, second photon generation attempt will only be successful, if the atom has been in the state A_{atom}. Finally, this means that the entanglement-swapping success is confirmed by a 4-fold coincidence.

Bibliography

[1] M. Zopf, T. Macha, R. Keil, E. Uruñuela, Y. Chen, W. Alt, L. Ratschbacher, F. Ding,
     D. Meschede and O. G. Schmidt,
     "Frequency feedback for two-photon interference from separate quantum dots",
     Physical Review B 98 (2018) 161302(R).

[2] E. Kästner, *Die Schildbürger*, Dressler, 2006.

[3] E. Sielaff, *Die Schildbürger. Nach der ersten Ausgabe von 1598 und dem Narrenbuch von 1811
     für die Jugend bearbeitet von Erich Sielaff.* Der Kinderbuchverlag, 1965.

[4] C. H. Bennett and G. Brassard,
     "Quantum cryptography: Public key distribution and coin tossing",
     Theoretical Computer Science 560 (2014) 7.

[5] M. A. Nielsen and I. L. Chuang, *Quantum Computation and Quantum Information*,
     Cambridge University Press, 2010.

[6] R. P. Feynman, "Simulating physics with computers",
     International Journal of Theoretical Physics 21.6-7 (1982) 467.

[7] P. W. Shor, "Polynomial-Time Algorithms for Prime Factorization and Discrete Logarithms on a
     Quantum Computer", SIAM Journal on Computing 26.5 (1997) 1484.

[8] V. Giovannetti, "Quantum-Enhanced Measurements: Beating the Standard Quantum Limit",
     Science 306.5700 (2004) 1330.

[9] T. E. Northup and R. Blatt, "Quantum information transfer using photons",
     Nature Photonics 8 (2014) 356.

[10] Y. Li, P. C. Humphreys, G. J. Mendoza and S. C. Benjamin,
      "Resource Costs for Fault-Tolerant Linear Optical Quantum Computing",
      Physical Review X 5 (2015) 041007.

[11] Y.-W. Cho, G. T. Campbell, J. L. Everett, J. Bernu, D. B. Higginbottom, M. T. Cao, J. Geng,
      N. P. Robins, P. K. Lam and B. C. Buchler,
      "Highly efficient optical quantum memory with long coherence time in cold atoms",
      Optica 3.1 (2016) 100.

[12] A. I. Lvovsky, B. C. Sanders and W. Tittel, "Optical quantum memory",
      Nature Photonics 3.12 (2009) 706.

[13] J. I. Cirac and P. Zoller, "Quantum Computations with Cold Trapped Ions",
      Physical Review Letters 74.20 (1995) 4091.

[14] M. H. Devoret and J. M. Martinis,
      "Implementing qubits with superconducting integrated circuits",
      Experimental Aspects of Quantum Computing, 2005.

[15] J. I. Cirac, P. Zoller, H. J. Kimble and H. Mabuchi, "Quantum State Transfer and Entanglement Distribution among Distant Nodes in a Quantum Network", Physical Review Letters 78.16 (1997) 3221.

[16] H. J. Kimble, "The quantum internet", Nature 453 (2008) 1023.

[17] A. Reiserer and G. Rempe, "Cavity-based quantum networks with single atoms and optical photons", Reviews of Modern Physics 87.4 (2015) 1379.

[18] S. Haroche and D. Kleppner, "Cavity quantum electrodynamics", Physics Today 42.1 (1989) 24.

[19] M. Mücke, J. Bochmann, C. Hahn, A. Neuzner, C. Nölleke, A. Reiserer, G. Rempe and S. Ritter, "Generation of single photons from an atom-cavity system", Physical Review A 87.6 (2013) 063805.

[20] P. B. R. Nisbet-Jones, J. Dilley, D. Ljunggren and A. Kuhn, "Highly efficient source for indistinguishable single photons of controlled shape", New Journal of Physics 13.10 (2011) 103036.

[21] W. Chen, K. M. Beck, R. Bucker, M. Gullans, M. D. Lukin, H. Tanji-Suzuki and V. Vuletic, "All-Optical Switch and Transistor Gated by One Stored Photon", Science 341.6147 (2013) 768.

[22] A. Reiserer, N. Kalb, G. Rempe and S. Ritter, "A quantum gate between a flying optical photon and a single trapped atom", Nature 508.7495 (2014) 237.

[23] H. P. Specht, C. Nölleke, A. Reiserer, M. Uphoff, E. Figueroa, S. Ritter and G. Rempe, "A single-atom quantum memory", Nature 473.7346 (2011) 190.

[24] M. Körber, O. Morin, S. Langenfeld, A. Neuzner, S. Ritter and G. Rempe, "Decoherence-protected memory for a single-photon qubit", Nature Photonics 12.1 (2018) 18.

[25] S. Ritter, C. Nölleke, C. Hahn, A. Reiserer, A. Neuzner, M. Uphoff, M. Mücke, E. Figueroa, J. Bochmann and G. Rempe, "An elementary quantum network of single atoms in optical cavities", Nature 484.7393 (2012) 195.

[26] M. Lettner, M. Mücke, S. Riedl, C. Vo, C. Hahn, S. Baur, J. Bochmann, S. Ritter, S. Dürr and G. Rempe, "Remote Entanglement between a Single Atom and a Bose-Einstein Condensate", Physical Review Letters 106 (2011) 210503.

[27] Y. Tamura, H. Sakuma, K. Morita, M. Suzuki, Y. Yamamoto, K. Shimada, Y. Honma, K. Sohma, T. Fujii and T. Hasegawa, "The First 0.14-dB/km Loss Optical Fiber and its Impact on Submarine Transmission", Journal of Lightwave Technology 36.1 (2018) 44.

[28] W. K. Wootters and W. H. Zurek, "A single quantum cannot be cloned", Nature 299 (1982) 802.

[29] L.-M. Duan, M. D. Lukin, J. I. Cirac and P. Zoller, "Long-distance quantum communication with atomic ensembles and linear optics", Nature 414.6862 (2001) 413.

[30] W. Dür, H.-J. Briegel, J. I. Cirac and P. Zoller, "Quantum repeaters based on entanglement purification", Physical Review A 59 (1999) 169.

[31] M. Uphoff, M. Brekenfeld, G. Rempe and S. Ritter, "An integrated quantum repeater at telecom wavelength with single atoms in optical fiber cavities", Applied Physics B 122.3 (2016) 46.

[32]   N. Sangouard, C. Simon, H. de Riedmatten and N. Gisin,
"Quantum repeaters based on atomic ensembles and linear optics",
Reviews of Modern Physics 83.1 (2011) 33.

[33]   J. H. Prechtel, A. V. Kuhlmann, J. Houel, L. Greuter, A. Ludwig, D. Reuter, A. D. Wieck and
R. J. Warburton, "Frequency-Stabilized Source of Single Photons from a Solid-State Qubit",
Physical Review X 3 (2013) 041006.

[34]   N. Akopian, R. Trotta, E. Zallo, S. Kumar, P. Atkinson, A. Rastelli, O. G. Schmidt and V. Zwiller,
"An artificial atom locked to natural atoms", arXiv preprint: 1302.2005 (2013).

[35]   A. Muller, E. B. Flagg, J. R. Lawall and G. S. Solomon,
"Ultrahigh-finesse, low-mode-volume Fabry-Perot microcavity",
Optics letters 35.13 (2010) 2293.

[36]   L. Greuter, S. Starosielec, D. Najer, A. Ludwig, L. Duempelmann, D. Rohner and
R. J. Warburton,
"A small mode volume tunable microcavity: Development and characterization",
Applied Physics Letters 105.12 (2014) 121105.

[37]   D. Hunger, T. Steinmetz, Y. Colombe, C. Deutsch, T. W. Hänsch and J. Reichel,
"A fiber Fabry–Perot cavity with high finesse", New Journal of Physics 12.6 (2010) 065038.

[38]   J. Gallego, S. Ghosh, S. K. Alavi, W. Alt, M. Martinez-Dorantes, D. Meschede and
L. Ratschbacher,
"High-finesse fiber Fabry-Pérot cavities: stabilization and mode matching analysis",
Applied Physics B 122.3 (2016) 47.

[39]   J. Gallego, W. Alt, T. Macha, M. Martinez-Dorantes, D. Pandey and D. Meschede,
"Strong Purcell Effect on a Neutral Atom Trapped in an Open Fiber Cavity",
Physical Review Letters 121 (2018) 173603.

[40]   Y. Colombe, T. Steinmetz, G. Dubois, F. Linke, D. Hunger and J. Reichel,
"Strong atom-field coupling for Bose-Einstein condensates in an optical cavity on a chip",
Nature 450.7167 (2007) 272.

[41]   Y. H. Lien, G. Barontini, M. Scheucher, M. Mergenthaler, J. Goldwin and E. A. Hinds,
"Observing coherence effects in an overdamped quantum system",
Nature Communications 7 (2016) 13933.

[42]   Y. Wang, X. Zhang, T. A. Corcovilos, A. Kumar and D. S. Weiss,
"Coherent Addressing of Individual Neutral Atoms in a 3D Optical Lattice",
Physical Review Letters 115.4 (2015) 043003.

[43]   D. Schrader, I. Dotsenko, M. Khudaverdyan, Y. Miroshnychenko, A. Rauschenbeutel and
D. Meschede, "Neutral Atom Quantum Register", Physical Review Letters 93.15 (2004) 150501.

[44]   G. Kurizki, P. Bertet, Y. Kubo, K. Mølmer, D. Petrosyan, P. Rabl and J. Schmiedmayer,
"Quantum technologies with hybrid systems",
Proceedings of the National Academy of Sciences 112.13 (2015) 3866.

[45]   N. Somaschi, V. Giesz, L. De Santis, J. C. Loredo, M. P. Almeida, G. Hornecker, S. L. Portalupi,
T. Grange, C. Antón, J. Demory, C. Gómez, I. Sagnes, N. D. Lanzillotti-Kimura, A. Lemaítre,
A. Auffeves, A. G. White, L. Lanco and P. Senellart,
"Near-optimal single-photon sources in the solid state", Nature Photonics 10 (2016) 340.

[46] S. Haroche and J.-M. Raimond, *Exploring the Quantum: Atoms, Cavities, and Photons*,
      Oxford University Press, 2006.

[47] A. J. Shields, "Semiconductor quantum light sources", Nanoscience and Technology (2010) 221.

[48] M. B. Ward, M. C. Dean, R. M. Stevenson, A. J. Bennett, D. J. P. Ellis, K. Cooper, I. Farrer,
      C. A. Nicoll, D. A. Ritchie and A. J. Shields,
      "Coherent dynamics of a telecom-wavelength entangled photon source",
      Nature Communications 5 (2014).

[49] J.-P. Jahn, M. Munsch, L. Béguin, A. V. Kuhlmann, M. Renggli, Y. Huo, F. Ding, R. Trotta,
      M. Reindl, O. G. Schmidt, A. Rastelli, P. Treutlein and R. J. Warburton,
      "An artificial Rb atom in a semiconductor with lifetime-limited linewidth",
      Physical Review B 92.24 (2015) 245439.

[50] R. H. Dicke, "Coherence in Spontaneous Radiation Processes", Physical Review 93 (1954) 99.

[51] J. C. Gallego Fernández,
      "Strong Coupling between Small Atomic Ensembles and an Open Fiber Cavity",
      PhD thesis: Universität Bonn, 2017.

[52] L. Paulet, "Raman and Microwave Manipulation of Small Atomic Ensembles",
      MSc thesis: Universität Bonn, 2014.

[53] E. L. Raab, M. Prentiss, A. Cable, S. Chu and D. E. Pritchard,
      "Trapping of Neutral Sodium Atoms with Radiation Pressure",
      Physical Review Letters 59.23 (1987) 2631.

[54] D. Schrader, S. Kuhr, W. Alt, M. Müller, V. Gomer and D. Meschede,
      "An optical conveyor belt for single neutral atoms", Applied Physics B 73.8 (2001) 819.

[55] S. Kuhr, W. Alt, D. Schrader, M. Müller, V. Gomer and D. Meschede,
      "Deterministic Delivery of a Single Atom", Science 293.5528 (2001) 278.

[56] I. Dotsenko, W. Alt, M. Khudaverdyan, S. Kuhr, D. Meschede, Y. Miroshnychenko, D. Schrader
      and A. Rauschenbeutel, "Submicrometer position control of single trapped neutral atoms",
      Physical Review Letters 95.3 (2005) 033002.

[57] T. Hänsch and B. Couillaud,
      "Laser frequency stabilization by polarization spectroscopy of a reflecting reference cavity",
      Optics Communications 35.3 (1980) 441.

[58] D. A. Steck, "Rubidium 87 D Line Data", (2015).

[59] A. Neuzner, S. Dürr, M. Körber, S. Ritter and G. Rempe,
      "Increased dimensionality of Raman cooling in a slightly nonorthogonal optical lattice",
      Physical Review A 98 (2018) 013401.

[60] M. Martinez-Dorantes,
      "Fast non-destructive internal state detection of neutral atoms in optical potentials",
      PhD thesis: Universität Bonn, 2016.

[61] M. Martinez-Dorantes, W. Alt, J. Gallego, S. Ghosh, L. Ratschbacher, Y. Völzke and
      D. Meschede,
      "Fast Nondestructive Parallel Readout of Neutral Atom Registers in Optical Potentials",
      Physical Review Letters 119 (2017) 180503.

[62]   M. Martinez-Dorantes, W. Alt, J. Gallego, S. Ghosh, L. Ratschbacher and D. Meschede, "State-dependent fluorescence of neutral atoms in optical potentials", Physical Review A 97 (2018) 023410.

[63]   R. Reimann, "Cooling and Cooperative Coupling of Single Atoms in an Optical Cavity", PhD thesis: Universität Bonn, 2014.

[64]   S. Chu, J. E. Bjorkholm, A. Ashkin and A. Cable, "Experimental observation of optically trapped atoms", Physical Review Letters 57.3 (1986) 314.

[65]   C. J. Hood, T. W. Lynn, A. C. Doherty, A. S. Parkins and H. J. Kimble, "The atom-cavity microscope: single atoms bound in orbit by single photons", Science 287.5457 (2000) 1447.

[66]   P. W. H. Pinkse, T. Fischer, P. Maunz and G. Rempe, "Trapping an atom with single photons", Nature 404.6776 (2000) 365.

[67]   A. C. Doherty, T. W. Lynn, C. J. Hood and H. J. Kimble, "Trapping of single atoms with single photons in cavity QED", Physical Review A 63.1 (2001) 1.

[68]   R. Reimann, W. Alt, T. Macha, D. Meschede, N. Thau, S. Yoon and L. Ratschbacher, "Carrier-free Raman manipulation of trapped neutral atoms", New Journal of Physics 16.11 (2014) 113042.

[69]   E. Keiler, Lab support during MSc studies: Universität Bonn, 2018.

[70]   E. Uruñuela, "Imaging and addressing of neutral atoms inside a fiber cavity", MSc thesis: Universität Bonn, 2017.

[71]   E. D. Black, "An introduction to Pound–Drever–Hall laser frequency stabilization", American Journal of Physics 69.1 (2001) 79.

[72]   I. Dotsenko, "Single atoms on demand for cavity QED experiments", PhD thesis: Universtät Bonn, 2007.

[73]   C. Wieman and T. W. Hänsch, "Doppler-Free Laser Polarization Spectroscopy", Physical Review Letters 36 (1976) 1170.

[74]   U. Schünemann, H. Engler, R. Grimm, M. Weidemüller and M. Zielonkowski, "Simple scheme for tunable frequency offset locking of two lasers", Review of Scientific Instruments 70.1 (1999) 242.

[75]   X. Baillard, A. Gauguet, S. Bize, P. Lemonde, P. Laurent, A. Clairon and P. Rosenbusch, "Interference-filter-stabilized external-cavity diode lasers", Optics Communications 266.2 (2006) 609.

[76]   C. Robens, "Testing the Quantumness of Atom Trajectories", PhD thesis: Universität Bonn, 2017.

[77]   T. W. Hänsch and N. Picqué, "Laser Spectroscopy and Frequency Combs", Journal of Physics: Conference Series 467.1 (2013) 012001.

[78]   *http://www.menlosystems.com/assets/datasheets/MENLO_FC1500-250-ULN_D-EN_2016-07_3w.pdf*, Menlo Systems GmbH, 2018.

[79]   T. Sala, D. Gatti, A. Gambetta, N. Coluccelli, G. Galzerano, P. Laporta and M. Marangoni, "Wide-bandwidth phase lock between a CW laser and a frequency comb based on a feed-forward configuration", Optics Letters 37.13 (2012) 2592.

[80] W. Gunton, M. Semczuk and K. W. Madison, "Method for independent and continuous tuning of N lasers phase-locked to the same frequency comb", Optics Letters 40.18 (2015) 4372.

[81] J. D. Jost, J. L. Hall and J. Ye,
"Continuously tunable, precise, single frequency optical signal generator",
Optics Express 10.12 (2002) 515.

[82] K. Schörner, "Ein phasenstabilisiertes Lasersystem für resonatorinduzierte Raman-Prozesse",
Diplomarbeit: Universität Bonn, 2008.

[83] M. Ammenwerth, "Analysing a phase-frequency lock of a laser to an optical frequency comb",
BSc thesis: Universität Bonn, 2017.

[84] L. Ahlheit,
"Frequenzvariable Phasenstabilisierung eines Diodenlasers auf einen optischen Frequenzkamm",
BSc thesis: Universität Bonn, 2017.

[85] T. Führer, D. Stang and T. Walther,
"Actively controlled tuning of an external cavity diode laser by polarization spectroscopy",
Optics Express 17.7 (2009) 4991.

[86] H. Kogelnik and C. V. Shank, "Coupled-Wave Theory of Distributed Feedback Lasers",
Journal of Applied Physics 43.5 (1972) 2327.

[87] C.-Y. Shih and M. S. Chapman,
"Nondestructive light-shift measurements of single atoms in optical dipole traps",
Physical Review A 87 (2013) 063408.

[88] M. E. Shea and D. J. Gauthier,
"Comment on "Nondestructive light-shift measurements of single atoms in optical dipole traps"",
Physical Review A 96 (2017) 027401.

[89] C. E. Rogers III, J. L. Carini, J. A. Pechkis and P. L. Gould, "Characterization and compensation of the residual chirp in a Mach-Zehnder-type electro-optical intensity modulator",
Optics Express 18.2 (2010) 1166.

[90] N. Courjal, J. M. Dudley and H. Porte,
"Extinction-ratio-independent method for chirp measurements of Mach-Zehnder modulators",
Optics Express 12.3 (2004) 442.

[91] C. Liu, Y. Sun, L. Zhao, S. Zhang, M. M. T. Loy and S. Du,
"Efficiently Loading a Single Photon into a Single-Sided Fabry-Perot Cavity",
Physical Review Letters 113.13 (2014) 133601.

[92] G. P. Djotyan, J. S. Bakos, G. Demeter, P. N. Ignácz, M. Á. Kedves, Z. Sörlei, J. Szigeti and Z. L. Tóth, "Coherent population transfer in Rb atoms by frequency-chirped laser pulses",
Physical Review A 68 (2003) 053409.

[93] E. Keiler, "AOM-Switching Setup to create short, coherent Photon Pulses", tech. rep.,
Universität Bonn, 2017.

[94] A. Derevianko and H. Katori, "Colloquium: Physics of optical lattice clocks",
Reviews of Modern Physics 83 (2011) 331.

[95] F. Schmidt-Kaler, H. Häffner, M. Riebe, S. Gulde, G. P. T. Lancaster, T. Deuschle, C. Becher, C. F. Roos, J. Eschner and R. Blatt,
"Realization of the Cirac-Zoller controlled-NOT quantum gate", Nature 422 (2003) 408.

[96] T. J. Kippenberg and K. J. Vahala, "Cavity Optomechanics: Back-Action at the Mesoscale",
Science 321.5893 (2008) 1172.

[97] A. S. Parkins and H. J. Kimble, "Quantum state transfer between motion and light",
Journal of Optics B: Quantum and Semiclassical Optics 1.4 (1999) 496.

[98] M. Gehm, K. O'Hara, T. Savard and J. Thomas,
"Dynamics of noise-induced heating in atom traps", Physical Review A 58.5 (1998) 3914.

[99] T. Savard, K. O'Hara and J. Thomas,
"Laser-noise-induced heating in far-off resonance optical traps",
Physical Review A 56.2 (1997) R1095.

[100] M. H. Anderson, J. R. Ensher, M. R. Matthews, C. E. Wieman and E. A. Cornell,
"Observation of Bose-Einstein Condensation in a Dilute Atomic Vapor",
Science 269.5221 (1995) 198.

[101] S. Reick, "Internal and external dynamics of a strongly-coupled atom-cavity system",
PhD thesis: Universität Bonn, 2009.

[102] P. Maunz, T. Puppe, I. Schuster, N. Syassen, P. Pinkse and G. Rempe,
"Cavity cooling of a single atom", Nature 428.6978 (2004) 50.

[103] H. Ritsch, P. Domokos, F. Brennecke and T. Esslinger,
"Cold atoms in cavity-generated dynamical optical potentials",
Reviews of Modern Physics 85 (2013) 553.

[104] T. Kampschulte, W. Alt, S. Manz, M. Martinez-Dorantes, R. Reimann, S. Yoon, D. Meschede,
M. Bienert and G. Morigi,
"Electromagnetically-induced-transparency control of single-atom motion in an optical cavity",
Physical Review A 89.3 (2014) 033404.

[105] T. Kampschulte, "Coherently driven three-level atoms in an optical cavity",
PhD thesis: Universität Bonn, 2011.

[106] C. F. Roos, D. Leibfried, A. Mundt, F. Schmidt-Kaler, J. Eschner and R. Blatt, "Experimental
Demonstration of Ground State Laser Cooling with Electromagnetically Induced Transparency",
Physical Review Letters 85 (2000) 5547.

[107] V. Vuleti ć, C. Chin, A. J. Kerman and S. Chu, "Degenerate Raman Sideband Cooling of Trapped
Cesium Atoms at Very High Atomic Densities", Physical Review Letters 81 (1998) 5768.

[108] S. E. Hamann, D. L. Haycock, G. Klose, P. H. Pax, I. H. Deutsch and P. S. Jessen,
"Resolved-Sideband Raman Cooling to the Ground State of an Optical Lattice",
Physical Review Letters 80 (1998) 4149.

[109] A. Kerman, V. Vuletić, C. Chin and S. Chu, "Beyond optical molasses: 3D Raman sideband
cooling of atomic cesium to high phase-space density",
Physical Review Letters 84.3 (2000) 439.

[110] M. Gröbner, P. Weinmann, E. Kirilov and H.-C. Nägerl,
"Degenerate Raman sideband cooling of ^{39}K", Physical Review A 95 (2017) 033412.

[111] W. Happer, "Optical Pumping", Reviews of Modern Physics 44 (1972) 169.

[112] H. J. Lee, C. S. Adams, M. Kasevich and S. Chu,
"Raman Cooling of Atoms in an Optical Dipole Trap", Physical Review Letters 76 (1996) 2658.

[113] D. Leibfried, R. Blatt, C. Monroe and D. Wineland, "Quantum dynamics of single trapped ions",
Reviews of Modern Physics 75.January (2003) 281.

[114] A. Boozer, "Theory of Raman transitions in cavity QED",
Physical Review A 78.3 (2008) 033406.

[115] R. Grimm, M. Weidemüller and Y. B. Ovchinnikov, "Optical Dipole Traps for Neutral Atoms",
Advances in Atomic, Molecular and Optical Physics 42 (2000) 95.

[116] B. Efron and R. J. Tibshirani, *An Introduction to the Bootstrap*, Chapman and Hall, 1993.

[117] C. J. Clopper and E. S. Pearson,
"The Use of Confidence or Fiducial Limits Illustrated in the Case of the Binomial",
Biometrika 26.4 (1934) 404.

[118] R. Kohlrausch, "Theorie des elektrischen Rückstandes in der Leidener Flasche",
Annalen der Physik und Chemie 167.1 (1854) 56.

[119] G. Williams and D. C. Watts, "Non-symmetrical dielectric relaxation behaviour arising from a
simple empirical decay function", Transactions of the Faraday Society 66 (1970) 80.

[120] K. B. Lee, J. Siegel, S. Webb, S. Lévêque-Fort, M. Cole, R. Jones, K. Dowling, M. Lever and
P. French,
"Application of the Stretched Exponential Function to Fluorescence Lifetime Imaging",
Biophysical Journal 81.3 (2001) 1265.

[121] B. S. Mathur, H. Tang and W. Happer, "Light shifts in the alkali atoms",
Physical Review 171.1 (1968) 11.

[122] C. Cohen-Tannoudji and J. Dupont-Roc,
"Experimental Study of Zeeman Light Shifts in Weak Magnetic Fields",
Physical Review A 5.2 (1972) 968.

[123] A. Kaufman, B. Lester and C. Regal,
"Cooling a Single Atom in an Optical Tweezer to its Quantum Ground State",
Physical Review X 2.4 (2012) 041014.

[124] J. D. Thompson, T. G. Tiecke, a. S. Zibrov, V. Vuletić and M. D. Lukin,
"Coherence and Raman Sideband Cooling of a Single Atom in an Optical Tweezer",
Physical Review Letters 110.13 (2013) 133001.

[125] A. D. Boozer, A. Boca, R. Miller, T. E. Northup and H. J. Kimble, "Cooling to the Ground State
of Axial Motion for One Atom Strongly Coupled to an Optical Cavity",
Physical Review Letters 97.8 (2006) 083602.

[126] M. Eckstein, "Three-Level Physics of a Single Atom Coupled to a High Finesse Cavity",
Diplomarbeit: Universität Bonn, 2010.

[127] S. Hild, "Resolved Raman sideband cooling in a doughnut-shaped optical trap",
MSc thesis: Universität Bonn, 2011.

[128] A. Reiserer, C. Nölleke, S. Ritter and G. Rempe,
"Ground-state cooling of a single atom at the center of an optical cavity",
Physical Review Letters 110.22 (2013) 223003.

[129] A. F. Linskens, I. Holleman, N. Dam and J. Reuss, "Two-photon Rabi oscillations",
Physical Review A 54 (1996) 4854.

[130] I. Bloch, J. Dalibard and S. Nascimbene, "Quantum simulations with ultracold quantum gases", Nature Physics 8.4 (2012) 267.

[131] E. Jaynes and F. Cummings, "Comparison of quantum and semiclassical radiation theories with application to the beam maser", Proceedings of the IEEE 51.1 (1963) 89.

[132] H. J. Charmichael,
Statistical Methods in Quantum Optics 1: Master Equations and Fokker-Planck Equations,
Springer, 2002.

[133] D. F. Walls and G. J. Milburn, *Quantum optics*, Springer Science & Business Media, 2007.

[134] M. Aspelmeyer, T. J. Kippenberg and F. Marquardt, "Cavity optomechanics",
Reviews of Modern Physics 86 (2014) 1391.

[135] A. V. Gorshkov, A. André, M. D. Lukin and A. S. Sørensen,
"Photon storage in Λ-type optically dense atomic media. I. Cavity model",
Physical Review A 76.3 (2007) 033804.

[136] J. Dilley, P. Nisbet-Jones, B. W. Shore and A. Kuhn,
"Single-photon absorption in coupled atom-cavity systems",
Physical Review A 85.2 (2012) 023834.

[137] L. Giannelli, T. Schmit, T. Calarco, C. P. Koch, S. Ritter and G. Morigi,
"Optimal storage of a single photon by a single intra-cavity atom",
New Journal of Physics 20.10 (2018) 105009.

[138] N. V. Vitanov, A. A. Rangelov, B. W. Shore and K. Bergmann,
"Stimulated Raman adiabatic passage in physics, chemistry, and beyond",
Reviews of Modern Physics 89 (2017) 015006.

[139] C. Nölleke, A. Neuzner, A. Reiserer, C. Hahn, G. Rempe and S. Ritter,
"Efficient Teleportation Between Remote Single-Atom Quantum Memories",
Physical Review Letters 110.14 (2013) 140403.

[140] M. W. Janowicz and J. M. A. Ashbourn,
"Dynamics of the four-level Λ system in a two-mode cavity",
Physical Review A 55 (1997) 2348.

[141] J. Johansson, P. Nation and F. Nori,
"QuTiP 2: A Python framework for the dynamics of open quantum systems",
Computer Physics Communications 184.4 (2013) 1234.

[142] J. Johansson, P. Nation and F. Nori,
"QuTiP: An open-source Python framework for the dynamics of open quantum systems",
Computer Physics Communications 183.8 (2012) 1760.

[143] D. d'Alessandro, *Introduction to quantum control and dynamics*, Chapman and Hall/CRC, 2007.

[144] T. Caneva, T. Calarco and S. Montangero, "Chopped random-basis quantum optimization",
Physical Review A 84 (2011) 022326.

[145] N. Khaneja, T. Reiss, C. Kehlet, T. Schulte-Herbrüggen and S. J. Glaser, "Optimal control of coupled spin dynamics: design of NMR pulse sequences by gradient ascent algorithms",
Journal of Magnetic Resonance 172.2 (2005) 296.

[146] D. Wales, *Energy landscapes: Applications to clusters, biomolecules and glasses*,
Cambridge University Press, 2003.

[147] F. Gao and L. Han,
       "Implementing the Nelder-Mead simplex algorithm with adaptive parameters",
       Computational Optimization and Applications 51.1 (2012) 259.

[148] M. D. Eisaman, J. Fan, A. Migdall and S. V. Polyakov,
       "Invited Review Article: Single-photon sources and detectors",
       Review of Scientific Instruments 82.7 (2011) 071101.

[149] M. Keller, B. Lange, K. Hayasaka, W. Lange and H. Walther, "Continuous generation of single
       photons with controlled waveform in an ion-trap cavity system", Nature 431 (2004) 1075.

[150] J. McKeever, "Deterministic Generation of Single Photons from One Atom Trapped in a Cavity",
       Science 303.5666 (2004) 1992.

[151] M. Hijlkema, B. Weber, H. P. Specht, S. C. Webster, A. Kuhn and G. Rempe,
       "A single-photon server with just one atom", Nature Physics 3.4 (2007) 253.

[152] D. B. Higginbottom, L. Slodička, G. Araneda, L. Lachman, R. Filip, M. Hennrich and R. Blatt,
       "Pure single photons from a trapped atom source", New Journal of Physics 18.9 (2016) 093038.

[153] R. Albrecht, A. Bommer, C. Pauly, F. Mücklich, A. W. Schell, P. Engel, T. Schröder, O. Benson,
       J. Reichel and C. Becher, "Narrow-band single photon emission at room temperature based on a
       single nitrogen- vacancy center coupled to an all-fiber-cavity",
       Applied Physics Letters 105.073113 (2014).

[154] J. Benedikter, H. Kaupp, T. Hümmer, Y. Liang, A. Bommer, C. Becher, A. Krueger, J. M. Smith,
       T. W. Hänsch and D. Hunger,
       "Cavity-Enhanced Single-Photon Source Based on the Silicon-Vacancy Center in Diamond",
       Physical Review Applied 7.2 (2017) 024031.

[155] A. Jeantet, Y. Chassagneux, C. Raynaud, P. Roussignol, J. S. Lauret, B. Besga, J. Estève,
       J. Reichel and C. Voisin,
       "Widely Tunable Single-Photon Source from a Carbon Nanotube in the Purcell Regime",
       Physical Review Letters 116.24 (2016) 247402.

[156] A. Muller, W. Fang, J. Lawall and G. S. Solomon, "Creating Polarization-Entangled Photon
       Pairs from a Semiconductor Quantum Dot Using the Optical Stark Effect",
       Physical Review Letters 103 (2009) 217402.

[157] J. Miguel-Sánchez, A. Reinhard, E. Togan, T. Volz, A. Imamoglu, B. Besga, J. Reichel and
       J. Estève, "Cavity quantum electrodynamics with charge-controlled quantum dots coupled to a
       fiber Fabry–Perot cavity", New Journal of Physics 15.4 (2013) 045002.

[158] I. Novikova, A. V. Gorshkov, D. F. Phillips, A. S. Sørensen, M. D. Lukin and R. L. Walsworth,
       "Optimal Control of Light Pulse Storage and Retrieval",
       Physical Review Letters 98 (2007) 243602.

[159] I. Marcikic, H. de Riedmatten, W. Tittel, V. Scarani, H. Zbinden and N. Gisin,
       "Time-bin entangled qubits for quantum communication created by femtosecond pulses",
       Physical Review A 66 (2002) 062308.

[160] P. B. Nisbet-Jones, J. Dilley, A. Holleczek, O. Barter and A. Kuhn,
       "Photonic qubits, qutrits and ququads accurately prepared and delivered on demand",
       New Journal of Physics 15.5 (2013) 053007.

[161] R. Hanbury Brown and R. Q. Twiss,
       "Correlation between Photons in two Coherent Beams of Light", Nature 177.4497 (1956) 27.

[162] J. McKeever, A. Boca, A. D. Boozer, R. Miller, J. R. Buck, A. Kuzmich and H. J. Kimble, "Deterministic Generation of Single Photons from One Atom Trapped in a Cavity", Science 303.5666 (2004) 1992.

[163] A. S. Parkins, P. Marte, P. Zoller and H. J. Kimble, "Synthesis of arbitrary quantum states via adiabatic transfer of Zeeman coherence", Physical Review Letters 71 (1993) 3095.

[164] M. Hennrich, T. Legero, A. Kuhn and G. Rempe, "Vacuum-Stimulated Raman Scattering Based on Adiabatic Passage in a High-Finesse Optical Cavity", Physical Review Letters 85 (2000) 4872.

[165] B. W. Shore, "Picturing stimulated Raman adiabatic passage: a STIRAP tutorial", Advances in Optics and Photonics 9.3 (2017) 563.

[166] P. Nisbet-Jones, "Shaping Single Photons", PhD thesis: University of Oxford, 2012.

[167] A. V. Gorshkov, A. André, M. D. Lukin and A. S. Sørensen, "Photon storage in Λ-type optically dense atomic media. II. Free-space model", Physical Review A 76 (2007) 033805.

[168] M. Bader, S. Heugel, a. L. Chekhov, M. Sondermann and G. Leuchs, "Efficient coupling to an optical resonator by exploiting time-reversal symmetry", New Journal of Physics 15 (2013).

[169] T. Wilk, "Quantum Interface between an Atom and a Photon", PhD thesis: TU München, 2008.

[170] M. Tanida, R. Okamoto and S. Takeuchi, "Highly indistinguishable heralded single-photon sources using parametric down conversion", Optics Express 20.14 (2012) 15275.

[171] H. J. Kimble, M. Dagenais and L. Mandel, "Photon Antibunching in Resonance Fluorescence", Physical Review Letters 39.11 (1977) 691.

[172] H. Paul, "Photon antibunching", Reviews of Modern Physics 54.4 (1982) 1061.

[173] J. Bochmann, M. Mücke, C. Guhl, S. Ritter, G. Rempe and D. L. Moehring, "Lossless State Detection of Single Neutral Atoms", Physical Review Letters 104 (2010) 203601.

[174] G. K. Gulati, H. Takahashi, N. Podoliak, P. Horak and M. Keller, "Fiber cavities with integrated mode matching optics", Scientific Reports 7.1 (2017) 5556.

[175] J. Simon, H. Tanji, S. Ghosh and V. Vuletić, "Single-photon bus connecting spin-wave quantum memories", Nature Physics 3.11 (2007) 765.

[176] L. Li and A. Kuzmich, "Quantum memory with strong and controllable Rydberg-level interactions", Nature Communications 7 (2016) 13618.

[177] R. Zhao, Y. O. Dudin, S. D. Jenkins, C. J. Campbell, D. N. Matsukevich, T. a. B. Kennedy and A. Kuzmich, "Long-lived quantum memory", Nature Physics 5.2 (2008) 100.

[178] B. Zhao, Y.-A. Chen, X.-H. Bao, T. Strassel, C.-S. Chuu, X.-M. Jin, J. Schmiedmayer, Z.-S. Yuan, S. Chen and J.-W. Pan, "A millisecond quantum memory for scalable quantum networks", Nature Physics 5.2 (2008) 95.

[179] E. Bimbard, R. Boddeda, N. Vitrant, A. Grankin, V. Parigi, J. Stanojevic, A. Ourjoumtsev and P. Grangier, "Homodyne Tomography of a Single Photon Retrieved on Demand from a Cavity-Enhanced Cold Atom Memory", Physical Review Letters 112 (2014) 033601.

[180] J. Wolters, G. Buser, A. Horsley, L. Béguin, A. Jöckel, J. P. Jahn, R. J. Warburton and
P. Treutlein,
"Simple Atomic Quantum Memory Suitable for Semiconductor Quantum Dot Single Photons",
Physical Review Letters 119.6 (2017) 1.

[181] C. Kurz, M. Schug, P. Eich, J. Huwer, P. Müller and J. Eschner,
"Experimental protocol for high-fidelity heralded photon-to-atom quantum state transfer",
Nature Communications 5 (2014) 5527.

[182] N. Piro, F. Rohde, C. Schuck, M. Almendros, J. Huwer, J. Ghosh, A. Haase, M. Hennrich,
F. Dubin and J. Eschner, "Heralded single-photon absorption by a single atom",
Nature Physics 7 (2011) 17.

[183] M. T. Rakher, R. J. Warburton and P. Treutlein, "Prospects for storage and retrieval of a
quantum-dot single photon in an ultracold 87Rb ensemble", Physical Review A 88.5 (2013) 1.

[184] H. M. Meyer, R. Stockill, M. Steiner, C. Le Gall, C. Matthiesen, E. Clarke, A. Ludwig,
J. Reichel, M. Atatüre and M. Köhl,
"Direct Photonic Coupling of a Semiconductor Quantum Dot and a Trapped Ion",
Physical Review Letters 114.12 (2015) 123001.

[185] C. Matthiesen, A. N. Vamivakas and M. Atatüre,
"Subnatural Linewidth Single Photons from a Quantum Dot",
Physical Review Letters 108.9 (2012) 093602.

[186] A. V. Gorshkov, A. André, M. Fleischhauer, A. S. Sørensen and M. D. Lukin,
"Universal approach to optimal photon storage in atomic media",
Physical Review Letters 98.12 (2007) 1.

[187] J. Dilley, "A Single-Photon Source for Quantum Networking",
PhD thesis: Exeter College, Oxford, 2012.

[188] M. Fleischhauer, S. Yelin and M. Lukin,
"How to trap photons? Storing single-photon quantum states in collective atomic excitations",
Optics Communications 179.1-6 (2000) 395.

[189] G. S. Vasilev, D. Ljunggren and A. Kuhn, "Single photons made-to-measure",
New Journal of Physics 12.6 (2010) 063024.

[190] A. D. Boozer, A. Boca, R. Miller, T. E. Northup and H. J. Kimble,
"Reversible State Transfer between Light and a Single Trapped Atom",
Physical Review Letters 98.19 (2007) 193601.

[191] B. W. Shore,
"Pre-History Of The Concepts Underlying Stimulated Raman Adiabatic Passage (STIRAP)",
Acta Physica Slovaca 63.6 (2013) 361.

[192] M. Radonjić and B. M. Jelenković,
"Stark-chirped rapid adiabatic passage among degenerate-level manifolds",
Physical Review A 80 (2009) 043416.

[193] N. Mukherjee and R. N. Zare,
"Stark-induced adiabatic Raman passage for preparing polarized molecules",
The Journal of Chemical Physics 135.2 (2011) 024201.

[194] A. V. Smith, "Numerical studies of adiabatic population inversion in multilevel systems",
Journal of Optical Society of America B 9.9 (1992) 1543.

[195] I. I. Boradjiev and N. V. Vitanov,
"Stimulated Raman adiabatic passage with unequal couplings: Beyond two-photon resonance",
Physical Review A 81 (2010) 053415.

[196] H. P. Specht, "Einzelatom-Quantenspeicher für Polarisations-Qubits",
PhD thesis: Technische Universität München, 2010.

[197] N. V. Vitanov, K.-A. Suominen and B. W. Shore,
"Creation of coherent atomic superpositions by fractional stimulated Raman adiabatic passage",
Journal of Physics B: Atomic, Molecular and Optical Physics 32.18 (1999) 4535.

[198] K. M. Birnbaum, A. Boca, R. Miller, A. D. Boozer, T. E. Northup and H. J. Kimble,
"Photon blockade in an optical cavity with one trapped atom", Nature 436 (2005) 87.

[199] B. Dayan, A. S. Parkins, T. Aoki, E. P. Ostby, K. J. Vahala and H. J. Kimble,
"A Photon Turnstile Dynamically Regulated by One Atom", Science 319.5866 (2008) 1062.

[200] M. P. Fewell, B. W. Shore and K. Bergmann,
"Coherent Population Transfer Among Three States: Full Algebraic Solutions and the Relevance of Non Adiabatic Processes to Transfer by Delayed Pulses",
Australian Journal of Physics 50.2 (1997) 281.

[201] J. Werschnik and E. K. U. Gross, "Quantum optimal control theory",
Journal of Physics B: Atomic, Molecular and Optical Physics 40.18 (2007) R175.

[202] M. D. Lukin, "Colloquium: Trapping and manipulating photon states in atomic ensembles",
Reviews of Modern Physics 75 (2003) 457.

[203] I. R. Solá, V. S. Malinovsky and D. J. Tannor,
"Optimal pulse sequences for population transfer in multilevel systems",
Physical Review A 60 (1999) 3081.

[204] J. L. O'Brien, "Optical Quantum Computing", Science 318.5856 (2007) 1567.

[205] N. Gisin and R. Thew, "Quantum communication", Nature Photonics 1.3 (2007) 165.

[206] H. de Riedmatten, I. Marcikic, J. A. W. van Houwelingen, W. Tittel, H. Zbinden and N. Gisin,
"Long-distance entanglement swapping with photons from separated sources",
Physical Review A 71.5 (2005).

[207] J. W. Pan, Z. B. Chen, C. Y. Lu, H. Weinfurter, A. Zeilinger and M. Zukowski,
"Multiphoton entanglement and interferometry", Reviews of Modern Physics 84.2 (2012) 777.

[208] P. Michler, A. Kiraz, C. Becher, W. V. Schoenfeld, P. M. Petroff, L. Zhang, E. Hu and
A. Imamoglu, "A Quantum Dot Single-Photon Turnstile Device",
Science 290.5500 (2000) 2282.

[209] C. Santori, M. Pelton, G. Solomon, Y. Dale and Y. Yamamoto,
"Triggered Single Photons from a Quantum Dot", Physical Review Letters 86 (2001) 1502.

[210] Y.-M. He, Y. He, Y.-J. Wei, D. Wu, M. Atatüre, C. Schneider, S. Höfling, M. Kamp, C.-Y. Lu and
J.-W. Pan,
"On-demand semiconductor single-photon source with near-unity indistinguishability",
Nature Nanotechnology 8 (2013) 213.

[211] O. Benson, C. Santori, M. Pelton and Y. Yamamoto,
"Regulated and Entangled Photons from a Single Quantum Dot",
Physical Review Letters 84 (2000) 2513.

[212] R. M. Stevenson, R. J. Young, P. Atkinson, K. Cooper, D. A. Ritchie and A. J. Shields, "A semiconductor source of triggered entangled photon pairs", Nature 439.7073 (2006) 179.

[213] N. Akopian, N. Lindner, E. Poem, Y. Berlatzky, J. Avron, D. Gershoni, B. Gerardot and P. Petroff, "Entangled photon pairs from semiconductor quantum dots", Physical Review Letters 96.13 (2006) 130501.

[214] R. Hafenbrak, S. Ulrich, P. Michler, L. Wang, A. Rastelli and O. Schmidt, "Triggered polarization-entangled photon pairs from a single quantum dot up to 30 K", New Journal of Physics 9.9 (2007) 315.

[215] A. Dousse, J. Suffczyński, A. Beveratos, O. Krebs, A. Lemaître, I. Sagnes, J. Bloch, P. Voisin and P. Senellart, "Ultrabright source of entangled photon pairs", Nature 466.7303 (2010) 217.

[216] R. Keil, M. Zopf, Y. Chen, B. Höfer, J. Zhang, F. Ding and O. G. Schmidt, "Solid-state ensemble of highly entangled photon sources at rubidium atomic transitions", Nature Communications 8 (2017) 15501.

[217] P. Atkinson, E. Zallo and O. G. Schmidt, "Independent wavelength and density control of uniform GaAs/AlGaAs quantum dots grown by infilling self-assembled nanoholes", Journal of Applied Physics 112.5 (2012) 054303.

[218] S. Kumar, R. Trotta, E. Zallo, J. D. Plumhof, P. Atkinson, A. Rastelli and O. G. Schmidt, "Strain-induced tuning of the emission wavelength of high quality GaAs/AlGaAs quantum dots in the spectral range of the 87Rb D2 lines", Applied Physics Letters 99.16 (2011) 161118.

[219] V. Giesz, S. L. Portalupi, T. Grange, C. Antón, L. De Santis, J. Demory, N. Somaschi, I. Sagnes, A. Lemaître, L. Lanco, A. Auffèves and P. Senellart, "Cavity-enhanced two-photon interference using remote quantum dot sources", Physical Review B 92.16 (2015) 161302.

[220] X. Ding, Y. He, Z.-C. Duan, N. Gregersen, M.-C. Chen, S. Unsleber, S. Maier, C. Schneider, M. Kamp, S. Höfling, C.-Y. Lu and J.-W. Pan, "On-Demand Single Photons with High Extraction Efficiency and Near-Unity Indistinguishability from a Resonantly Driven Quantum Dot in a Micropillar", Physical Review Letters 116 (2016) 020401.

[221] A. J. Bennett, M. A. Pooley, R. M. Stevenson, M. B. Ward, R. B. Patel, A. B. de la Giroday, N. Sköld, I. Farrer, C. A. Nicoll, D. A. Ritchie and A. J. Shields, "Electric-field-induced coherent coupling of the exciton states in a single quantum dot", Nature Physics 6.12 (2010) 947.

[222] M. Ghali, K. Ohtani, Y. Ohno and H. Ohno, "Generation and control of polarization-entangled photons from GaAs island quantum dots by an electric field", Nature Communications 3 (2012) 661.

[223] J. Zhang, E. Zallo, B. Höfer, Y. Chen, R. Keil, M. Zopf, S. Böttner, F. Ding and O. G. Schmidt, "Electric-Field-Induced Energy Tuning of On-Demand Entangled-Photon Emission from Self-Assembled Quantum Dots", Nano Letters 17.1 (2017) 501.

[224] M. A. Pooley, A. J. Bennett, R. M. Stevenson, A. J. Shields, I. Farrer and D. A. Ritchie, "Energy-Tunable Quantum Dot with Minimal Fine Structure Created by Using Simultaneous Electric and Magnetic Fields", Physical Review Applied 1.2 (2014) 024002.

[225] F. Ding, R. Singh, J. D. Plumhof, T. Zander, V. Křápek, Y. H. Chen, M. Benyoucef, V. Zwiller, K. Dörr, G. Bester, A. Rastelli and O. G. Schmidt, "Tuning the Exciton Binding Energies in Single Self-Assembled InGaAs/GaAs Quantum Dots by Piezoelectric-Induced Biaxial Stress", Physical Review Letters 104.6 (2010) 067405.

[226] J. Zhang, Y. Huo, A. Rastelli, M. Zopf, B. Höfer, Y. Chen, F. Ding and O. G. Schmidt, "Single Photons On-Demand from Light-Hole Excitons in Strain-Engineered Quantum Dots", Nano Letters 15.1 (2015) 422.

[227] Y. Chen, J. Zhang, M. Zopf, K. Jung, Y. Zhang, R. Keil, F. Ding and O. G. Schmidt, "Wavelength-tunable entangled photons from silicon-integrated III-V quantum dots", Nature Communications 7 (2016) 10387.

[228] M. Metcalfe, A. Muller, G. S. Solomon and J. Lawall, "Active feedback of a Fabry-Perot cavity to the emission of a single InAs/GaAs quantum dot", Journal of the Optical Society of America B 26.12 (2009) 2308.

[229] R. Trotta, P. Atkinson, J. D. Plumhof, E. Zallo, R. O. Rezaev, S. Kumar, S. Baunack, J. R. Schröter, A. Rastelli and O. G. Schmidt, "Nanomembrane Quantum-Light-Emitting Diodes Integrated onto Piezoelectric Actuators", Advanced Materials 24.20 (2012) 2668.

[230] C. K. Hong, Z. Y. Ou and L. Mandel, "Measurement of subpicosecond time intervals between two photons by interference", Physical Review Letters 59 (1987) 2044.

[231] R. B. Patel, A. J. Bennett, I. Farrer, C. A. Nicoll, D. A. Ritchie and A. J. Shields, "Two-photon interference of the emission from electrically tunable remote quantum dots", Nature Photonics 4 (2010) 632.

[232] E. B. Flagg, A. Muller, S. V. Polyakov, A. Ling, A. Migdall and G. S. Solomon, "Interference of Single Photons from Two Separate Semiconductor Quantum Dots", Physical Review Letters 104.13 (2010) 137401.

[233] C. K. Hong and L. Mandel, "Experimental realization of a localized one-photon state", Physical Review Letters 56 (1986) 58.

[234] C. L. Salter, R. M. Stevenson, I. Farrer, C. A. Nicoll, D. A. Ritchie and A. J. Shields, "An entangled-light-emitting diode", Nature 465 (2010) 594.

[235] Y. Zhang, Y. Chen, M. Mietschke, L. Zhang, F. Yuan, S. Abel, R. Hühne, K. Nielsch, J. Fompeyrine, F. Ding and O. G. Schmidt, "Monolithically Integrated Microelectromechanical Systems for On-Chip Strain Engineering of Quantum Dots", Nano Letters 16.9 (2016) 5785.

[236] M. Müller, S. Bounouar, K. D. Jöns, M. Glässl and P. Michler, "On-demand generation of indistinguishable polarization-entangled photon pairs", Nature Photonics 8 (2014) 224.

[237] J. D. Plumhof, R. Trotta, A. Rastelli and O. G. Schmidt, "Experimental methods of post-growth tuning of the excitonic fine structure splitting in semiconductor quantum dots", Nanoscale Research Letters 7.1 (2012) 336.

[238] M. Zopf, "Coherent Strain Tunable Single Photon Sources", MSc thesis: Technische Universität Dresden, 2014.

[239] M. Fox, *Quantum Optics: An Introduction*, Oxford University Press, 2006.

[240] S. L. Portalupi, M. Widmann, C. Nawrath, M. Jetter, P. Michler, J. Wrachtrup and I. Gerhardt, "Simultaneous Faraday filtering of the Mollow triplet sidebands with the Cs-D1 clock transition", Nature Communications 7 (2016) 13632.

[241] J. A. Zielińska, F. A. Beduini, N. Godbout and M. W. Mitchell, "Ultranarrow Faraday rotation filter at the Rb D1 line", Optics Letters 37.4 (2012) 524.

[242] M. A. Zentile, J. Keaveney, L. Weller, D. J. Whiting, C. S. Adams and I. G. Hughes, "ElecSus: A program to calculate the electric susceptibility of an atomic ensemble", Computer Physics Communications 189 (2015) 162.

[243] J. Brossel, J.-L. Mosser and M. Winter, "Absorption du sodium par des parois de verre chauffées à 120° C", Journal de Physique et Le Radium 16.10 (1955) 814.

[244] J. Ma, A. Kishinevski, Y.-Y. Jau, C. Reuter and W. Happer, "Modification of glass cell walls by rubidium vapor", Physical Review A 79.4 (2009) 042905.

[245] P. Siddons, C. S. Adams, C. Ge and I. G. Hughes, "Absolute absorption on rubidium D lines: comparison between theory and experiment", Journal of Physics B: Atomic, Molecular and Optical Physics 41.15 (2008) 155004.

[246] L. Weller, R. J. Bettles, P. Siddons, C. S. Adams and I. G. Hughes, "Absolute absorption on the rubidium D1 line including resonant dipole-dipole interactions", Journal of Physics B: Atomic, Molecular and Optical Physics 44.19 (2011) 195006.

[247] L. Weller, T. Dalton, P. Siddons, C. S. Adams and I. G. Hughes, "Measuring the Stokes parameters for light transmitted by a high-density rubidium vapour in large magnetic fields", Journal of Physics B: Atomic, Molecular and Optical Physics 45.5 (2012) 055001.

[248] A. V. Kuhlmann, J. Houel, A. Ludwig, L. Greuter, D. Reuter, A. D. Wieck, M. Poggio and R. J. Warburton, "Charge noise and spin noise in a semiconductor quantum device", Nature Physics 9 (2013) 570.

[249] E. Uruñuela, "Digital Lock-Box for frequency stabilization of single photon sources", tech. rep., Universität Bonn, 2016.

[250] H. Jung and D.-G. Gweon, "Creep characteristics of piezoelectric actuators", Review of Scientific Instruments 71.4 (2000) 1896.

[251] V. Leong, S. Kosen, B. Srivathsan, G. K. Gulati, A. Cerè and C. Kurtsiefer, "Hong-Ou-Mandel interference between triggered and heralded single photons from separate atomic systems", Physical Review A 91 (2015) 063829.

[252] R. Kaltenbaek, B. Blauensteiner, M. Żukowski, M. Aspelmeyer and A. Zeilinger, "Experimental Interference of Independent Photons", Physical Review Letters 96 (2006) 240502.

[253] J. Bylander, I. Robert-Philip and I. Abram, "Interference and correlation of two independent photons", The European Physical Journal D 22.2 (2003) 295.

[254] M. Zopf, PhD thesis: IFW Dresden, 2019.

[255] A. Thoma, P. Schnauber, J. Böhm, M. Gschrey, J.-H. Schulze, A. Strittmatter, S. Rodt, T. Heindel and S. Reitzenstein, "Two-photon interference from remote deterministic quantum dot microlenses", Applied Physics Letters 110.1 (2017) 011104.

[256] I. Aharonovich, D. Englund and M. Toth, "Solid-state single-photon emitters",
Nature Photonics 10 (2016) 631.

[257] K. D. Jöns, K. Stensson, M. Reindl, M. Swillo, Y. Huo, V. Zwiller, A. Rastelli, R. Trotta and
G. Björk, "Two-photon interference from two blinking quantum emitters",
Physical Review B 96 (2017) 075430.

[258] A. Ulhaq, S. Weiler, S. M. Ulrich, R. Roßbach, M. Jetter and P. Michler,
"Cascaded single-photon emission from the Mollow triplet sidebands of a quantum dot",
Nature Photonics 6 (2012) 238.

[259] A. Gushterov, L. Lingys and J. Reithmaier, "Control of dot geometry and photoluminescence
linewidth of InGaAs/GaAs quantum dots by growth conditions",
Journal of Crystal Growth 311.7 (2009) 1783.

[260] A. V. Kuhlmann, J. H. Prechtel, J. Houel, A. Ludwig, D. Reuter, A. D. Wieck and
R. J. Warburton, "Transform-limited single photons from a single quantum dot",
Nature Communications 6 (2015) 8204.

[261] Y. Chen, M. Zopf, R. Keil, F. Ding and O. G. Schmidt, "Highly-efficient extraction of entangled
photons from quantum dots using a broadband optical antenna",
Nature Communications 9.1 (2018) 2994.

[262] C. Deng and X. Hu, "Decoherence of nuclear spin quantum memory in a quantum dot",
IEEE Transactions on Nanotechnology 4.1 (2005) 35.

[263] R. J. Young, S. J. Dewhurst, R. M. Stevenson, P. Atkinson, A. J. Bennett, M. B. Ward, K. Cooper,
D. A. Ritchie and A. J. Shields,
"Single electron-spin memory with a semiconductor quantum dot",
New Journal of Physics 9.10 (2007) 365.

[264] A. Holleczek, O. Barter, A. Rubenok, J. Dilley, P. B. R. Nisbet-Jones, G. Langfahl-Klabes,
G. D. Marshall, C. Sparrow, J. L. O'Brien, K. Poulios, A. Kuhn and J. C. F. Matthews,
"Quantum Logic with Cavity Photons From Single Atoms",
Physical Review Letters 117 (2016) 023602.

[265] N. Akopian, L. Wang, A. Rastelli, O. G. Schmidt and V. Zwiller,
"Hybrid semiconductor-atomic interface : slowing down single photons from a quantum dot",
Nature Photonics 5 (2011) 2.

[266] F. Reiter, M. J. Kastoryano and A. S. Sørensen,
"Driving two atoms in an optical cavity into an entangled steady state using engineered decay",
New Journal of Physics 14.5 (2012) 053022.

[267] M. P. Baden, K. J. Arnold, A. L. Grimsmo, S. Parkins and M. D. Barrett,
"Realization of the Dicke Model Using Cavity-Assisted Raman Transitions",
Physical Review Letters 113 (2014) 020408.

[268] F. Haas, J. Volz, R. Gehr, J. Reichel and J. Esteve,
"Entangled States of More Than 40 Atoms in an Optical Fiber Cavity",
Science 344.6180 (2014) 180.

[269] M. T. DePue, C. McCormick, S. L. Winoto, S. Oliver and D. S. Weiss,
"Unity Occupation of Sites in a 3D Optical Lattice", Physical Review Letters 82.11 (1999) 2262.

[270] R. Schmied, "Quantum state tomography of a single qubit: comparison of methods",
Journal of Modern Optics 63.18 (2016) 1744.

[271] D. Köhler, "Quantenzustandstomographie mit polarisierten QuBits",
BSc thesis: Universität Bonn, 2016.

[272] R. M. Stevenson, R. J. Young, P. See, D. G. Gevaux, K. Cooper, P. Atkinson, I. Farrer,
D. A. Ritchie and A. J. Shields,
"Magnetic-field-induced reduction of the exciton polarization splitting in InAs quantum dots",
Physical Review B 73 (2006) 033306.

[273] M. Bock, P. Eich, S. Kucera, M. Kreis, A. Lenhard, C. Becher and J. Eschner, "High-fidelity
entanglement between a trapped ion and a telecom photon via quantum frequency conversion",
Nature Communications 9.1 (2018) 1998.

[274] J. H. Weber, B. Kambs, J. Kettler, S. Kern, J. Maisch, H. Vural, M. Jetter, S. L. Portalupi,
C. Becher and P. Michler, "Two-photon interference in the telecom C-band after frequency
conversion of photons from remote quantum emitters", Nature Nanotechnology (2018).

[275] N. Lütkenhaus, J. Calsamiglia and K.-A. Suominen, "Bell measurements for teleportation",
Physical Review A 59 (1999) 3295.

Acknowledgements

With this work, an interesting time is coming to an end, during which I had the opportunity to work and spend time with many skilled – and more importantly – motivated people. By strictly using the pronoun 'we' throughout the main text, I have already implied that complicated quantum experiments and long-distance collaborations cannot be conducted without the help and contributions of many people. As a last challenge, I will try to express my gratitude to all of them in only a few paragraphs.

First of all, I would like to thank Prof. Dr. Dieter Meschede who has given me the opportunity to work on his exciting experiments, while being a kind and understanding mentor at any point in time. Every new member eventually realizes that the group he gathered is a fantastic environment for discussions and inter-cultural exchange. Furthermore I thank Prof. Dr. Simon Stellmer for being my second advisor and, moreover, taking a sincere interest in our work.

I appreciate the help and motivation from Dr. Lothar Ratschbacher, who has been a role-model postdoc in the early stage of the presented experiments by providing ideas, guiding many students and teaching how to solve problems in a sometimes more, sometimes less dirty way. While probably all of us were happy to hear his 'let's call it a day' at 4 a.m. (on actually the next day), working with him never felt forced, which I enjoyed a lot. Let's meet and bake DDS boards soon!

Dr. Wolfgang Alt always found the time to discuss and picture problems in a comprehensive yet understandable way. His incredible overview over our field, his capability of live circuit design and critical questioning have often led to solutions, for which I am very grateful. Not to mention his supply of sweets and high-quality fruits, which he generously shared with the entire group.

A big thanks goes to Dr. René Reimann who patiently taught me the lab basics and the importance of the chosen AOM diffraction order – I hope you are happy your cooling scheme became a tool. And don't worry, I'm not feeling cold.

Dr. Jose Gallego, my predecessor, deserves special thanks for investing so much time, a tooth and his youth in building the fiber-based atom-cavity experiment. He is not only an exemplary experimentalist, but also my long-lost twin brother who can finish each of my...

I would like to thank the lab team: Eduardo Uruñuela and Elvira Keiler, for their support and strong teamwork on everyday basis – together, we made a significant progress. Our early-stage members Maximilian Ammenwerth and Lukas Ahlheit have been astonishingly motivated and skillful given their involvement in ongoing studies. I'm confident that the experiment is in good hands now. A special thanks goes to Eduardo for running the lab during the final photon storage experiments and to Dr. Hannes Pfeifer for significant improvements of our post-selection routines and data evaluation.

I enjoyed the opportunity to work for and in the lab of Prof. Dr. Oliver G. Schmidt. Thanks to the collaboration, especially with Michael Zopf and Robert Keil, I had the chance to work with both single atoms and single photons.

In early times, the lab-corridor office became a second home thanks to Dr. Carsten Robens, Dr. Stefan Brakhane, Jose from Japan, Gautam Ramola, Jonathan Zopes, Ricardo Gómez Escalante, Max Werninghaus and Dr. Geol Moon. I will never forget the atmosphere created by flying drones, nerf-gun wars, ceiling volleyball and squeaking 3D printers. My apologies go to Dr. Seokchan Yoon for

Declaration of Authorship

I hereby certify that the work presented here was accomplished by myself and without the use of illegitimate means of support, and that no sources and tools were used other than those cited.

_____   _____
Place, date   Tobias Nicolay Macha